
Article:
Barker, R orcid.org/0000-0002-5106-6929, Burkle, D, Charpentier, T orcid.org/0000-0002-3433-3511 et al. (2 more authors) (2018) A review of iron carbonate ($FeCO_3$) formation in the oil and gas industry. Corrosion Science, 142. pp. 312-341. ISSN 0010-938X

https://doi.org/10.1016/j.corsci.2018.07.021

A review of iron carbonate ($FeCO_3$) formation in the oil and gas industry

Richard Barker*, Daniel Burkle, Thibaut Charpentier, Harvey Thompson and Anne Neville

Institute of Functional Surfaces, School of Mechanical Engineering, University of Leeds, Leeds, LS2 9JT, United Kingdom

**Corresponding Author*

Abstract

This paper reviews the information in the literature relating to $FeCO_3$ formation in the context of oil and gas production. Numerous factors which influence the kinetics, physical properties and protective nature of $FeCO_3$ are considered in addition to a review of semi-empirical models developed to predict precipitation/corrosion layer accumulation rate.

The limitations of current models are discussed and the challenges of conducting deposition studies onto steel surfaces in a controlled environment using laboratory based techniques are also reviewed. Finally, more recently employed experimental techniques are considered in their potential to provide a further understanding of $FeCO_3$ and mixed carbonate kinetics.

Key words: Carbon Steel (A), SEM (B), Interfaces (C), Kinetic Parameters (C).

Table of Contents

1. Introduction

Companies within the oil and gas industry have a responsibility to ensure that hydrocarbons are produced in a safe and reliable manner. However, internal pipeline corrosion as a result of dissolved carbon dioxide (CO_2) in process fluids represents one of the main obstacles towards successful production.

The formation of iron carbonate ($FeCO_3$) internally within carbon steel pipework plays a crucial role in defining the rate of corrosion of the underlying steel. The layer formed is capable of reducing the corrosion kinetics by well over an order of magnitude by acting as a diffusion barrier to electrochemically active species and/or blocking active sites on the steel surface.[1]

Owing to its properties, the $FeCO_3$ film has the ability to assist in internal pipeline corrosion mitigation. However, some authors believe that the formation and subsequent local breakdown of the film by mechanical or chemical effects, or the non-uniform coverage of the layer is a pre-cursor to localised corrosion[2-6]. Consequently, it is critical to understand the fundamental processes governing the formation of $FeCO_3$ so that the operating and environmental conditions can be related to not only the formation rate, but also its physical properties and degree of protection.

Although there have been a number of review papers published within the area of CO_2 corrosion over the last two decades[6-15], these have either focused on the inherent complexities of modelling the electrochemical processes, the corrosion mechanism itself, or the numerous factors influencing the corrosion response of carbon steel in the absence of protective films. When referred to within review papers, the discussion of film formation typically comprises a very brief supplementary component which covers the topic superficially. However, the continued importance of the role of $FeCO_3$ film formation is evidenced by the initiation of a number of recent joint industry-academic meetings and current research collaborations[16, 17].

Despite the existence of a significant body of literature discussing the electrochemical processes and reaction pathways relating to the CO_2 corrosion mechanism and the development of corrosion prediction models (as summarised recently by Kahyarian et al.[11, 12]), considerably less attention is afforded towards the development of models to predict $FeCO_3$ nucleation and growth. This is reflected in the observed complexity of the

CO_2 corrosion mechanistic models versus the proposed, much less evolved, semi-empirical precipitation expressions. As will be discussed later, while the developed CO_2 corrosion models in the absence of protective films are fairly robust and agree reasonably well with one another, this level of accuracy is not shared by the precipitation models, resulting in corrosion prediction models accounting for $FeCO_3$ precipitation diverging significantly from one another[18]. Models which predict corrosion from first principles have so far struggled to correctly incorporate the effect of film formation of protective corrosion products because the necessary rate parameters for the nucleation and growth behaviour are not reliably known, nor are the fundamentals associated with such processes[18].

The breakdown in model predictive capabilities in protective film forming conditions presents a research gap which, if filled, will facilitate more accurate prediction of corrosion rates, and bring the research community one step closer towards understanding the mechanism of localised corrosion, improving the safety and reliability of pipeline transport. This can only be achieved through a fundamental understanding of corrosion product nucleation and growth processes and their sensitivity to numerous environmental, operational and steel/interfacial properties. To achieve such an understanding, it is important to raise awareness of experimental limitations of laboratory based studies and which experimental approaches, methodologies and *in situ* measurements are available to accurately determine and understand the precipitation kinetics and morphology of $FeCO_3$ in greater detail.

This review paper is focused exclusively on consolidating the information relating to $FeCO_3$ accumulation on carbon steel pipelines in the context of oil and gas production. The paper discusses the concept of saturation ratio (or supersaturation) and how this relates to the nucleation, growth and morphology of $FeCO_3$ films. Consideration is also afforded to the numerous factors influencing the deposition behaviour and kinetics of $FeCO_3$ (both directly and indirectly), reviewing in detail the semi-empirical models developed to predict precipitation rates and/or corrosion layer accumulation rates (CLARs), making the distinction between the two terms.

Based on the models reviewed, a selection of key influential parameters are discussed which are not incorporated into current prediction tools, yet have the potential to influence kinetics dramatically. The limitations of experimental techniques for accurately

determining $FeCO_3$ precipitation are highlighted before discussing alternative approaches which hold promise for improving the understanding of the nucleation and growth of this corrosion product. These methodologies are drawn from both the corrosion and mineral scaling literature and help to address some of the limitations identified with more conventional experimental techniques.

2. Background - CO_2 corrosion mechanism

Before discussing the process of $FeCO_3$ formation, it is perhaps prudent to review the current understanding of the CO_2 corrosion mechanisms associated with carbon steel. This section is intended to provide a brief overview of the equilibria and electrochemical reactions associated with CO_2 corrosion, not to provide a holistic review of the corrosion process, as this has been covered extensively in other publications. For further detail relating to the electrochemical reactions, transport processes and mechanistic modelling, the reader is directed to the review Chapter and article on CO_2 corrosion by Kahyarian et al.[11, 12].

Dugstad[15] discussed that CO_2 corrosion and the role of CO_2 gas dissolved within a solution is not related to one particular mechanism. CO_2 corrosion is in fact, a complex process which requires a number of electrochemical, chemical and mass transport reactions to occur in conjunction with one another at the steel surface. Chemical equilibria, anodic and cathodic reactions can be used to describe the CO_2 corrosion process and these are outlined in the following sections.

2.1 Water chemistry and chemical equilibria reactions

After dissolution in water, CO_2 becomes hydrated to produce carbonic acid (H_2CO_3).[19] H_2CO_3 is diprotic, allowing it to partially dissociate in two steps, resulting in the formation of bicarbonate (HCO_3^-), carbonate (CO_3^{2-}) and hydrogen (H^+) ions[19, 20]. These chemical equilibria reactions have been extensively studied[21-24] and are summarised in Table 1, along with their corresponding equilibrium constant expressions. Carbonic acid dissociation (Reaction 1c) is known to be a particularly rapid reaction compared to CO_2 dissolution and hydration (Reactions 1a and 1b)[25].

The reactions in Table 1 represent a system involving solely CO_2 and pure water. However, the water chemistry encountered in oil and gas production is invariably more complex than this, containing various dissolved salts and other weak acids.

Table 1: Chemical equilibria reactions for CO_2 dissolution in pure water

Chemical Equilibria Reaction	*Equilibrium constant expression*	
$CO_{2(g)} \leftrightarrow CO_{2(aq)}$	$K_{CO_2} = \frac{[CO_{2(aq)}]}{[pCO_{2(g)}]}$	*(1a)*
$CO_{2(aq)} + H_2O_{(l)} \leftrightarrow H_2CO_{3(aq)}$	$K_{hyd} = \frac{[H_2CO_3]}{[CO_{2(aq)}]}$	*(1b)*
$H_2CO_{3(aq)} \leftrightarrow H^+_{(aq)} + HCO^-_{3(aq)}$	$K_{ca} = \frac{[H^+][HCO_3^-]}{[H_2CO_3]}$	*(1c)*
$HCO^-_{3(aq)} \leftrightarrow H^+_{(aq)} + CO^{2-}_{3(aq)}$	$K_{bi} = \frac{[H^+][CO_3^{2-}]}{[HCO_3^-]}$	*(1d)*
$H_2O_{(l)} \leftrightarrow H^+_{(aq)} + OH^-_{(aq)}$	$K_w = [H^+][OH^-]$	*(1e)*

2.2 Electrochemical reactions

CO_2 corrosion in an electrochemical process and can be divided into both cathodic and anodic reactions. The following text summarises the current understanding in relation to such reactions. It is important to stress that although much is known in relation to these reactions, a number of challenges still remain and there are still gaps in the knowledge related to the significance and pathways of certain reactions, as will be discussed.

2.2.1 Cathodic reactions

The main cathodic reaction at the steel interface (under oil and gas transportation conditions) is hydrogen evolution (i.e. the reduction of H^+ ions). In CO_2-containing environments, the production of hydrogen at the steel surface is facilitated through a collection of cathodic reactions. For a CO_2 system with pure water, the reactions involved are shown in Table 2 and consists of the reduction of H^+, H_2CO_3, HCO_3^- and H_2O. Although these reactions are all thermodynamically identical, they have very different reaction kinetics.

Table 2: Cathodic electrochemical reactions associated with CO_2 corrosion for CO_2 dissolved in pure water

Cathodic electrochemical reactions	
$2H^+_{(aq)} + 2e^- \rightarrow H_{2(g)}$	*(2a)*
$2H_2CO_{3(aq)} + 2e^- \rightarrow H_{2(g)} + 2HCO^-_{3(aq)}$	*(2b)*
$2HCO^-_{3(aq)} + 2e^- \rightarrow H_{2(g)} + 2CO^-_{3(aq)}$	*(2c)*
$2H_2O_{(l)} + 2e^- \rightarrow H_{2(g)} + 2OH^-_{(aq)}$	*(2d)*

Reaction (2a) is hydrogen ion reduction, which has been studied extensively[26-29]. The general consensus is that the reaction can be described using three steps, which involve electrochemical adsorption of H^+ (Reaction 3a), followed by either electrochemical desorption (Reaction 3b) or chemical desorption (Reaction 3c).

$$H^+_{(aq)} + e^- \rightarrow H_{ads} \qquad (3a)$$

$$H_{ads} + H^+_{(aq)} + e^- \rightarrow H_{2(g)} \qquad (3b)$$

$$H_{ads} + H_{ads} \rightarrow H_{2(g)} \qquad (3c)$$

Reaction (2b) is the direct reduction of H_2CO_3. However, it should be noted that more recent research has suggested that this reaction actually occurs via a 'buffering effect' whereby H_2CO_3 dissociates at the steel-electrolyte interface and the resulting H^+ ions are then reduced via Reaction 2a.[30-32] These observations will be discussed further at the end of this section.

Reduction of HCO_3^- (Reaction 2c) is also another possible reaction pathway. However, experience suggests that such a reaction is slower than the 'buffering effect' provided by H_2CO_3 in the pH range 4 to 6. Consequently, in the context of oil and gas production, it can be ignored. However, at near-neutral and alkaline pH, this reaction may become appreciable and warrant consideration because of the high bicarbonate concentration[33]. Again, no studies have confirmed the significance of direct HCO_3^- reduction and whether it is capable of undergoing a similar reaction sequence to that of H_2CO_3 (i.e. dissociation, followed by H^+ reduction).

A final reaction which can be considered is the direct reduction of water (Reaction 2d). Although the reduction of water is thermodynamically equivalent to hydrogen evolution, the alternative reaction pathway exhibits much slower kinetics, resulting in minimal contribution towards the total cathodic reaction under typical oil and gas environments.

It is important to stress that the aforementioned cathodic reactions are the commonly and currently accepted electrochemical reactions relating to CO_2 corrosion of carbon steel. The exact cathodic reaction in the presence of H_2CO_3 arguably still remains open to debate, and is predominantly related to the role of undissociated H_2CO_3, as previously discussed. The electrochemical activity of H_2CO_3 was perhaps first discussed by Linter and Burstein[19] who suggested that it was not directly reduced at the surface of 13 Cr stainless steel and low alloy steel, although these observations were restricted to solutions at pH 4. In 2008, Remita et al.[32], evaluated the electrochemical activity of H_2CO_3 using a rotating disk electrode with N_2 and CO_2-saturated solutions at pH 4. Through the application of a mathematical model it was possible to predict the behaviour of the cathodic reaction in CO_2 environments negating any direct effect from H_2CO_3. Their observations at pH 4 and 25°C with 1 bar CO_2 partial pressure suggested that H_2CO_3 is not electroactive at these conditions. However, in a recent study, Kahyarian et al.[34] argued that both studies suffered from the shortcomings that only a narrow range of operating conditions were considered. In order to address such limitations, Tran et al.[30] focused on clarifying the role of H_2CO_3 by studying the cathodic polarisation behaviour of stainless steels at elevated pressures, enabling its role to be evaluated with more confidence. By comparing the steady-state cathodic polarisation behaviour at pH 4 and pH 5 at CO_2 partial pressures of both 1 and 10 bar, the authors noted no noteworthy difference in the charge-transfer region of the cathodic currents, hence concluding that the 'buffering effect' mechanism takes place even at elevated pressure.[34] However, the sensitivity of the hydrogen evolution reaction is known to be connected to the state of the material surface, meaning that the presence of the oxide film on the electro-activity of the metal surface could be significant.[12] Therefore such results need to be considered with caution. It is important to note the reason for Tran et al.[30] evaluating the cathodic polarisation behaviour of stainless steel as opposed to carbon steel was attributed to the fact that the charge-transfer cathodic currents on X65 steel could not be clearly distinguished due to interference from the anodic reaction. The use of UNS30400

stainless steel by Tran et al.[30] enabled suppression of the anodic reaction which allowed the charge-transfer reactions on the cathodic polarisation plot to be clearly observed.

Kahyarian et al.[34] recently extended the work of Tran et al.[30] using a different approach whereby experiments were conducted at high flow rates (13 m/s), higher CO_2 partial pressure (5 bar) and low temperature (10°C) in order to disproportionately decrease the rate of the anodic reaction relative to the cathodic reactions. In addition to evaluating X65 steel, both pure iron and stainless steel were considered. The results enabled the charge-transfer behaviour to be observed on X65 and iron, which could be compared with stainless steel. The polarisation behaviour across all three materials indicated no significant difference in electro-activity with regards to hydrogen reduction. Furthermore, the cathodic response from all materials showed no significant effect of the direct reduction of H_2CO_3.

Despite the work of Tran et al.[30] and Kahyarian et al.[34], the question still remains as to the behaviour of H_2CO_3 at higher partial pressures beyond 10 bar and whether the direct reduction reaction becomes influential. Recently, de Sousa et al.[35] evaluated the hydrogen evolution reaction on platinum in CO_2 environments using both polarisation curves and electro-hydrodynamic impedance, demonstrating the use of transient techniques in a dynamic (low inertia rotating disk) autoclave system at pressures up to 40 bar. The application of such equipment combined with the aforementioned polarisation and impedance techniques to study the cathodic reaction on carbon steel in such environments could prove valuable to the research community in terms of understanding the chemical-electrochemical processes, aiding the development of models for carbon steel corrosion under high CO_2 partial pressures.

The discussed reaction sequence of specie dissociation at the steel surface followed by H^+ reduction is not exclusive to H_2CO_3, as similar arguments have been put forward for acetic acid (HAc) which is commonly found in CO_2-containing brines[11, 36, 37]. (Note that discussion on hydrogen sulphide and its reaction pathway are outside of the scope of this review, but similar discussions also exist in literature for this weak acid[11]).

Considering HAc, the direct reduction can be expressed using Reaction (4a). However, HAc can also undergo dissociation (Reaction (4b)), producing H^+ ions which can support the previously discussed hydrogen evolution reaction (Reaction (2a)).

$$2HAc_{(aq)} + 2e^- \rightarrow H_{2(g)} + 2Ac^- \tag{4a}$$

$$HAc_{(aq)} \leftrightarrow H^+_{(aq)} + Ac^-_{(aq)} \tag{4b}$$

These two pathways can again be distinguished by studying the behaviour of the charge-transfer controlled cathodic currents as in the work of Tran et al.[30] for identification of the role of H_2CO_3 (as discussed previously). Such analysis has recently been performed by Kahyarian et al.[36, 37] for HAc, where it was clearly indicated that the direct reduction of undissociated HAc is not significant i.e. it contributes to the cathodic current via a buffering effect. This was attributed to the fact that increasing HAc concentration for a constant bulk solution pH resulted in no increase in the charge-transfer reaction. Interestingly, it was found that depending upon whether the corrosion system is charge-transfer controlled or mass-transfer controlled determines the mechanisms by which HAc influences the corrosion rate. When corrosion currents were under mass-transfer control, HAc increased corrosion rates through buffering the H^+ concentration at the metal surface. If charge-transfer processes controlled the corrosion current, then HAc was shown to have an inhibiting effect on both the anodic and cathodic reactions, which was achieved through chemical adsorption onto the steel surface.

Despite the continuing advances in the understanding of the cathodic reactions in CO_2 environments over the years, various aspects still require further clarification. This particularly relates to the electrochemical mechanism of the hydrogen evolution reactions, and the significance of the H_2CO_3, HCO_3^- and longer chain organic acid direct reduction pathways. In addition, a complete study would also require analysis at higher partial pressures of CO_2.

2.2.2 Anodic reactions

In terms of anodic processes, the electrochemical dissolution of iron in acidic media:

$$Fe_{(s)} \rightarrow Fe^{2+}_{(aq)} + 2e^- \tag{5}$$

has been considered by many researchers[38-46]. Within literature, two main mechanisms are proposed for the dissolution of iron; the 'catalytic mechanism' (proposed by Heusler et al.[46]) and the 'consecutive mechanism' (proposed by Bockris et al.[38, 39]), both of which are observed when iron undergoes active dissolution. Both mechanisms were inferred based on steady-state anodic polarisation responses (for which there is now a consensus from literature that elucidating such processes using steady-state techniques is extremely difficult and should be complemented with transient techniques such as impedance measurements)[47].

The anodic polarisation behaviour of carbon steel in CO_2-saturated environments is frequently reported to be around 40 mV/decade, possessing a first order dependence with OH^- concentration. Such behaviour is in agreement with the 'consecutive mechanism' proposed by Bockris et al.[38, 39], which follows the steps outlined in Reactions 6a to 6c. In this mechanism, iron reacts with water to form $(FeOH)_{ads}$, which is then directly oxidised through a one-electron transfer step.

$$Fe_{(s)} + H_2O_{(l)} \leftrightarrow (FeOH)_{ads} + H^+_{(aq)} + e^- \tag{6a}$$

$$(FeOH)_{ads} \rightarrow FeOH^+_{(aq)} + e^- \tag{6b}$$

$$FeOH^+_{(aq)} + H^+_{(aq)} \leftrightarrow Fe^{2+}_{(aq)} + H_2O_{(l)} \tag{6c}$$

The mechanisms proposed by Bockris et al.[38, 39] have commonly been used to describe the anodic reaction in CO_2 environments. However, in 1996 Nesic et al.[48] performed studies which suggested that there does appear to be an effect from CO_2 on the anodic reaction. Based on collected anodic Tafel slopes and galvanostatic measurements, new sets of anodic reactions were proposed. The process comprised of a multi-step mechanism, of which the first step involved the adsorption of CO_2 onto the carbon steel surface, forming $(FeCO_2)_{ads}$. The steps of the reaction mechanism to describe the effect of CO_2 on iron dissolution are shown in Reactions 7a to 7f.

$$Fe_{(s)} + CO_{2(aq)} \leftrightarrow (FeCO_2)_{ads} \tag{7a}$$

$$(FeCO_2)_{ads} + H_2O_{(l)} \leftrightarrow (FeCO_2)OH_{ads} + H^+_{(aq)} + e^- \tag{7b}$$

$$(FeCO_2)OH_{ads} \leftrightarrow (FeCO_2)OH^+_{ads} + e^- \tag{7c}$$

$$(FeCO_2)OH^+_{ads} + H_2O_{(l)} \leftrightarrow (FeCO_2)(OH)_{2\,ads} + H^+_{(aq)} \tag{7d}$$

$$(FeCO_2)(OH)_{2\,ads} \leftrightarrow (FeCO_2)(OH)_{2\,sol} \quad (7e)$$

$$(FeCO_2)(OH)_{2\,sol} + 2H^+_{(aq)} \leftrightarrow Fe^{2+}_{(aq)} + CO_{2(aq)} + 2H_2O_{(l)} \quad (7f)$$

Although the proposed mechanism was not supported with sufficient experimental evidence, the steps were shown to resemble those proposed by Drazic et al.[45]. in which CO_2 adsorption onto the iron surface resulted in the formation of $(FeCO_2)_{ads}$.

The role of CO_2 and its ability to act directly on the steel surface has only been recently re-analysed by Almedia et al.[49] who utilised a two electrode cell within an autoclave system. Through the application of large parallel plate electrodes, impedance measurements could be collected within a high resistivity system of distilled water with dissolved CO_2. Comparisons of impedance plots at open circuit potential in CO_2-saturated distilled water and CO_2-saturated 3.2M NaCl solution at both 1 bar and 30 bar pressure suggested that CO_2 does not act over the free iron surface since the inductive loop associated with the relaxation of water-iron species appeared in all CO_2-saturated solutions evaluated (at pH 4), even when partial pressure was significantly increased. These observations are in contrast to the work of Nesic et al.[48].

Shortly after this publication, Kahyarian et al.[50] suggested that observations by Almedia et al.[49] should not be generalised across all conditions encountered in CO_2 corrosion. They performed their own study to investigate the kinetics of the anodic dissolution reaction using steady-state polarisation curves at pH 4 and 5, and CO_2 partial pressures ranging from 0 to 5 bar. By performing tests at 10°C in a 0.1M NaCl solution with and without CO_2 saturation, Kahyarian et al.[50] found that the presence of CO_2 decreased the Tafel slope value from ~28 mV/decade to ~22 mV/decade in the active dissolution range. They believed that this difference suggested that CO_2 and/or its carbonate species were directly involved in the anodic dissolution reaction, affecting the kinetics at CO_2 partial pressures as low as 1 bar.

In response to the work of Kahyarian et al.[50], Almedia et al.[47] questioned the validity of such observations given that the effect from CO_2 was not detected in their previous paper[49], published in the same journal. They suggested that the use of steady-state Tafel analysis alone is inadequate to fully decipher the anodic dissolution reaction. In their paper, they provide a compelling argument for the use of transient techniques (such as impedance measurements) in addition to Tafel analysis, as the former has the ability to

infer anion participation over a large time domain, and is not limited to steady state conditions.

3. $FeCO_3$ reactions and saturation ratio/supersaturation

In CO_2-containing systems, when the product of the activities of Fe^{2+} and CO_3^{2-} ions exceed the solubility product, K_{sp}, it becomes thermodynamically possible for $FeCO_3$ to precipitate from the solution onto the steel surface and stifle the corrosion kinetics via the formation of a porous crystalline layer.

$FeCO_3$ is believed to occur via a one-stage reaction process with carbonates[11, 15] (Reaction (8)). However, a two-stage reaction involving bicarbonates (Reaction (9a) to (9b)) has also been proposed[51]:

$$Fe^{2+}_{(aq)} + CO^{2-}_{3(aq)} \rightarrow FeCO_{3(s)} \tag{8}$$

$$Fe^{2+}_{(aq)} + 2HCO^{-}_{3(aq)} \rightarrow Fe(HCO_3)_{2(s)} \tag{9a}$$

$$Fe(HCO_3)_{2(s)} \rightarrow FeCO_{3(s)} + CO_{2(g)} + H_2O_{(l)} \tag{9b}$$

The formation of $FeCO_3$ via the involvement of bicarbonate ions was also supported by Davies and Burstein[52] and was stated to consist of 'multiple step reactions'. They postulated that $FeCO_3$ may form from the reaction of bicarbonates with the metal or from $Fe(OH)_2$ reacting with bicarbonate ions, although these reactions were not wholly validated.

In a recent study, Sk et al.[18] correlated *in situ* synchrotron X-ray diffraction with electrochemical measurements for a rotating disc electrode. Through the use of potentiostatic polarisation of the carbon steel electrodes in CO_2-saturated environments at 80°C and various pH values and rotation speeds, they were able to show that the current response comprised of a current due to dissolution of iron (leading to colloidal $FeCO_3$) (Reactions 10a and b) and a current due to the growth of a $FeCO_3$ i.e. an electro-crystallisation reaction (Reaction 11):

$$Fe_{(s)} \rightarrow Fe^{2+}_{(aq)} + 2e^- \tag{10a}$$

$$Fe^{2+}_{(aq)} + CO^{2-}_{3(aq)} \rightarrow FeCO_{3(colloid)} + 2e^- \tag{10b}$$

$$Fe_{(s)} + CO^{2-}_{3(aq)} \rightarrow FeCO_{3(crystalline)} + 2e^- \tag{11}$$

Given the general consensus from literature is that $FeCO_3$ forms via Reaction (8)[7, 12, 15, 53, 54], this is an interesting observation.

Nonetheless, when $FeCO_3$ does accumulate on the steel surface, the morphology and level of protection afforded are strongly related to the rate of formation. The driving force responsible for $FeCO_3$ precipitation is the saturation ratio or supersaturation (S)[55], defined as:

$$S = \frac{a_{Fe^{2+}} a_{CO_3^{2-}}}{K_{sp}} \qquad (12)$$

where $a_{Fe^{2+}}$ and $a_{CO_3^{2-}}$ (in mol/L) are the ferrous and carbonate ion activities, respectively. K_{sp} (in mol^2/L^2) is the solubility product associated with $FeCO_3$. Consequently, any factors which influence K_{sp} or specie activity will affect the characteristics and rate of film formation.

Theoretically, supersaturation levels exceeding 1 initiate the nucleation of $FeCO_3$. Although such nuclei formation is possible at a saturation level of just above unity, its rate rises rapidly only when a saturation ratio of a critical value is exceeded[56]. Principally, two steps are involved in precipitation: nucleation and particle growth.[15] Initially, heterogeneous nucleation takes place on the carbon steel surface, starting the precipitation process. Due to the abundant imperfections (and therefore absorption sites) in the form of defects, dislocations in crystal/grain structures, surface roughness, percentage of ferrite/pearlite, etc., heterogeneous nucleation can easily occur, forming $FeCO_3$ nuclei[25]. Once stable nuclei have developed, crystal growth is then believed to dominate the process, limiting the precipitation rate.

The assumption is that the two processes of nucleation and growth are related to supersaturation. Nucleation rate is said to rise exponentially with saturation value, whilst particle growth increases in a linear fashion. Consequently, particle growth is believed to occur/dominate at lower levels of supersaturation. Conversely, high supersaturation results in nucleation dominating, and a nano-crystalline or amorphous films can form.[56] Lasaga[57] identified four key different regions of crystal nucleation and growth for a generic salt AB based on the concentrations of its constituent ions $[A^+]$ and $[B^-]$. These stages were related by Yang to the crystal growth processes involved with $FeCO_3$[58]. The four regions, showing the increase in the level of saturation from regions 1 to 4 are as follows:

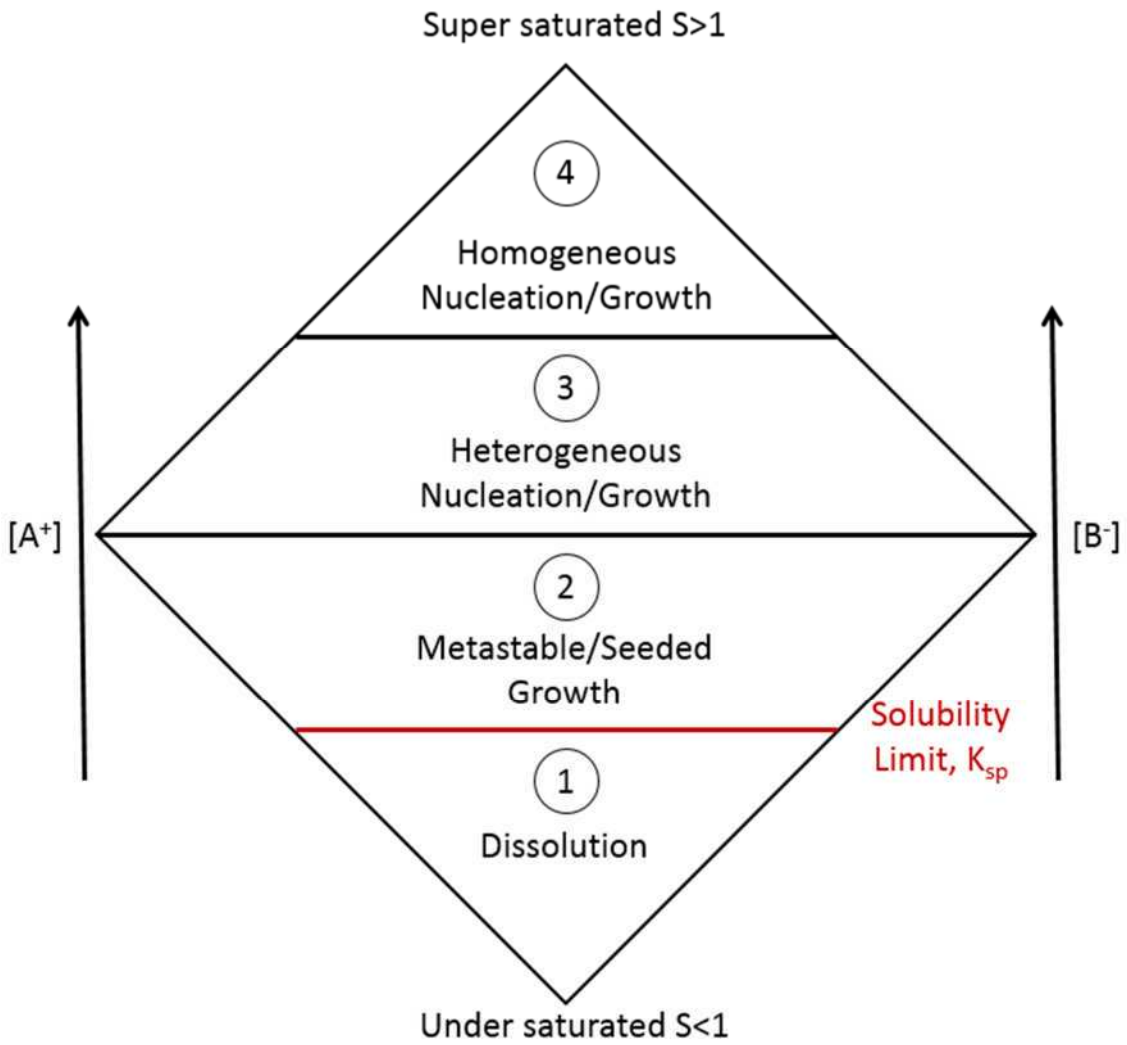

Figure 1: Regions of crystal growth identified by Lasaga[57] – adapted from the work of Lasaga[57]

- Region 1 - Dissolution: The system is under-saturated (S < 1). Consequently no crystal growth occurs and there is the potential for dissolution of the crystal.
- Region 2 – Metastable/Seeded Growth: In this situation, the system is super-saturated (i.e. the solubility limit is exceeded), however, growth will occur on seed crystals only. The system will in fact remain super-saturated for a considerable period of time in the absence of such seed crystals.[59]
- Region 3 – Heterogeneous Nucleation/Growth: Heterogeneous nucleation involves nucleation induced by foreign particles, which is subsequently followed by crystal growth.

- Region 4 – Homogeneous Nucleation/Growth: When saturation is increased further beyond Region 3, spontaneous homogenous nucleation and growth are able to occur.

Regions 3 and 4 involve both nucleation and growth, whilst only crystal growth is possible in Region 2.

4. Factors influencing the kinetics of $FeCO_3$ precipitation

Since $FeCO_3$ precipitation can lead to a significant decrease in the corrosion rate of carbon steel pipelines, it is very important to understand the key controlling parameters in order to develop effective approaches and theoretical models for corrosion management. The following sections focus on the environmental, physical and steel/interfacial properties which control the formation kinetics and morphology of $FeCO_3$, as well as the four main models which exist in the literature to calculate the rate of $FeCO_3$ precipitation/surface accumulation.

4.1 Solubility product of $FeCO_3$

The rate of precipitation has been shown to be strongly related to the level of supersaturation, and consequently, the solubility product (K_{sp})[60, 61]. Reliable calculations of solubility product are critical for developing accurate relationships between supersaturation and precipitation rate. A number of studies have focused on determining $FeCO_3$ solubility[53, 60, 62-74], yet few of them cover a wide enough range to encapsulate the temperatures encountered in CO_2 corrosion (with the exception of the unified expression developed by Sun and Nesic[53] and the correlation by Benezeth et al.[75], which will be discussed in due course).

4.1.1 Solubility product at room temperature

The solubility product of $FeCO_3$ can be determined experimentally by evaluating its precipitation from supersaturated solutions, through either the re-suspension of wet or dry crystals, or the use of a hydrogen-electrode concentration cell[60, 64-69, 72-75]. The predicted values of K_{sp} at room temperature from 10 publications[60, 64-69, 72-74] were evaluated extensively by Sun and Nesic[53]. They concluded that although theoretically, the solubility product should not be affected by any of these methods, the application of the wet crystal technique produced large variations in predicted K_{sp} across a number of

authors[65, 66, 73], ranging from 3.72 ×10^{-11} mol^2/L^2 to 1.17 ×10^{-11} mol^2/L^2 at room temperature.

4.1.2 Relationship between solubility product and temperature

The dependence of $FeCO_3$ solubility on temperature has been widely studied, with several models being developed[53, 59, 60, 63, 69, 75]. Table 3 summarises the solubility models available within literature which have been developed through experimental work[60, 61, 69, 75] or by the use of theoretical thermodynamic models[70, 71]. The models are also plotted in Figure 2 for comparative purposes. It is perhaps worth noting here that the result of Braun[69] could potentially be misleading as an artificial buffer was introduced into the system to control the pH, which may have led to errors in the results. Regardless of the results of Braun, the predicted values vary quite dramatically between each model as a function of temperature.

Perhaps one of the most common models for K_{sp} in Table 3 is that of Greenberg and Tomson[60, 61] who conducted a number of tests to determine $FeCO_3$ solubility from 25 to 94°C. The solubility constant temperature dependence was analysed using the equation suggested by Nordstrom et al.[62]:

$$log(K_{sp}) = a - bT_K - \frac{c}{T_K} + dlog(T_K) \qquad (13)$$

where T_K relates to temperature in units of degrees Kelvin.

Table 3: Solubility product (K_{sp}) prediction models for $FeCO_3$ from various authors

Author	Mathematical model	
Greenberg and Tomson[60]	$log(K_{sp}) = -59.2385 - 0.041377(T_K) - \frac{2.1963}{T_K} + 24.5724log(T_K)$	(14)
Johnson and Tomson[76]	$log(K_{sp}) = -0.4343\left(\frac{-30140}{8.314(T_K)} + 36.22\right)$	(15)
Marion et al.[63]	$log(K_{sp}) = -14.66 + \frac{1365.17}{T_K}$	(16)
Institute for Energy (identified by Sun and	$log(K_{sp}) = -10.13 - 0.0182(T_C)$	(17)

Nesic[53] and developed from the work of Helgeson et al.[71])		
Braun[69]	$log(K_{sp}) = -10.2 - 0.0314(T_c)$	(18)
Sun and Nesic[77]	$log(K_{sp}) = -59.3498 - 0.041377(T_K) - \frac{2.1963}{T_K} + 24.5724log(T_K)$	(19)
Benezeth et al.[75]	$log(K_{sp}) = 175.568 + 0.0139(T_K) - \frac{6738.483}{T_K} - 67.898\log(T_K)$	(20)

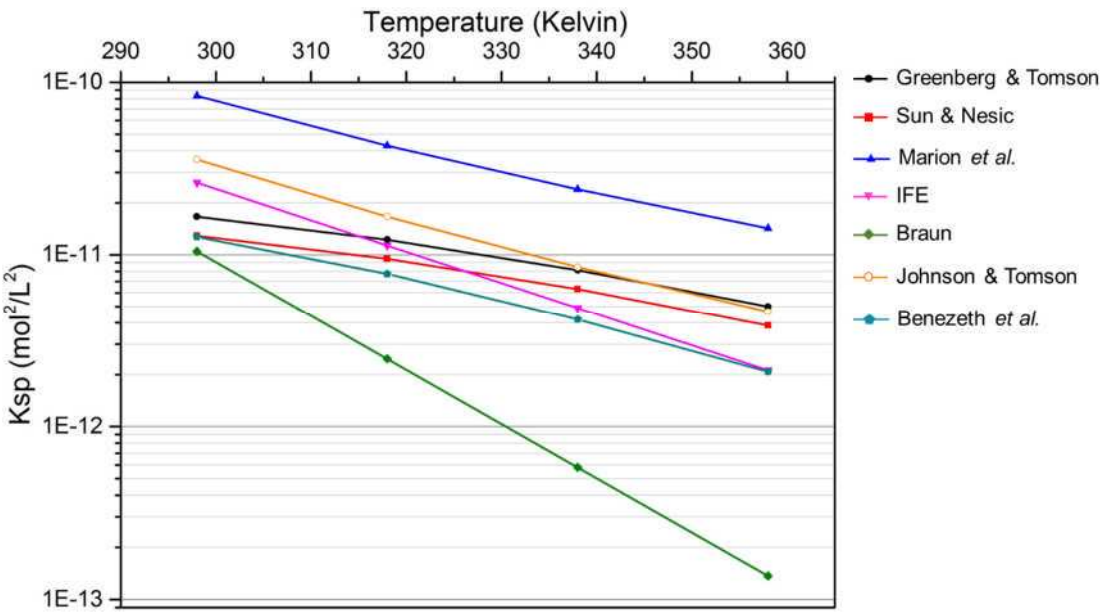

Figure 2: Plots of solubility models for $FeCO_3$ as a function of temperature

4.1.3 Role of ionic strength

Although not strictly influencing the solubility of $FeCO_3$, researchers have included ionic strength into K_{sp} models to enable the concentrations of Fe^{2+} and CO_3^{2-} to be used within Equation (12) as opposed to their corresponding activities when determining the saturation ratio.

The ionic strength of a solution is defined as:

$$I = \frac{1}{2}\sum_i c_i z_i^2 = \frac{1}{2}(c_1 z_1^2 + c_2 z_2^2 + \cdots) \qquad (21)$$

where c_i are the specie concentrations in the aqueous solution in mol/L and z_i is the specie charge.

Silva et al.[64] investigated the solubility of $FeCO_3$ in NaCl solutions experimentally. Through considering solubility behaviour from ionic strengths between 0.1 and 5.5, the following equation was proposed for K_{sp} at room temperature:

$$log(K_{sp}) = -10.9 + 2.518(I^{0.5}) - 0.657(I) \tag{22}$$

The incorporation of this ionic strength expression into the K_{sp} correlation as a function of temperature was performed by Sun and Nesic[53, 77]. After analysing the models summarised in Table 3, they recommended the model developed by Greenberg and Tomson, but noted that its underpinning assumption of zero ionic strength for the experiments performed was unrealistic for the chemistry considered in their experiments.[77] They therefore proposed the following modified equation:

$$log(K_{sp}) = -59.3498 - 0.041377(T_K) - \frac{2.1963}{T_K} + 24.5724log(T_K) \tag{23}$$

which is valid for I=0.

Incorporating ionic strength based on observations by Silva et al.[64] produced the final unified equation, enabling concentrations to be used in Equation (12) as opposed to activities to determine saturation levels:

$$log(K_{sp}) = -59.3498 - 0.041377(T_K) - \frac{2.1963}{T_K} + 24.5724log(T_K) + 2.518(I^{0.5}) - 0.657(I) \tag{24}$$

Figure 3 indicates the effect of varying ionic strength on K_{sp} using the Sun and Nesic model.[54] The plots show that the solubility of $FeCO_3$ increases in conjunction with ionic strength. However, K_{sp} becomes less sensitive to changes in the ionic strength as it approaches higher values of the latter.

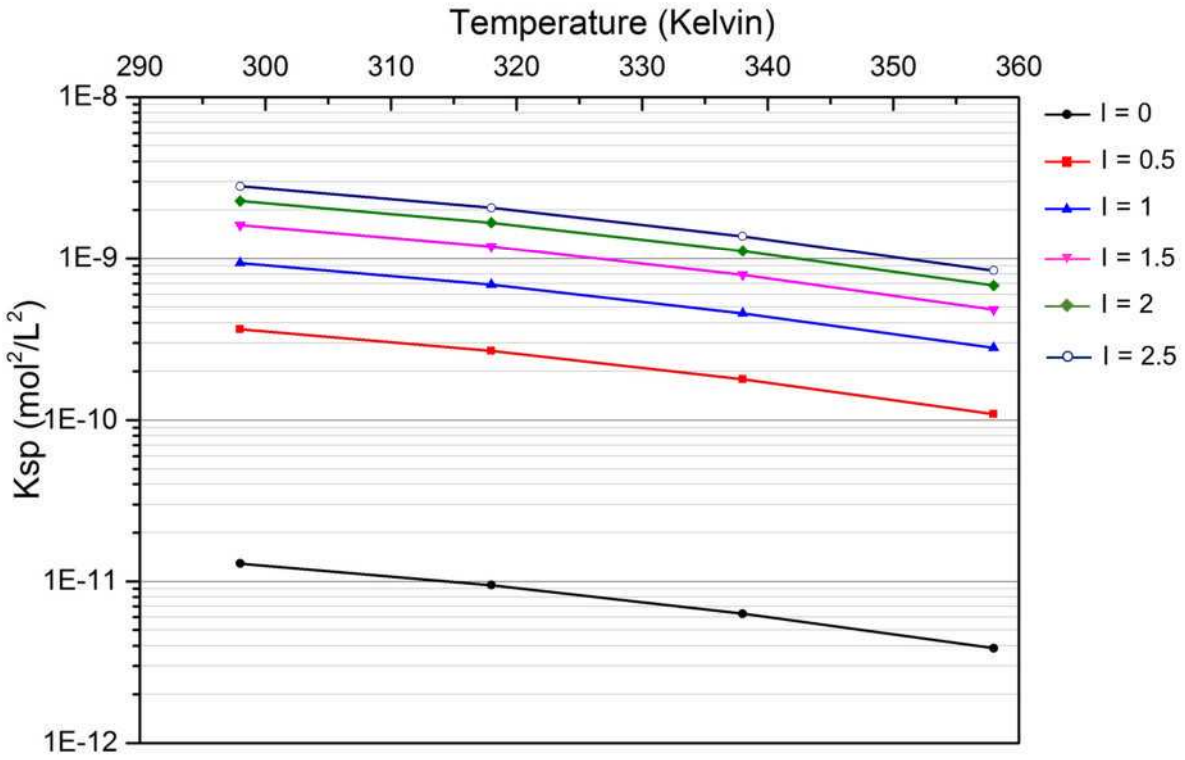

Figure 3: Plots of $FeCO_3$ solubility product (K_{sp}) as a function of temperature for varying levels of ionic strength from 0 to 2.5 using the Sun and Nesic[53] model.

4.2 Effect of environmental conditions on precipitation

4.2.1 pH

Due to the relatively slow kinetics of $FeCO_3$ precipitation, it is believed that supersaturation has to be exceeded at the steel surface by a factor of 10-100 to form a protective layer.[11] System pH could be considered as one of the most influential factors which controls the rate of $FeCO_3$ precipitation, as increasing pH reduces the Fe^{2+} concentration required to exceed $FeCO_3$ solubility significantly, promoting film formation[78-81]. Figure 4, taken from Dugstad et al.[15] for a 1 wt.% NaCl solution, shows how the Fe^{2+} level needed for $FeCO_3$ saturation depends on pH. It shows that the solubility of Fe^{2+} can be increased by factors of 100 and 5 by reducing pH from 6 to 5 and then from 5 to 4, respectively. This effect is very important since a higher solubility leads to smaller rates of precipitation for the same Fe^{2+} content in the bulk solution.[8]

Importantly, the Fe^{2+} concentrations shown in Figure 4 are those required to saturate the bulk solution. Due to the rise in pH at the vicinity of the steel surface (as discussed later), even lower concentrations of Fe^{2+} would be required to facilitate saturation locally with

respect to $FeCO_3$. Furthermore, the solubility curves in Figure 4 are not parallel and cross in the range 4.5 to 5 at different partial pressures which will be discussed further in subsequent sections.

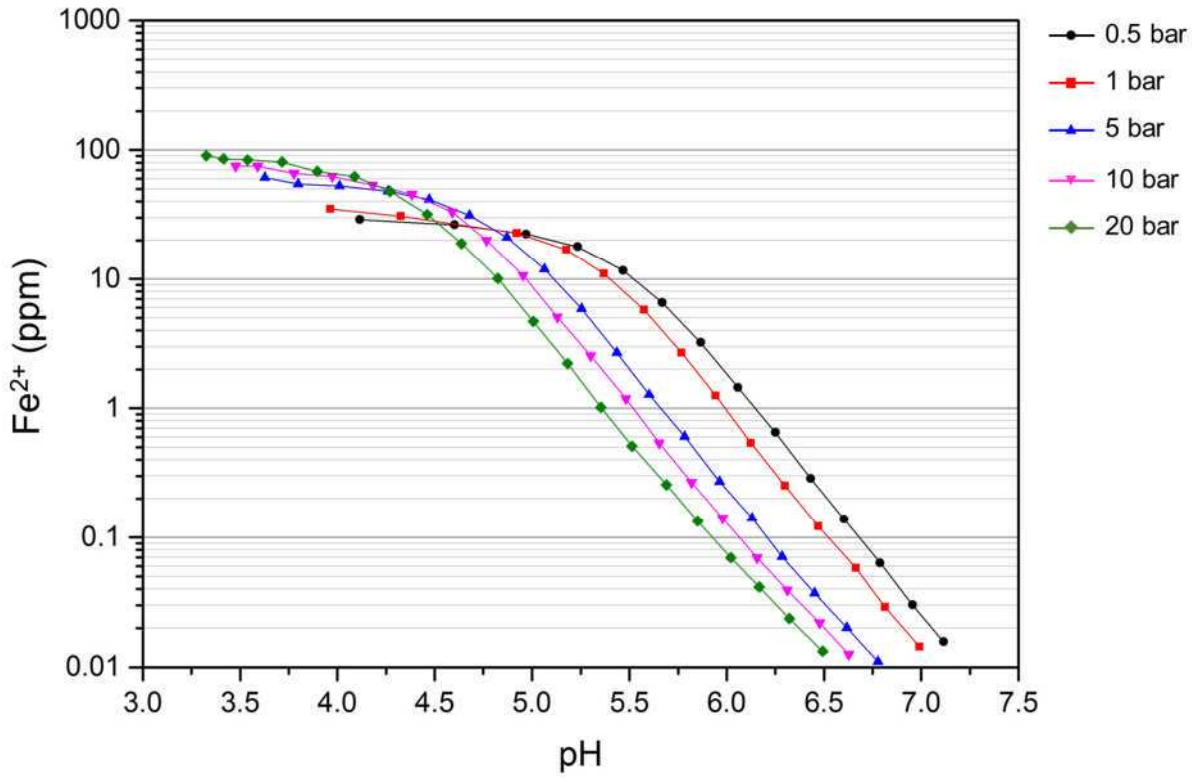

Figure 4: Amount of Fe^{2+} required to reach $FeCO_3$ saturation in a 1 wt.% NaCl solution as a function of pH for different CO_2 partial pressures – adapted from Dugstad et al.[15] and reproduced with permission from NACE International, Houston, TX. All rights reserved.

Pessu et al.[82] used an experimental method in which X65 steel was immersed in a 3.5 wt.% NaCl solution for 168 hours at 50°C , to explore the effect of pH on the precipitation kinetics, morphology and protectiveness of $FeCO_3$ films. They found that pH had a significant effect on the morphology and protectiveness of the corrosion films (see Figure 5). As pH was increased from 3.8 to 6.6 and then to 7.5, non-protective, amorphous/nano-polycrystalline $FeCO_3$ films were replaced, respectively, by protective, cubic ones and then by highly protective ones with rhombohedral structure.

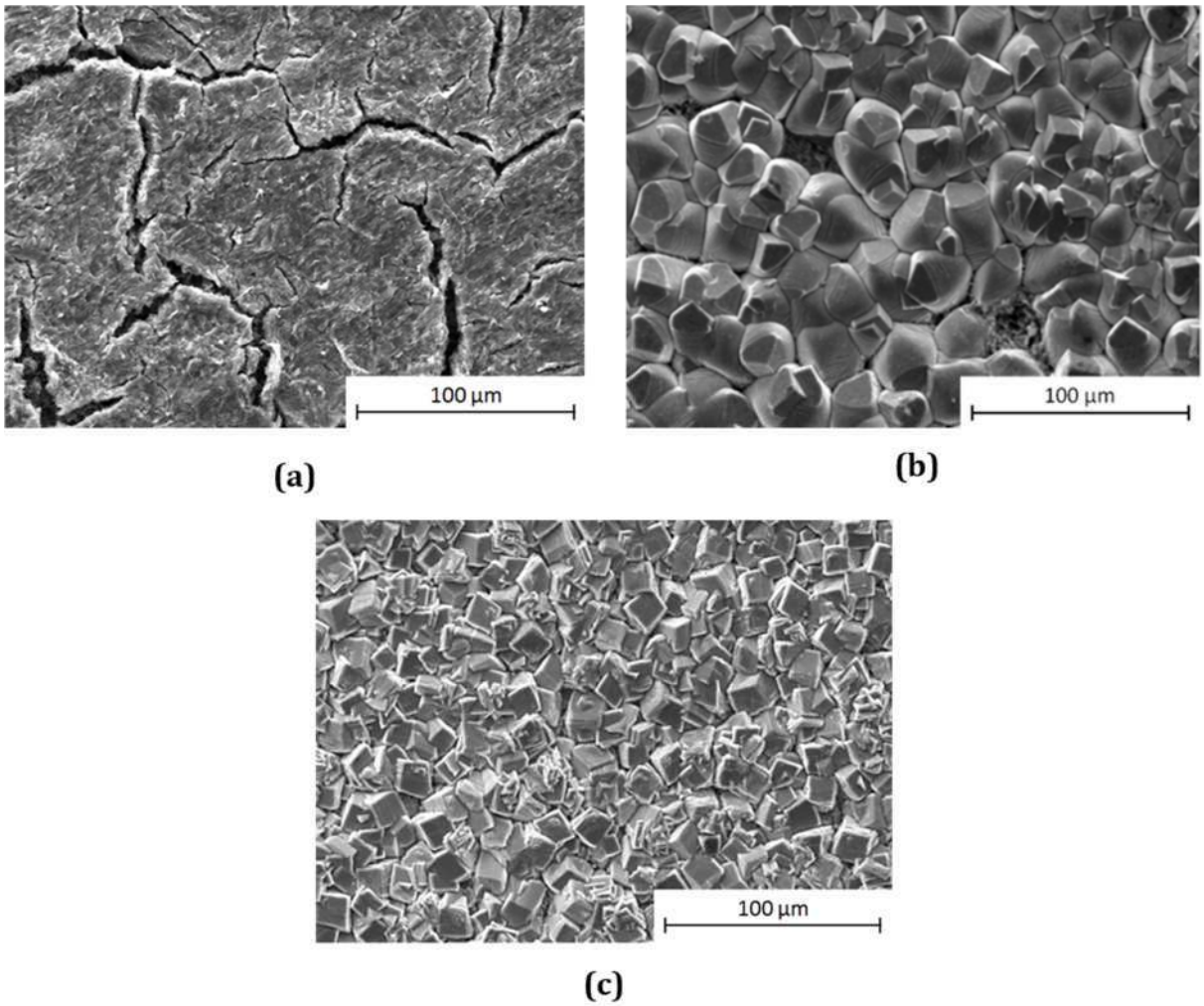

Figure 5: SEM images of X65 steel surfaces after exposure to a 3.5 wt.% NaCl solution at a temperature of 50°C for 168 hours; (a) starting pH of 3.8 (b) pH 6.6 and (c) pH 7.5 – adapted from Pessu et al.[82] and reproduced with permission from NACE International, Houston, TX. All rights reserved.

In other studies, van Hunnik et al.[83] suggested that at low temperatures, the pH has to exceed 6 in order for protective film formation to occur. Similar conclusions were made by Nazari et al.[84] who performed experiments over 72 hours across a range of temperatures (55 to 85°C) and pH (5.5 to 6.5). At 55°C, no corrosion product was observed at any pH in the aforementioned range. Increasing temperature to 65°C promoted the formation of $FeCO_3$ at all conditions which had a non-compact morphology, but coverage of the layer improved with increasing pH. Raising temperature to 75°C resulted in a compact, protective layer forming at all pH values, but the most protective layer was observed at pH 6.5. The work highlighted a noticeable synergy between temperature and pH, which both play a role in the kinetics of film formation.

4.2.2 Brine chemistry

Solution chemistry is extremely important and can dramatically influence the precipitation kinetics of $FeCO_3$ through its effect on:

- the corrosion rate (influencing the flux of Fe^{2+} ions at the steel surface) which changes the local pH and concentrations of the other chemical species
- the activity of Fe^{2+} and CO_3^{2-} which influences $FeCO_3$ saturation levels
- the formation of other mineral scales and mixed carbonates such as $Fe_xCa_{1-x}CO_3$.

The influence of salt or chloride concentration on corrosion rate needs to be considered carefully. Literature indicates that the addition of NaCl results in an increase, followed by a non-linear reduction in corrosion rate beyond a certain value for systems where CO_2 partial pressure is maintained[85, 86]. Under these circumstances, such observations relating to the reduction in corrosion rate with increased brine salinity can at least partly be attributed to the fact that NaCl decreases CO_2 solubility, lowering the dissolved CO_2 content. Almeida et al.[49] highlighted this concept, stating that the dissolved CO_2 concentration in distilled water was approximately twice that in a 3.2 mol/L NaCl solution when saturated at room pressure. By performing mass loss and electrochemical measurements in distilled water saturated with 1 bar CO_2 partial pressure, and 3.2 mol/L NaCl solution saturated with 0.437 bar CO_2 partial pressure (both adjusted to pH 4), they were able to show that NaCl does reduce corrosion rate when the dissolved gas concentration and pH are equal at room temperature.

In the context of brine chemistry and its influence on film formation, laboratory experiments tend to be conducted in dilute NaCl-containing brine, resulting in $FeCO_3$ being the most commonly observed corrosion product[3, 87-89], along with magnetite (Fe_3O_4) at elevated temperature[90, 91].

Although the protective properties of $FeCO_3$ have been shown to be sensitive to ionic specie activity, temperature, pH and CO_2 partial pressure to name a few, the influence of brine chemistry has received significantly less attention. However, in addition to sodium (Na^+) and chloride (Cl^-), calcium (Ca^{2+}) and magnesium (Mg^{2+}) ions are commonly found within process fluids. The presence of these divalent salts can result in the precipitation of calcium carbonate ($CaCO_3$) and magnesium carbonate ($MgCO_3$). These mineral scales differ in that the source of the cation for $CaCO_3$ and $MgCO_3$ is typically from the formation, whereas the cation is produced predominantly from the corrosion process for $FeCO_3$.

Despite the likely presence of Ca^{2+} and Mg^{2+} in the formation brines, their effects on corrosion product formation on carbon steel in CO_2 environments, as well as the effects on corrosion product morphology, structure and chemistry have received little attention. One may attribute this to the fact that $CaCO_3$ and $MgCO_3$ are mineral scales and $FeCO_3$ is typically classified as a corrosion product, and as such, the two classes of minerals tend to be dealt with separately by different research groups.

Both Ca^{2+} and Mg^{2+} are divalent cations, and given their ability to form carbonates with similar structures to $FeCO_3$, as well as their abundancy in process fluids, they have the potential to alter the CO_2 corrosion mechanism. The isostructurality of $CaCO_3$ and $MgCO_3$ results in Ca^{2+} and Mg^{2+} holding the ability to substitute themselves for Fe^{2+} in the $FeCO_3$ lattice or to co-precipitate with the corrosion product, either of which can theoretically modify the morphology and protectiveness of the developed layer. Furthermore, this question of whether co-precipitation of substitution causes the formation of mixed corrosion products is important, as the kinetics of each process are likely to be very different.

Shannon and co-workers[92] were perhaps one of the first groups to establish that solution chemistry modifies the protective properties of $FeCO_3$. Their results suggested that the protective properties of $FeCO_3$ and the ability for the $FeCO_3$ crystals to adhere to the steel substrate can be enhanced through the addition of Mg^{2+} ions to the solution. Recently, Ingham et al.[93] utilised *in situ* synchrotron radiation X-ray diffraction (SR-XRD) to monitor the precipitation of $FeCO_3$ in real-time with the introduction of magnesium chloride ($MgCl_2$) into the brine solution. Their results demonstrated that the addition of Mg^{2+} reduced the induction time of $FeCO_3$ nucleation. These tests, however, were performed using potentiostatic or galvanostatic electrochemical methods to drive the corrosion reaction. During the experiments, the anodic current density was driven in excess of 10 mA/cm^2 (equivalent to in excess of 100 mm/year corrosion rate). Such a technique at high anodic currents could be regarded as being unrepresentative of a metal corroding naturally, altering the kinetics of $FeCO_3$ formation significantly. Ingham et al.[93] claimed that $MgCl_2$ (added as 0.02, 0.05 or 0.1M within a 0.5M NaCl solution) decreased the critical supersaturation required for precipitation, and also promoted the formation of chukanovite ($Fe_2(OH)_2CO_3$) in conjunction with, but following $FeCO_3$ formation. Although traces of magnesium were identified within the corrosion product layer for

experiments with the highest $MgCl_2$ content, there was no evidence to suggest that magnesium had incorporated into the formed corrosion product.

Ding et al.[94] evaluated the corrosion of carbon steel in simulated stratum water at 10 bar and 75°C in the presence of varying concentrations of Ca^{2+}. They observed an increase in corrosion rate with increasing Ca^{2+} concentration from 256 to 512 mg/L, whilst also reporting that mixed iron-calcium carbonate ($Fe_xCa_{1-x}CO_3$) formed on the steel surface, and that the Fe^{2+} in the corrosion product was gradually replaced by more Ca^{2+} as the calcium content in the brine increased. The corrosion product was analysed using X-ray diffraction (XRD) and characterised as a mixed carbonate through the observation of shifts in the $FeCO_3$ peak positions with increasing Ca^{2+} presence in the layer. (Such a shift is a result of the change in the unit cell of the corrosion product.) Ding et al.[94] also performed experiments with brine containing both 512 mg/L Ca^{2+} and 78 mg/L Mg^{2+}, but stated that there was no indication of the presence of magnesium in the corrosion product.

In another study, Gao et al.[95] performed autoclave experiments in static and dynamic conditions to evaluate the corrosivity of a CO_2-saturated brine towards carbon steel. The brine in question contained 64 mg/L Ca^{2+} and 78 mg/L Mg^{2+} and CO_2 partial pressure was varied at 1, 3 and 10 bar. Gao et al.[95] observed the precipitation of individual phases of $FeCO_3$, $CaCO_3$ and $MgCO_3$ at 1 bar CO_2 under static conditions while higher pressures resulted in the formation of mixed carbonates. Under dynamic conditions and higher CO_2 partial pressures, there was no evidence of magnesium presence within the corrosion product layer, however, in static conditions at 3 bar CO_2, the corrosion product was reported to be '$(Fe,Mg,Ca)CO_3$'. In a similar fashion, Zhao et al.[96] conducted experiments for 72 hours on P110 carbon steel in a brine solution containing 6000 ppm Ca^{2+} and 1000 ppm Mg^{2+} at 25 bar pressure and 90°C. In these experiments, the corrosion product was described as '$Fe(Ca,Mg)(CO_3)_2$'.

Adopting a different approach, Tavares et al.[97] performed 28 day experiments to look at the effects of solid $CaCO_3$ addition to brine solutions on the corrosion rate of carbon steel at 80°C and 150 bar in a CO_2-saturated 6.4 mol/L NaCl solution. $CaCO_3$ powder was dosed at a concentration 10 times the mineral saturation limit within the test solution. The corrosion product produced on the steel surface was shown to exist as $Fe_xCa_{1-x}CO_3$ compared to $FeCO_3$ in the absence of $CaCO_3$. The Ca-containing film was described as

being more porous and it was suggested that the layer increased susceptibility of the substrate to Cl^- penetration, and as a result, pitting.

In a more recent study, Esmaeely et al.[98] systematically evaluated the influence of Ca^{2+} on $FeCO_3$ formation onto a corroding surface. Their study considered the effect of Ca^{2+} ions on the corrosion mechanisms of AISI 1018 carbon steel in a 1 wt.% NaCl solution saturated with CO_2 at 80°C, pH 6.6 and concentrations of 10, 100, 1000 and 10,000 ppm Ca^{2+}. At low concentrations of Ca^{2+} (10 and 100 ppm), their results showed that the corrosion rate reduced with time in conjunction with the precipitation of $FeCO_3$ or mixed carbonate ($Fe_xCa_{1-x}CO_3$). At elevated concentrations of Ca^{2+}, the solution was saturated with high levels of Ca^{2+} which prevented $FeCO_3$ precipitation, and favoured $CaCO_3$ precipitation, resulting in a porous, non-protective film forming, consisting of $CaCO_3$ polymorphs. Using XRD patterns, they were able to show that the isostructuality of $CaCO_3$ and $FeCO_3$ enabled the co-precipitation of Ca^{2+} and Fe^{2+} with CO_3^{2-}, altering the chemical and morphological properties of the corrosion product layer. Through calculation of the mole fraction of Ca^{2+} in $Fe_xCa_{1-x}CO_3$ they determined that when the Ca^{2+} mole fraction approached 1, the protectiveness of the layer diminished in static conditions. Additionally, in static conditions with high Ca^{2+} content, localised corrosion was observed. Given that the Cl^- content in each experiment remained constant, it was suggested that Ca^{2+} was responsible for the initiation of localised corrosion. However, it is possible that this effect could be attributed to acidification of the test solution due to initially rapid precipitation of $CaCO_3$.

Very little attention has been paid to the precipitation of mixed iron-calcium carbonates in comparison to other carbonate species within literature, despite the fact that the formation of $Fe_xCa_{1-x}CO_3$ has been observed in several water treatment plants and oil wells.[99-102] It is clear that the presence of Ca^{2+} ions can result in the formation of a mixed carbonate scale which appear to influence both the general and localised corrosion behaviour of carbon steel, at least in low pressure environments. However, the precipitation of Mg-containing corrosion scales appears not to have been fully confirmed, although magnesium presence within corrosion products has been reported. One area that also remains unexplored relates to identifying the factors responsible for controlling the stoichiometry of such films. Typically, authors report the Ca^{2+} and Mg^{2+} concentrations within the brine, correlating such concentrations with the film chemistry.

However, arguably more useful parameters to correlate against would be the respective saturation ratios of the pure phases and their individual precipitation kinetics. Such correlations were established by Alsaiari et al.[99, 103, 104], who performed a number of studies using a continuous stirred tank reactor (CSTR) to observe the precipitation of $Fe_xCa_{1-x}CO_3$. They derived an equation relating the solid solution stoichiometry to both specie activity in the brine, their equilibrium activities and the precipitation kinetics of each pure mineral. They suggested that the molar fraction of Fe (χ_{Fe}) within $Fe_xCa_{1-x}CO_3$ can be expressed in the form of a logistical function:

$$\chi_{Fe} = \frac{1}{1 + k\frac{(a_{Ca^{2+}} - a_{Ca^{2+},eq})a_{Ca^{2+}}}{(a_{Fe^{2+}} - a_{Fe^{2+},eq})a_{Fe^{2+}}}} \tag{25}$$

where $a_{Ca^{2+}}$ is the activity of Ca^{2+} in the system, $a_{Ca^{2+},eq}$ is the activity of Ca^{2+} at equilibrium, $a_{Fe^{2+}}$ is the activity of Fe^{2+} in the system, $a_{Ca^{2+},eq}$ is the activity of Fe^{2+} at equilibrium and k is the ratio of rate constants for the precipitation of the two pure phases of $CaCO_3$ and $FeCO_3$:

$$k = \frac{k_{CaCO_3}}{k_{FeCO_3}} \tag{26}$$

Therefore, the composition of the precipitated layer is theoretically related to both the individual precipitation kinetics of each pure mineral, their individual solubility characteristics (i.e. the degree to which they exceed the equilibrium activity) and the activities of the ionic species participating in the precipitation reaction. It is important to realise that the precipitation of one specie is capable of impairing the other, as they compete for the CO_3^{2-} ions in the precipitation reaction. It has also been suggested that the difference in characteristic water loss rate constant of the free ions in the solution can influence the stoichiometry, as well as the difference in interfacial free energy of the pure endmembers and the different values of the energy barriers[105].

4.2.3 Presence of acetic acid

The presence of acetic acid (HAc) and other organic acids increases the complexity of the brine chemistry, and its influence on CO_2 corrosion has been discussed in detail by Crolet and Bonis[106], Gulbrandsen[107], Hedges and McVeigh[108] and Dugstad[15]. Section 2.2.1 provides details relating to the role of HAc in the electrochemical reactions, whereas this

section focuses exclusively on its influence on brine chemistry and the impact on corrosion product formation.

HAc is a weak acid that is readily soluble in water. Contrary to the beliefs of a number of authors, HAc is not a stronger acid than carbonic acid. This misconception is related to the fact that dissolved CO_2 as well as H_2CO_3 is often included in the term 'carbonic acid' within some papers. This is reflected in Table 4 where the inclusion of $CO_{2(aq)}$ in the dissociation term (Equation (28)) produces a dissociation constant of 4.47×10^{-7} at 25°C (the inclusion of CO_2 with H_2CO_3 is termed as $H_2CO_3^*$ in the reaction here). However, the true dissociation constant of H_2CO_3 is 2.5×10^{-4}, which is actually higher than that of HAc which is 1.75×10^{-4}, indicating that H_2CO_3 is a stronger acid that HAc.

Table 4: Dissociation reactions and their respective values at 25°C for H_2CO_3 and HAc. ($H_2CO_3^*$ represents the combination of H_2CO_3 and $CO_{2(aq)}$ to highlight misinterpretations made regarding the strength of H_2CO_3 as an acid)

Dissociation reaction	*Dissociation expression*	*Value at 25°C and I=0*	
$H_2CO_{3(aq)} \leftrightarrow H^+_{(aq)} + HCO^-_{3(aq)}$	$K_{ca} = \frac{[H^+][HCO_3^-]}{[H_2CO_3]}$	$K_{ca} = 2.5 \times 10^{-4}$ *[109]*	*(27)*
$H_2CO^*_{3(aq)} \leftrightarrow H^+_{(aq)} + HCO^-_{3(aq)}$	$K_{ca^*} = \frac{[H^+][HCO_3^-]}{[H_2CO_3] + [CO_{2(aq)}]}$	$K_{ca^*} = 4.47 \times 10^{-7}$ *[109]*	*(28)*
$HAc_{(aq)} \leftrightarrow H^+_{(aq)} + Ac^-_{(aq)}$	$K_a = \frac{[H^+][Ac^-]}{[HAc]}$	$K_a = 1.75 \times 10^{-5}$ *[110]*	*(29)*

The concentrations of HAc are typically a few mM in oilfield brines, however, concentrations of more than 10 mM have been reported in some fields[10]. The presence of HAc has the ability to both decrease solution pH and solubilise Fe^{2+}, which can have implications on the integrity of the $FeCO_3$ film and/or hinder its formation. The effect of HAc was clearly illustrated in experiments by Hedges and McVeigh[108] in which an increase in HAc concentration resulted in progressively higher initial corrosion rates and an extended delay prior to $FeCO_3$ film formation occurring.

HAc is capable of decreasing solution pH (which has the knock-on effect of increasing the solubility of $FeCO_3$). However, only one study is available within literature which evaluates the effect of HAc in a buffered system i.e. determines whether HAc plays any role on $FeCO_3$ formation other than that associated with the change in pH. This study was performed by Nafday and Nesic[111] who monitored the growth of $FeCO_3$ in a 3 wt.% NaCl solution at 80°C and pH 6.6. Free HAc concentrations of 0, 18, 72 and 180 ppm (0 to 10000 ppm HAc total) were evaluated with the addition of 10 and 50 ppm Fe^{2+} at the start of each experiment to encourage the growth of $FeCO_3$. In all instances, the same $FeCO_3$ film was developed (with the same thickness and level of protection) irrespective of the HAc concentration.

However, these observations by Nafday and Nesic[111] should not be generalised across all conditions. This is particularly true in light of the analysis performed by Dugstad[10] on the role of HAc in determining the Fe^{2+} concentration required to reach $FeCO_3$ saturation over a range of experimental conditions. Dugstad[10] demonstrated that when $FeCO_3$ precipitation is considered, the system becomes particularly complex in the presence of HAc. As also highlighted by Gulbrandsen[107], Fe^{2+} is able to form complexes with acetate (Reactions 30 and 31) resulting in a greater Fe^{2+} content being required in the brine solution to achieve $FeCO_3$ saturation for a given pH.

$$Fe^{2+} + Ac^{-} \leftrightarrow FeAc^{+} \tag{30}$$

$$Fe^{2+} + 2Ac^{-} \leftrightarrow FeAc_2 \tag{31}$$

Figure 6 is adapted from the work of Dugstad and presents results from equilibrium models used to estimate the shift in pH and Fe^{2+} concentration required to reach $FeCO_3$ saturation for HAc concentrations of 0, 0.1, 1 and 10 mM. Figure 6 indicates that the increase in Fe^{2+} concentration required to reach $FeCO_3$ saturation is greatest at low values of pH. Dugstad reported that the increase was approximately 0.2, 3 and 8 times when the undissociated HAc concentration was 0.1, 1 and 10 mM, respectively. Towards higher values of pH (such as those evaluated by Nafday and Nesic[111]) the effect of HAc on $FeCO_3$ solubility appears minimal. This may explain the reasons behind Nafday and Nesic observing no particular effect of HAc on $FeCO_3$ precipitation in a buffered system at pH 6.6. Further analysis should be conducted under conditions where HAc appears to

have a more substantial effect on the Fe^{2+} concentration required to reach $FeCO_3$ solubility, to validate the response of the simulations in Figure 6.

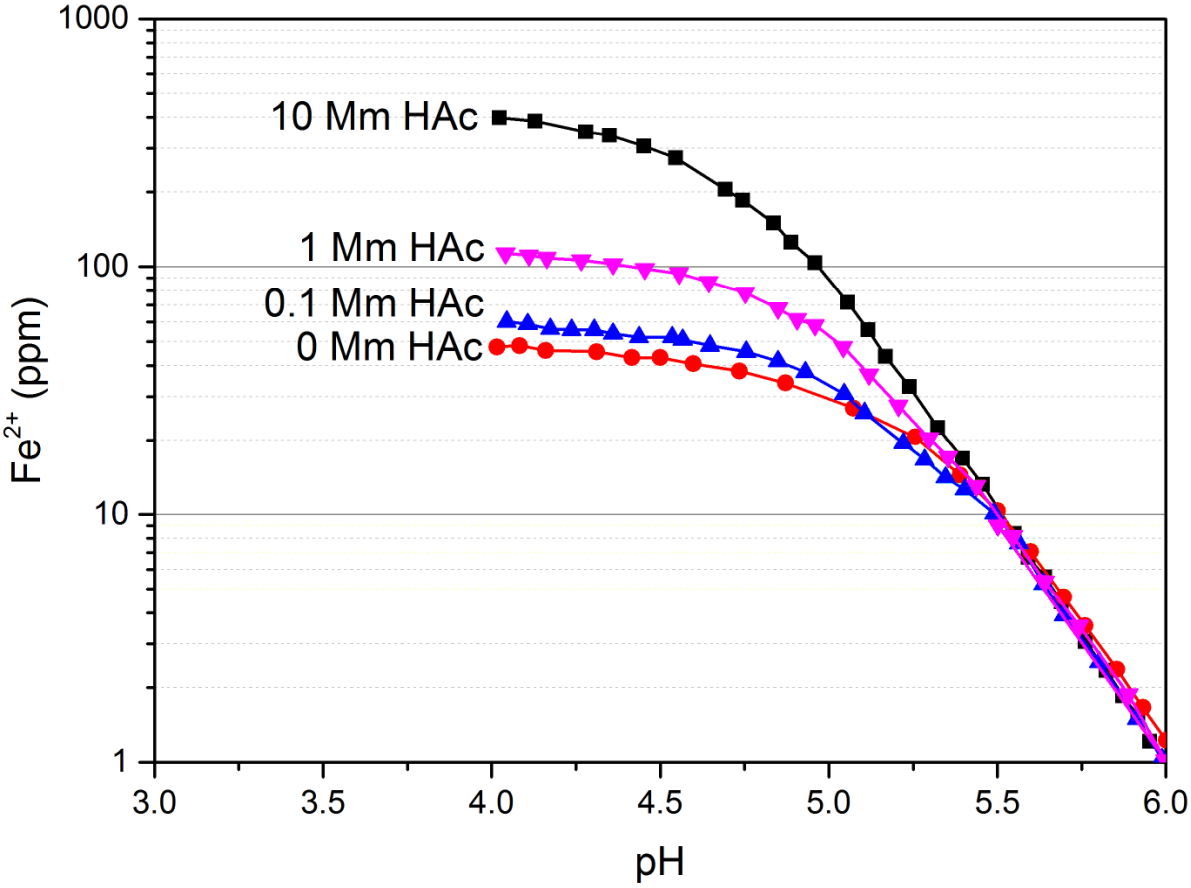

Figure 6: Fe^{2+} concentration required to reach $FeCO_3$ saturation in a 1 wt.% NaCl solution at 1 bar CO_2, plotted as a function of pH for different HAc concentrations – adapted from Dugstad et al.[15] and reproduced with permission from NACE International, Houston, TX. All rights reserved.

4.2.4 Fe^{2+} ions and their source

One important question in the precipitation of $FeCO_3$ is whether the ions which comprise the corrosion product predominantly come from those released by the steel surface or from the bulk solution when the system is supersaturated. Sun and Nesic[54] performed a series of 'free drift' corrosion experiments whereby X65 samples were placed in supersaturated static solutions at pH 6.6 and a range of temperatures. Both the rate of $FeCO_3$ film formation and corrosion rate were determined using the weight-change method and it was found that the rates of both these processes were of similar order of

magnitude, suggesting that corrosion rate of the steel surface has a significant effect on the accumulation rate of $FeCO_3$. This is expected to be the case, particularly at low supersaturation and low temperatures. The observations were re-enforced using tests performed on stainless steel samples which possessed a negligible corrosion rate in CO_2 conditions, releasing minimal Fe^{2+} ions into the solution. For the same experimental conditions (pH 6.6 and 80°C), carbon steel produced a very dense crystalline layer at a saturation ratio of 60, whereas almost no crystals formed on stainless steel. However, increasing the saturation level to 300 resulted in a greater level of precipitation onto stainless steel, but this was still not as substantial as that on the surface of carbon steel. These results suggest that precipitation is influenced by both the corrosion rate and the bulk water chemistry, although further work is required to determine their exact influence on the kinetics of the formation process. However, care should be exercised when drawing conclusions from precipitation experiments onto stainless steel as this may strictly not be analogous to a non-corroding carbon steel surface.

4.3 Effect of operating conditions on precipitation

4.3.1 Temperature

The crucial aspect of the film formation process is the stage of initiation. When both temperature and the level of supersaturation in the bulk solution are high, significant accumulation of corrosion product will occur and a protective $FeCO_3$ film is likely to form. At elevated temperatures, the development of $FeCO_3$ is faster and supersaturation is low, resulting in the formation of dense, crystalline films, offering good protection. Tomson et al.[102] also stated that at higher temperatures, $FeCO_3$ would rapidly nucleate and develop a thin, tight surface film. Dugstad[15] stated that below a temperature of 40°C, precipitation rates are low and the relative supersaturation becomes particularly high, which has the potential to result in a porous film that is loosely adherent, exhibits poor crystallinity and lacks the protection observed at higher temperature.

Although there is a consensus in the literature that the protectiveness, kinetics and adhesion of $FeCO_3$ films increases with temperature, no such consensus exists around the critical temperature above which $FeCO_3$ films form. Studies by Videm and Dugstad[112] and Pessu et al.[82], for example, showed that film can form at around 50°C, while other studies have placed the critical temperature in the range of 60-70°C[113, 114]. Interestingly,

experiments performed by Berntsen et al.[115] over 160 days at high initial saturation values of ~300 at room temperature in a 1 wt.% NaCl solution at pH 7 showed that it is possible to develop protective crystalline $FeCO_3$ at very low temperatures. This suggests that high pH, high supersaturation and significant time is required to generate protective films at low temperature, but it is indeed possible.

In addition to accelerating the kinetics of $FeCO_3$ precipitation and lowering the solubility in the system[100, 102, 116], temperature also plays a role in influencing the nature, characteristics and morphology of surface films, which in turn, influence the CO_2 corrosion process.[8] Ikeda[117] showed that at lower temperatures (<60°C), the $FeCO_3$ films formed struggle to adhere to the steel surface, offering little protection (although this observation may be pH dependent based on the work of Berntsen et al.[115]). Regardless, above 60°C, the level of protection offered was observed to increase with temperature.

The influence of temperature on the kinetics of $FeCO_3$ formation are covered in more detail in Section 5 as this parameter is integrated into the semi-empirical models derived to quantify the precipitation rate. Suffice to say in this section of the review, the growth rate of $FeCO_3$ determined by all predictive models available in literature suggests a particularly slow growth rate at room temperature, but this rate increases rapidly with temperature. Dugstad[15] provided a series of key cross-section images of carbon steel specimens exposed to supersaturated solutions at different temperatures (provided in Figure 7) to highlight the difference and importance of temperature on growth kinetics and protectiveness. At 40°C and S<40 (Figure 7(a)) a non-protective, porous Fe_3C network was reported to form on the steel surface, as precipitation of $FeCO_3$ was minimal. At 40°C with a bulk S>40 (Figure 7(b)), precipitation rate was low and the corrosion rate of the steel substrate exceeded that of the precipitation rate, resulting in corrosion undermining the precipitation and the layer still offering little protection. The layer was also reported to exhibit low crystallinity and be loosely adherent to the surface. At 80°C and S<10 (Figure 7(c)), precipitation was very fast and a protective layer was formed.

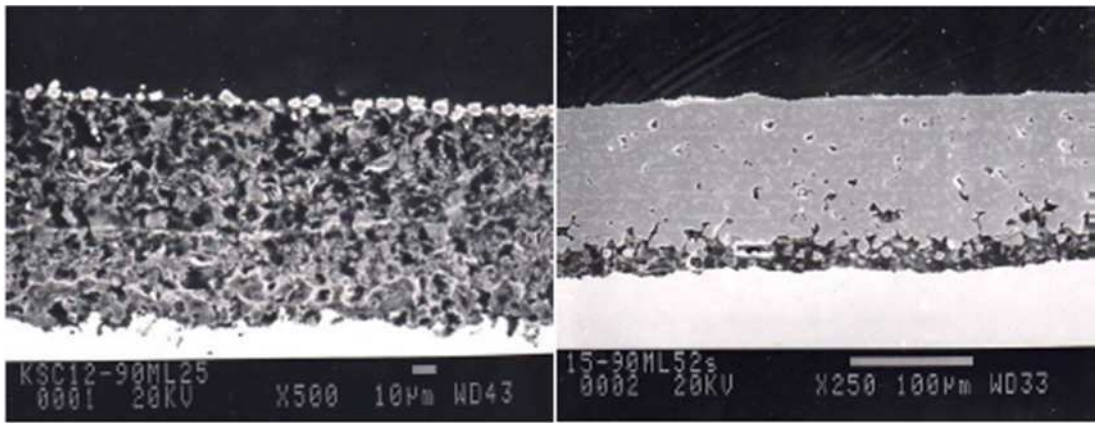

(a) **(b)**

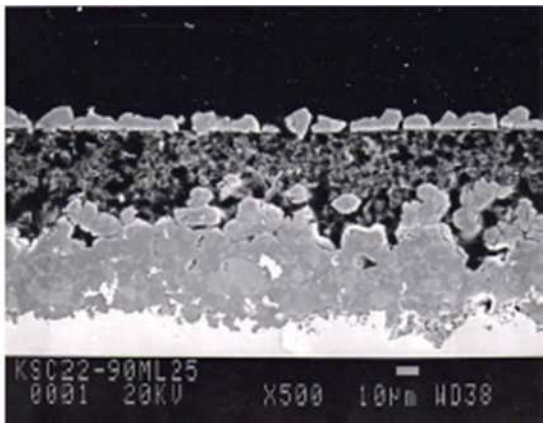

(c)

Figure 7: Cross-sections of samples exposed to various conditions. a) 40 °C and S<40 in bulk solution, b) 40 °C and S > 40 in bulk solution, c) 80 °C and S < 10 in bulk solution – adapted from Dugstad[15] and reproduced with permission from NACE International, Houston, TX. All rights reserved.

4.3.2 CO_2 partial pressure

When conditions do not favour protective $FeCO_3$ formation, the corrosion rate generally increases in conjunction with a rise in CO_2 partial pressure.[116] However, increasing CO_2 partial pressure can promote the precipitation of $FeCO_3$ when its generation is thermodynamically favourable. However, in very specific instances, it can make precipitation less favourable.

At a constant pH level, an increase in CO_2 partial pressure will typically lead to an increase in CO_3^{2-} concentration within the bulk solution and generally, an increase in supersaturation, accelerating the precipitation process (provided pH is high enough to

reach saturation with respect to $FeCO_3$). In terms of the effects of CO_2 partial pressure, the solubility of Fe^{2+} in an NaCl solution as a function of CO_2 partial pressure was determined by Dugstad[15] and is provided in Figure 8. The figure illustrates the complex behaviour of Fe^{2+} solubility as a result of partial pressure changes at constant pH at 60°C. These plots show that as the CO_2 partial pressure is increased, the solubility of Fe^{2+} goes through a maximum value when the system pH is 5 and 5.5. Furthermore, for the lower pH levels of 5 and 5.5, there is a maximum Fe^{2+} solubility as pressure is increased, with an opposite trend seen for pH 6.

The results suggest that an increase in the CO_2 partial pressure of the system can in fact, decrease or increase the potential for $FeCO_3$ films to form indicate that the likelihood of $FeCO_3$ formation cannot be predicted by pH alone.

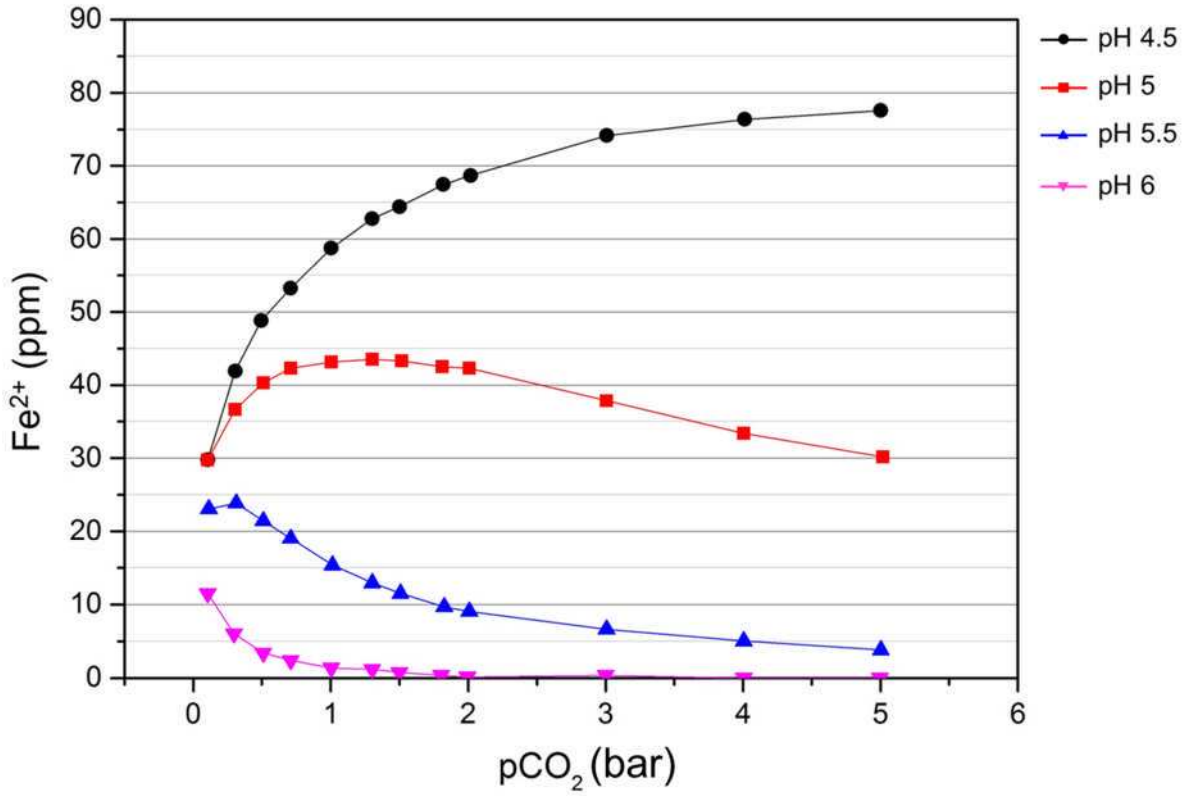

Figure 8: Concentration of Fe^{2+} required to reach $FeCO_3$ saturation, plotted as a function of pCO_2 at pH levels of 4, 5, 5.5 and 6 for a 3.5 wt.% NaCl solution at 60°C – adapted from Dugstad[15] and reproduced with permission from NACE International, Houston, TX. All rights reserved.

A recently developed mechanistic model by Arumugam et al.[118] was employed to study the effect of specific parameters on the nucleation and growth characteristics of $FeCO_3$

scales. The population number and the critical size of the nuclei were determined through the application of classical nucleation theory and the process was based on heterogeneous nucleation and diffusion aided growth of crystals.

From the model, it was possible to extract information on the nucleation rates as a function of the level of $FeCO_3$ saturation, Fe^{2+} concentration and partial pressure of CO_2. The model suggetss that nucleation rates increase with increasing temperature (from 80 to 120°C), resulting in the formation of more protective scales. Interestingly, in terms of the influence of CO_2 partial pressure, it was suggested that nucleation rates would reduce with an increase in this parameter, although an increase in temperature was found to sustain nucleation rates, even at high pressures. Unfortunately, no experimental data was produced to compare against the mechanistic model. Furthermore, the modelling results produced by Dugstad[15] (Figure 8) suggested that the role of partial pressure on solubility is pH dependant, and it was not clear whether the model by Arumugam et al.[118] was conducted for a constant pH solution, or a system where pH evolves with increase in partial pressure and temperature.

In terms of other experimental observations on the role of partial pressure on $FeCO_3$ formation, the general consensus from tests performed at pH 5 or greater is that increasing CO_2 partial pressure accelerates film formation. Videm et al.[119] showed that increasing partial pressure from 1 bar to 10 bar for a 80°C brine at pH 5 resulted in much faster film formation on carbon steel. Furthermore, another study by Gavanluei et al.[120] evaluated the effect of CO_2 partial pressure on the corrosion of carbon steel from room temperature to 75°C. The CO_2 partial pressures applied were 2.8, 5.5, 11, and 22.1 bar, respectively, and corrosion rates were recorded over 24 hours. At temperatures of 50°C and below, no $FeCO_3$ was detected on the steel surface. However, precipitation was evident at 75 °C above partial pressures of 5.52 bar. As partial pressure was increased in this temperature range, the density of $FeCO_3$ crystals increased and the time to produce protective $FeCO_3$ films reduced.

Suhor et al.[121] also performed a study to evaluate the formation of $FeCO_3$ at high partial pressures of CO_2 on carbon steel in comparison to lower partial pressure environments. Experiments were performed at 10 bar and 80 bar CO_2 at both 25°C and 80°C with the pH being allowed to evolve naturally. Only protective film formation was observed at the higher temperature, and despite the higher pressure system producing a lower unbuffered pH, the

kinetics of film formation were faster in this environment. Interestingly, at higher pressure, the $FeCO_3$ layer was able to form more easily at the lower pH, and this was attributed to the higher surface pH due to the initially high rate of material dissolution.

4.3.3 Surface concentration and mass transfer effects

Despite the environmental conditions, the concentration of Fe^{2+} within the bulk solution is undoubtedly one of the most important factors in the film formation process of $FeCO_3$. However, due to the metals susceptibility to corrode, Fe^{2+} is also produced at the steel surface, while H^+ ions are simultaneously being consumed. Diffusive mass transfer between the bulk and steel surface can lead to higher supersaturation at the steel surface, leading to larger rates of precipitation.[15] Hence, accurately predicting the rate of $FeCO_3$ precipitation will require the determination of the surface pH and surface supersaturation.

The corrosion of carbon steel results in a higher pH at the interface and this has been confirmed computationally[122, 123] through numerical simulation, but also experimentally via the use of a mesh capped pH electrode[124]. The high local pH results in an increase in CO_3^{2-} which results in less Fe^{2+} ions being required to exceed the solubility limit of $FeCO_3$. As the surface is corroding, the surface concentration of Fe^{2+} is greater at the surface compared to the bulk solution, resulting in increased supersaturation at the steel surface. Therefore, it is theoretically possible to achieve precipitation at a steel surface in a solution whereby the bulk solution is under-saturated. This concept is discussed further in Section 6 where combined experimental and modelling approaches are considered in their ability to relate local supersaturation to precipitation rate. In Section 6, an example of a numerically determined supersaturation profile from the steel surface into the bulk solution is provided to further illustrate this notion.

In terms of mass-transfer, increasing flow rate will often increase corrosion rate, which obviously leads to a greater flux of Fe^{2+} from the surface[116]. The accentuation of corrosion rate through increased mass transport is particularly evident at low pH (less than pH 5[25]) when the concentration of H^+ is particularly high. Towards higher levels of pH there is little sensitivity in corrosion rate with mass-transfer as a result of the slow hydration process associated with H_2CO_3. Increased mass-transfer will serve to transport Fe^{2+} ions away from the surface. Consequently, although the flux of Fe^{2+} from the carbon

steel surface is increased (increasing $FeCO_3$ surface saturation), the hydrodynamic effects compete against the increased flux in an attempt to lower surface saturation by transporting Fe^{2+} away from the surface more readily.

The bulk of research directed towards understanding the formation of $FeCO_3$ on carbon steel surfaces has been performed in static conditions[54, 87, 88, 90, 97, 98, 107, 108, 111, 125-131] despite a number of researchers highlighting the importance of flow on scale precipitation kinetics, morphology and mechanical properties[112, 122, 123, 132, 133]. In addition, the literature relating precipitation behaviour to the system hydrodynamics appears contradictory in nature. As examples, de Waard et al.[134] reported the formation of protective scales even at very high liquid flow rates whilst Dugstad[79] and Hara et al.[135] reported no $FeCO_3$ formation based on extensive flow loop experiments performed at high flow rates.

In some instances, the apparently divergent results are attributed to the complex nature of the precipitation process and its sensitivity to a number of environmental, as well as physical factors (as discussed in this review). However, the disparity in some circumstances can also be partly attributed to the different experimental methodologies employed, as well as the variation in sample surface area to solution volume used in closed systems, which results in a drift in bulk pH and supersaturation during the experiment due to the corrosion process. Authors then link the occurrence of precipitation in such tests to a set of initial conditions which are not maintained, nor stable throughout the entire experiment. This leads to the wrong conclusions being drawn regarding whether a set of conditions favours $FeCO_3$ precipitation and should not be translated to the 'once-through', constant composition scenario.

In a number of circumstances within the literature, if the reported initial conditions were to be maintained for the entire experiment duration, precipitation would be slower, or not occur at all, resulting in very different conclusions being drawn regarding film formation kinetics and their protective properties. The limitation of closed systems is addressed further in Section 6, along with suggestions of how to effectively maintain a stable solution chemistry (particularly from the perspective of Fe^{2+} concentration and pH).

Relating back to the effects of mass-transfer, the critical relationship between supersaturation and surface precipitation inevitably implies some effect of solution flow

rate on the kinetics of the process. Such effects have been recently explored by Sk et al.[18]. Their analysis of *in situ* synchrotron X-ray diffraction with electrochemical measurements for a rotating disc electrodes revealed the dependency of precipitation kinetics on local supersaturation. They proposed that the formation of crystalline $FeCO_3$ is preceded by the formation of a colloidal precipitate in the solution and an amorphous surface layer, and that the presence and thickness of this thin layer controls the current response from potentiostatic experiments. By varying rotation speed, pH and applied potential, the authors claimed that the only effect of microstructure, surface roughness, electrode potential and flow were to change local supersaturation by changing the current density per unit area flowing through the amorphous layer, and that the variation in brine concentration apparently had no effect.

The analysis and interpretation of the data produced by synchrotron tests needs to be performed carefully when electrochemical techniques are employed that perturb the system significantly away from its equilibrium state. The work of Sk et al.[18], Ko et al.[136-138] and Ingham et al.[93, 139, 140] have utilised *in situ* synchrotron techniques and *in situ* electrochemical measurements to understand the formation of $FeCO_3$ and some of the key variables influencing the morphology and kinetics of formation of the crystalline layer. In all of the techniques, due to the limited time frame for synchrotron analysis, the precipitation kinetics and local supersaturation have been accelerated through the application of a fixed anodic current or anodic potential. In most instances, the initial current densities are around 5 mA/cm^2, which equates to approximately 58 mm/year as a corrosion rate. This current density rises to ~25 mA/cm^2 over the course of the experiment in some instances[136].

In the tests which report the initial formation of an amorphous layer on the steel substrate prior to the development of a crystalline layer[18, 139], such an observation is perhaps not surprising given that the current density response ranged from ~5 mA/cm^2 up to ~15 mA/cm^2 during the early stages of film formation (~58 to 174 mm/year). Such excessive currents result in an exceptionally high surface supersaturation, and given the exponential dependency of nucleation rate on supersaturation, it is possible for this process to occur to the near exclusion of particle growth, resulting in the formation of a colloidal solution at or close to the steel surface[15]. The observed initial amorphous/nano-crystalline layer is consistent with the observations of authors who

have performed tests at high temperatures and/or pressure when the initial dissolution rates at open circuit potential (OCP) are high (resulting in a high level of supersaturation at the steel surface) or when temperature/pH is low (resulting in high supersaturation being sustained in the bulk solution for prolonged periods)[82, 141-143].

However, in systems where the corrosion rates are not excessive (particularly when pH is high), precipitation appears to have been observed without the initial development of such an amorphous layer[54, 82, 144]. Examples of both scenarios are provided in Figure 9 and this factor is typically overlooked as many authors tend not to track the growth of $FeCO_3$ over the duration of experiments or in the early stages of growth. Instead they merely observe the layer at the end of experiments once the corrosion rate has stabilised. Therefore, one needs to be careful when relating such a proposed mechanism to systems where the surface supersaturation is considerably lower and particle growth competes more closely with the nucleation process. The proposed mechanism of the amorphous pre-cursor to the formation is an interesting concept, and could be the appropriate formation mechanism in systems when the samples are highly polarised or the initial supersaturation at the surface is particularly high at OCP for prolonged period of time (i.e. when high nucleation rates supress or exclude crystal growth). However, one should exercise caution with generalising such behaviour to systems where the surface supersaturation and corrosion rates are much lower (which can be encountered in oil and gas systems for hydrocarbon transport) as the corrosion and precipitation kinetics may not be controlled or influenced by the presence of such an amorphous layer.

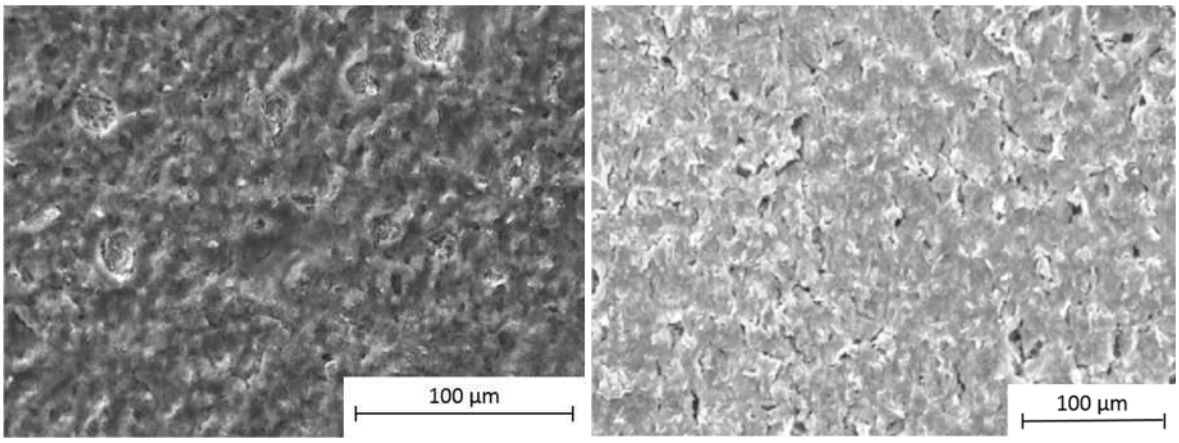

(a) **(b)**

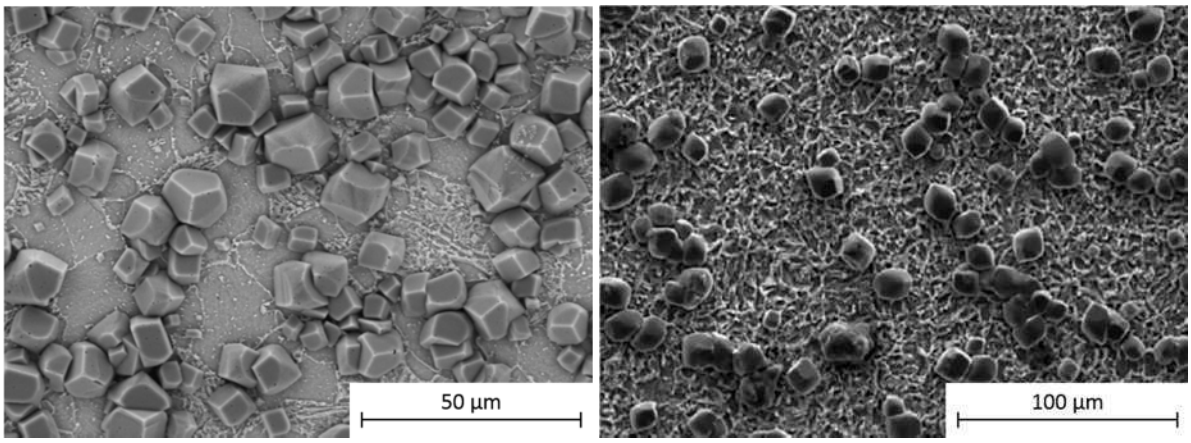

(c) **(d)**

Figure 9: (a)/(b) Examples of experiments where an amorphous/nano poly-crystalline layer develops on the steel surface prior to the formation of crystalline $FeCO_3$; (a) Hua et al.[141] - X65 steel after 24 hours in distilled water at 50 °C and 80 bar pCO_2[141], (b) Wei et al.[142] - X70 steel after 2 hours in 3.5 wt.% NaCl solution at 80°C and 95 bar pCO_2[142] (c)/(d) Examples of experiments were crystals form in the absence of an initial amorphous layer and precipitate directly onto the steel surface; (c) unpublished image from the authors own work - X65 (initially polished with diamond suspension) after 8 hours in CO_2-saturated 3.5 wt.% NaCl solution at 80°C, pH 6.8 at room pressure – the ferritic-pearlitic microstructure can be observed on the surface as a result of the initial dissolution from the surface, (d) Pessu et al.[82] - X65 after 36 hours in CO_2-saturated 3.5 wt.% NaCl solution at 50°C, initial pH of 6.6 at room pressure – the image shows precipitation of $FeCO_3$ onto an iron carbide (Fe_3C) network (reproduced with permission from NACE International, Houston, TX. All rights reserved.).

4.4 Effect of steel and interface properties on precipitation

4.4.1 Steel microstructure

The microstructure associated with carbon steels plays an important role on the corrosion behaviour and protectiveness of the formed corrosion products, as shown in a number of studies[78, 131, 145-150]. In particular, the size and protectiveness of Fe_3C within the steel structure has been suggested to determine the protectiveness of the layer formed[131, 148], with conflicting observations on its role having been suggested[8, 78, 145, 151, 152]. However, the majority of investigations indicate that ferritic-pearlitic

microstructures exhibit better corrosion resistance when compared with martensitic or martensitic-bainitic steels in the absence of protective films[78, 146, 147, 149]. This has been attributed to the distinct layering between ferrite and Fe_3C within the pearlite phase[136, 145, 153].

In relation to the role of microstructure on $FeCO_3$ formation and protectiveness, Palacios and Shadley[146] discussed how this may influence the structure of $FeCO_3$. They claimed that $FeCO_3$ is less tenacious and less crystalline on martensitic steels compared to ferritic-pearlitic steels. Such observations were supported by Ueda and Takabe[78] who evaluated J55 steel (ferritic-pearlitic) against N80 steel (martensitic) in a CO_2 environment with 3 bar CO_2 and 80°C. They stated that as J55 corroded, the lamellar Fe_3C was left behind, resulting in an increase in the local concentration of Fe^{2+} in the cavities, promoting $FeCO_3$ formation. However, the opposite behaviour was witnessed by Dugstad et al.[154], who found that ferritic-pearlitic steels did not encourage $FeCO_3$ formation, and corrosion product growth was more favourable on martensitic steels. Ueda and Takabe[78] suggested that the Fe_3C then helps to anchor the corrosion product to the steel surface. In the N80 steel, the homogeneous dispersed Fe_3C allows the corrosion product to peel off partially because it does not possess the anchoring effect of J55. Therefore, N80 suffered from severe localised corrosion whilst J55 did not. The anchoring effect promoted by pearlite regions has also been reported by a number of other authors[78, 145, 146], however, some studies have suggested that the needle-like carbide structure produced by martensitic steels provides better anchoring of corrosion products compared to large ferritic areas with small pearlite grains[148]. In addition, Dugstad et al.[154] reported higher corrosion rates of ferritic-pearlitic steels compared with martensitic steels, stating that no protective film formed on ferritic-pearlitic microstructures of St52 steel. Some researchers have also proposed that in some instances, an extensive carbide layer can accentuate corrosion through galvanic effects and internal acidification[8, 151, 152], preventing the precipitation of $FeCO_3$. In a more recent study, Ko et al.[136] compared the effects of modifying microstructure and chromium micro-alloying on the formation of $FeCO_3$ using a potentiostatic approach combined with *in situ* synchrotron measurements. Experiments at pH 6.8 and 80°C in a 0.5M NaCl CO_2-saturated solution at room pressure revealed that, on average, the effect of micro-alloying (discussed in the following paragraphs in more detail) dominates the $FeCO_3$ nucleation and growth behaviour compared to microstructure, with little difference in current transients being observed

between ferritic-pearlitic and martensitic microstructures of a 1% Cr/0.25% Mo low alloy steel.

As stated previously, the development of a porous Fe_3C layer is able to act as a diffusion barrier, preventing the diffusion of Fe^{2+} ions away from the surface, promoting the formation of $FeCO_3$ within the network, which can ultimately lower corrosion rate.[8, 151, 155] An example of an Fe_3C network encouraging the growth of $FeCO_3$ is shown in Figure 10 which is adapted from the paper by Farelas et al.[155]. In this study, two steels with similar carbon content and different microstructure (X65 with martensitic and UNS G10180 with ferritic-pearlitic) were exposed to a 3 wt.% NaCl solution saturated with CO_2 at 80°C and pH 6. Over time, a porous Fe_3C layer was observed on both steels which exhibited different morphologies due to the different microstructures. As the test progressed, the Fe_3C layer acted as a diffusion barrier resulting in a high local pH inside the network, facilitating the precipitation of $FeCO_3$. Ieamsupapong et al.[156] reported similar results in a more recent study in which Fe_3C was found to influence the formation of $FeCO_3$ by acting as a diffusion barrier. These tests were performed on a ferritic-pearlitic steel over a pH range of 5.4 to 6. Based on these observations, the presence of such a porous network appears to be a prerequisite, along with supersaturation in some instances.

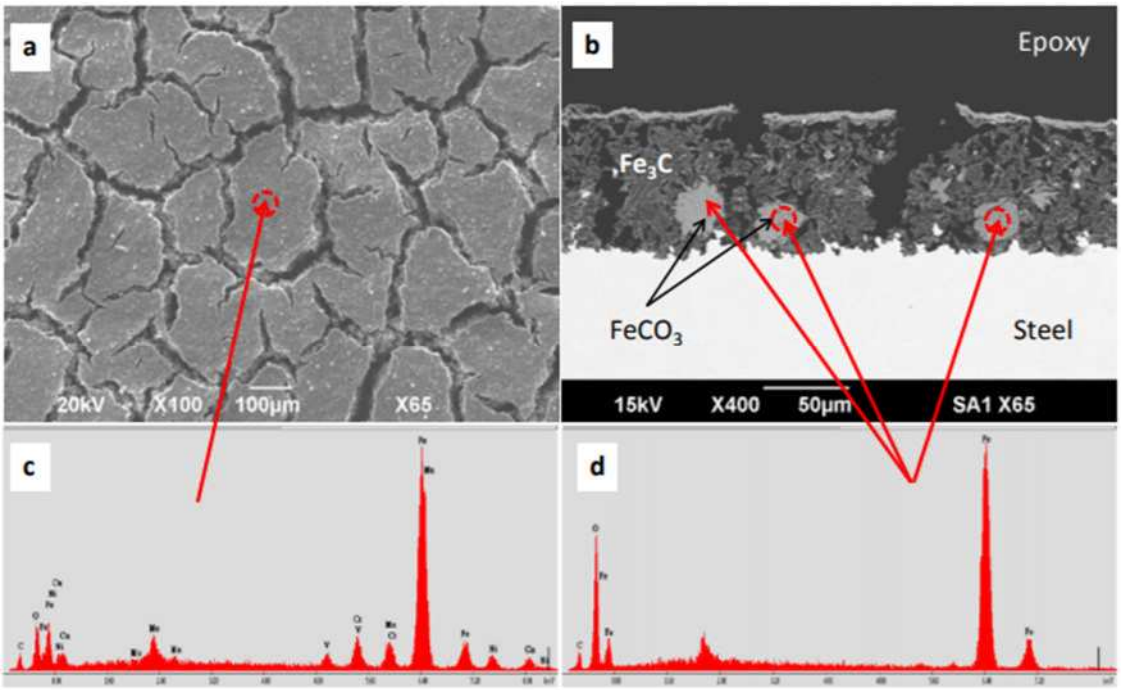

Figure 10: SEM and EDX analysis of X65 steel after exposure to 3 wt.% NaCl solution at 80°C at 0.5 m/s and pH 6 for 41 h; (a) top view and (b) cross-section with the associated EDX analysis in (c) and (d) – image adapted from Farelas et al.[155] and reproduced with permission from NACE International, Houston, TX. All rights reserved.

4.4.2 Micro-alloying

The influence of composition of low alloy steels on CO_2 corrosion behaviour has been explored and reviewed considerably over the past few years[78, 117, 145, 147, 149, 150, 157-167] The purpose of this section of the paper is to focus more towards the role of such alloying elements on the formation of protective films, not on the corrosion characteristics of the steel in non-scaling conditions. However, the general consensus in the absence of protective films is that chromium (Cr) addition has the most significant effect on reducing corrosion rate. As well as varying Cr content, studies have also focused on the influence of micro-alloying elements such as vanadium (V), titanium (Ti), niobium (Nb), molybdenum (Mo), copper (Cu) and silicon (Si)[8, 154], with the purpose of preventing Cr from being tied up within carbides of low Cr containing steels, affording it the opportunity to participate in the formation of chromium oxide which enriches corrosion product films. Such effects can also be achieved through the reduction in carbon content of the steel[6, 150, 160]. A summary of the effects of alloying elements (as well as steel microstructures) on CO_2 corrosion performance in the absence of corrosion products is provided by Kermani[8], where one of the main aspects emphasised was the importance of the ratio between alloying elements and carbon content, as this relates to the level of carbide removal. Kermani[8] also made reference to effects of Mo addition as well as Cr. Therefore, the focus of this section of the review paper is orientated towards these two specific elements, as they appear to hold the most promise.

Although micro-alloying of Cr is undoubtedly the most effective in improving the CO_2 corrosion resistance of carbon steels[8, 56, 164-166, 168-175], a number of studies have also considered the role of Mo concentrations of 0.15-0.25 wt.%, typically in combination with 0.5-3wt.% Cr[146, 162, 168, 169, 176]. These combinations have demonstrated a significant improvement in corrosion resistance, but also appear to facilitate the formation of a less porous, better adhered and more protective corrosion product. Interestingly, Ingham et al.[139] and Ko et al.[137] identified that the addition of Cr^{3+} to a brine solution at 80°C and

pH 6.8 reduced the critical supersaturation and enhanced the crystallisation rate of $FeCO_3$ on carbon steel. The study by Ko et al.[137] also revealed the ability of molybdate ions to promote the growth of $FeCO_3$ under the same operating conditions. Studies on low Cr alloys have shown that the development of an amorphous layer consisting of chromium hydroxide ($Cr(OH)_3$) and $FeCO_3$ can significantly reduce the corrosion rate[56, 173, 177-179].

With regards to the addition of Mo to carbon steels, the influence of this particular alloying element on $FeCO_3$ formation has not been well addressed and the individual effect of Mo addition is unclear. Although the addition of Mo to steels in the presence of Cr has been reported to have beneficial effects on corrosion rate in the absence[176] and presence[150, 162, 176] of corrosion products, a mechanistic interpretation of why corrosion rates are lower, or why corrosion products are more protective is not provided. Research evaluating the effect of Cr and Mo as alloying elements typically remarks on the overall improvement in corrosion rate reduction or scale formation, without showing the decoupled effect of each element or the interactions between Cr and Mo. However, a more recent study by Sk et al.[168] focused on systematically varying both the Cr and Mo content from 0-3.5 wt.% and 0-0.7 wt.%, respectively, with the goal of determining the role of each element on the corrosion rate and corrosion product protectiveness. Experiments were conducted on each steel within a CO_2-saturated 0.5 mol/L NaCl brine at 80°C and pH 6.6 in hydrodynamic conditions using a rotating disc electrode (100 or 1000 rpm). The results from potentiostatic current transients revealed that a synergistic interaction exists between Cr and Mo, which induces more rapid crystallisation of $FeCO_3$ compared to steels with an absence of Mo. Furthermore, increasing Mo content resulted in the formation of a thinner, but more compact film. The authors proposed that the addition of small amounts of Cr/Mo modulates the current due to dissolution as well as the current due to growth of the crystalline layer. They also claimed that the Cr/Mo species emitted into the solution at the metal interface significantly accelerate the electro-crystallization of $FeCO_3$.

4.4.3 Corrosion rate vs precipitation rate

In addition to the rate of $FeCO_3$ accumulation on the steel surface, the corrosion rate of the underlying steel is also an important consideration, as this effectively has the potential to 'undermine' the film. As voids are created beneath the film as a result of the steel dissolution process, they are filled by ongoing precipitation which influences both

the morphology and the ultimate protective capability of the layer.[11] If the precipitation rate significantly exceeds that of the corrosion rate, then a dense, adherent, protective layer is anticipated which can be very thin (<10 μm). Conversely, if the corrosion rate exceeds the rate of $FeCO_3$ formation, a porous and poorly protective film is likely to develop, which can be particularly thick (~100 μm or greater).[11] Research has indicated that the thickness of the $FeCO_3$ layer does not necessarily correlate to a protective film. The key indicators of protectiveness is the layer density, but most importantly, the degree and quality of adhesion between the crystals and the substrate.[11, 14, 125]

In the context of determining if protective film formation will occur, the non-dimensional parameter of scaling tendency is typically used[83, 116]:

$$ST = \frac{PR_{FeCO_3}}{CR} \tag{32}$$

The scaling tendency is the ratio of precipitation (PR_{FeCO_3}) to corrosion rate (CR) in the same units. If ST<<1, a porous and unprotective film is likely to form. When ST>1, conditions are regarded as favourable for the formation of protective $FeCO_3$ films.

4.4.4 Surface roughness

To fully understand and generate reliable precipitation models, it is important to be able to relate the concentration of species at the metal-electrolyte interface to the precipitation kinetics. Achieving this requires an understanding of the mass-transfer characteristics in the system, as this influences the movement of species to and from the steel surface. The roughness of the substrate plays a role in influencing mass-transfer at the surface, but as discussed in the following paragraphs, it can also affect the nucleation stage.

4.4.4.1 Role of mass-transfer

The generation of surface roughness of a material through either wet-grinding (sample preparation), erosion, corrosion, deposition or other processes has the ability to modify the hydrodynamic and mass-transfer boundary layers, resulting in a change in mass-transfer characteristics.[180]

The general agreement within literature examining surface roughness effects on mass-transfer is that rougher surfaces promote increased levels of mass-transfer[181]. In the

context of oil and gas pipelines, Fogg and Morse[182] stated that the surface roughness of steel pipelines delivered to coating yards has a roughness in the order of 20 μm and may even exceed 50 μm. Dawson and Trass[183] proposed that when the surface roughness is large enough to emerge from the viscous sublayer, this enables sufficient turbulence to be generated to disrupt the viscous sublayer, penetrate into the valleys between roughness elements and cause increased mass-transfer across the concentration boundary layer. However, more recent studies have shown that under certain flow conditions, even when the roughness elements are well immersed within the viscous sublayer, the disruption to solely the thinner mass-transfer boundary layer leads to enhancement of mass transfer[181].

The main approach towards characterising mass-transfer behaviour for a system is to determine the mass-transfer coefficient (k) and convert it into the Sherwood number (Sh). By plotting Sh against Reynolds number (Re) it is possible to compare with existing correlations for complete mass-transfer control[181]. Though it is known that roughness will influence the Sh vs Re correlations, defining such effects quantitatively is made challenging due to the diverse geometrical forms of roughness i.e. the mass-transfer characteristics can be changed by the nature of the roughness, specifically the number of roughness elements per unit area, their shape, height, distribution, orientation/alignment to the flow direction[184]. Considerations of such effects are beyond the scope of this review, but important to note.

4.4.4.2 Role of nucleation

From the previous section, the perspective may be that increasing surface roughness in a flowing environment may hinder $FeCO_3$ formation by promoting increased mass-transfer and reducing surface supersaturation (as discussed previously). However, the process of heterogeneous nucleation can also be influenced by roughness, which provides sites with lower surface energy for nucleation[185]. Arumugam et al.[118] showed that nucleation takes place only when the nuclei overcome a free energy/nucleation barrier, ΔG^*, and a critical size is reached. In fact, de Yoreo and Vekilov[185] stated that this barrier determines the kinetics of nucleation, with the nucleation probability being proportional to the exponential of the barrier height divided by the product of the Boltzmann constant and temperature (k_BT)[185]. Therefore, the nucleation rate (J_n) can be expressed as:

$$J_n = Ae^{-\frac{\Delta G^*}{k_B T}} \quad (33)$$

where A depends on many parameters. De Yoreo and Vekilov[185] showed that, amongst other factors (grouped together in Equation (34) as the coefficient 'B' – which incorporates the Boltzmann constant and temperature), the nucleation rate depends strongly on the supersaturation (S) and interfacial energy (α). These values are second and third power terms, respectively, in the argument of an exponential, indicating that they are critical in terms of influencing nucleation rate.

$$J_n = Ae^{-\frac{B\alpha^3}{S^2}} \quad (34)$$

The surface roughness is strongly linked to surface energy. Therefore, it is sensible to suggest that the initial roughness of a steel surface, or the evolution of roughness during corrosion can have a significant effect on $FeCO_3$ formation, yet this has not been considered in the literature with respect to $FeCO_3$ precipitation. Certainly, from our own studies, surface roughness appears critical in influencing crystal nucleation. Figure 11 provides a comparison of X65 steel exposed to a CO_2-saturated 3.5 wt.% NaCl solution for 3 hours in static conditions. One sample was polished with 3 μm diamond suspension prior to immersion in the test solution, while the other was wet-ground using 120 grit SiC paper. There is clearly a difference in nucleation rate and growth of crystals under these conditions.

The results in Figure 11 are supported by the work of Ko et al.[136] who evaluated the kinetics of $FeCO_3$ nucleation and growth on mild steel with surface finishes of 1 μm and 46 μm in a 0.5 mol/L NaCl solution saturated with CO_2 at room pressure, 80°C and pH 6.8. They reported that the effect of surface finish was dramatic. Under potentiostatic polarisation, the rougher surface exhibited an increase in current density immediately upon application of potential where as an induction time was observed before current increased for the smoother sample. The increase in roughness also altered the nucleation and growth kinetics, with the rough sample inducing nucleation much earlier, and promoting faster growth.

Such effects of surface roughness on the precipitation of $FeCO_3$ have perhaps not received the attention they warrant. However, the authors believe that a number of apparent inconsistencies across literature for reported precipitation rates of $FeCO_3$ onto the same substrates can be attributed to the difference in sample preparation or the initial surface

condition. There is clearly a counter-balance effect from increased roughness between its influence on lowering local supersaturation (due to enhancement of mass-transfer) and increasing nucleation kinetics (through lowering interfacial energy and promoting increased supersaturation within the grinding grooves as a result of the preparation process). Depending on which effect dominates dictates the role of roughness on the nucleation and growth processes.

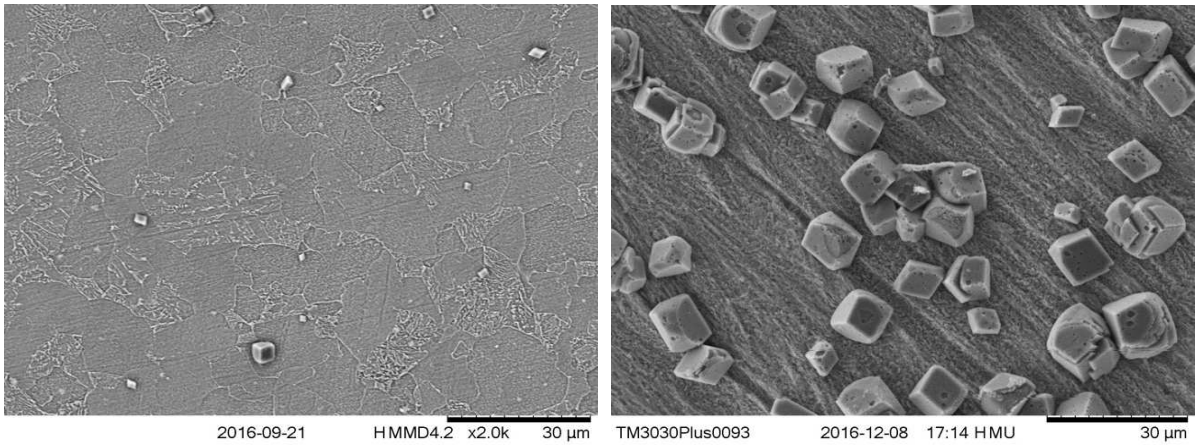

Figure 11: SEM images of X65 steel after exposure to 3.5 wt.% NaCl solution at 80°C and pH 6.8 for 3 h; (a) initial surface finish achieved by polishing with diamond suspension (b) initial surface finish achieved by wet-grinding with 120 grit SiC paper.

5. Developed models for $FeCO_3$ precipitation

5.1 Summaries of $FeCO_3$ precipitation models

The growth of $FeCO_3$ crystals is determined by the kinetics of the precipitation reaction. The process is governed by the heterogeneous crystallisation from the aqueous solution and such a process can be divided into two phases which both possess distinct kinetics, nucleation and growth.[54]

Research has shown that nucleation is predominantly important in homogenous crystallisation processes, while in the case of precipitation reactions (heterogeneous crystallisation) the process is believed to be dominated by crystal growth.[54] However, though this may be true for cases in which the solution is highly super-saturated with $FeCO_3$ (where induction times are rapid), this process could be different in a scenario

whereby the level of saturation is very low at the steel surface and the induction time is prolonged, as may be the case in certain oil and gas operating scenarios.

For engineering applications, four semi-empirical growth rate expressions have been developed to determine the rate of *precipitation* of crystals *(PR)*. These take the following form:

$$PR = k_r \frac{A}{V} \sigma(S) \qquad (35)$$

where k_r is the kinetic constant, A/V is the ratio of surface area (of seed crystals or the steel sample) to solution volume, σ is termed as the driving force of the precipitation process which, for $FeCO_3$ crystal growth, is a function of the saturation ratio *(S)* (as described earlier using Equation (12)).

These four models have been developed by Greenberg and Tomson[60, 61], Johnson and Tomson[59, 76], van Hunnik et al.[83] and Sun and Nesic[54, 77, 186]. A full summary of each of the models, the different experimental approaches adopted to generate expressions and the exact equations derived is provided in Table 5.

To summarise how each model was generated, the methods employed by both Greenberg and Tomson[60, 61] and Johnson and Tomson[59, 76] involve estimating precipitation rate in a bulk solution by measuring the change in Fe^{2+} concentration. The systems considered by both sets of authors consisted of low saturation ratio solutions where the growth was measured on well characterised *seed crystals in a bulk solution*.

The method of van Hunnik et al.[83] also involved measurement of Fe^{2+} concentration, but this was performed by determining the initial deviation of Fe^{2+} concentration increase once the system passed through the pH at which the solubility of $FeCO_3$ was exceeded. The work focused on extending the validity of the Johnson and Tomson model to higher saturation ratios of ~1000 as they believed that this initial model overestimated precipitation rate at this level. In tests performed by van Hunnik et al.[83] the substrate was a steel pipe surface, however, the implementation of the Fe^{2+} concentration measurements implicitly assumes that the entire amount of Fe^{2+} lost in the solution is associated with $FeCO_3$ deposition onto the steel surface. It must be noted that $FeCO_3$ not only deposits onto the steel surface, but elsewhere in the system. Consequently, the model of van Hunnik et al.[83] will evidently lead to an over-estimation of $FeCO_3$

precipitation rate onto a steel surface, particularly at high saturation levels when significant bulk precipitation occurs.

The experimental technique implemented by Sun and Nesic involved the direct measurement of $FeCO_3$ precipitation onto a corroding steel surface by determining the mass gain of a $FeCO_3$ covered sample. Steel samples were placed in a deoxygenated saline solution and ferrous chloride was added to create a specific level of $FeCO_3$ saturation. Samples were then removed at regular intervals from the system, dried and weighed. The corrosion product layer was then removed using Clarke's solution before being weighed again. The difference in mass and time of exposure were then used to determine precipitation rates (or corrosion layer accumulation rate (CLAR), as will be discussed below).

5.2 Comparison of the kinetic constant, solubility product and driving force

Figure 12 provides a comparison of each of the four models in terms of their proposed kinetic constant as a function of temperature, the driving force as a function of supersaturation, and the solubility constant implemented as a function of temperature. These terms are shown in Table 5. In the case of the van Hunnik et al.[83] model, the solubility product equation was not provided in the paper itself, so it is omitted from the figure. The values of each term across the four equations all agree to within one order of magnitude of one another, with the exception of the Sun and Nesic model, where there is a significant discrepancy in relation to the proposed kinetic constant. This results in drastically lower precipitation rates being predicted from this model in comparison to the other three (reasons behind this difference in kinetic constants and precipitation rate prediction will be discussed in due course).

Regardless of the difference in value, the role of temperature and the observed trends remain the same i.e. increasing temperature serves to increase the kinetic constant and reduce the solubility product. This reduction in solubility product causes an increase in supersaturation for given Fe^{2+} and CO_3^{2-} ion concentrations/activities, which serves to increase the driving force, promoting an overall increase in precipitation rate with temperature.

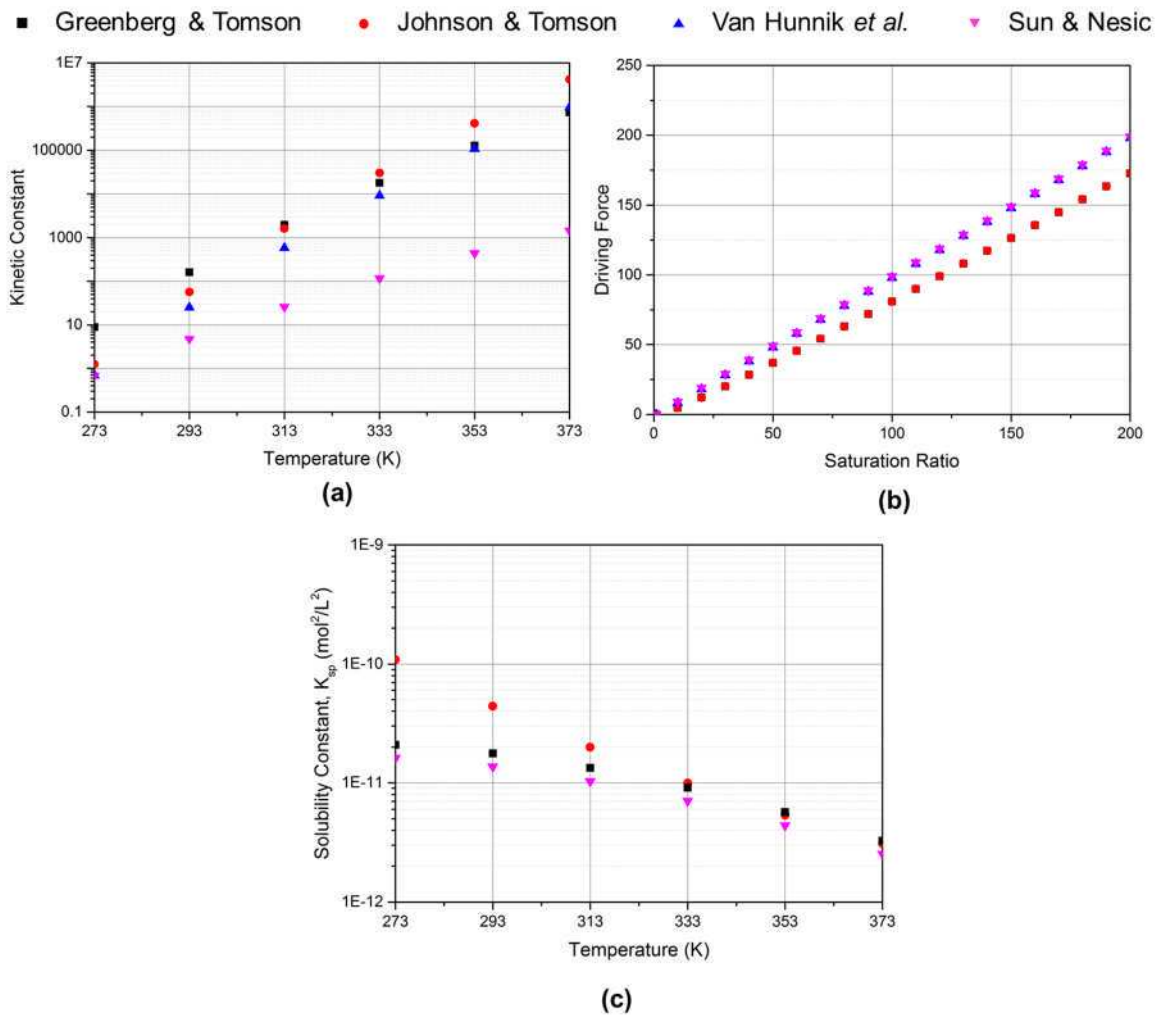

Figure 12: Kinetic constant as a function of temperature, driving force as a function of $FeCO_3$ saturation and solubility constant as a function of temperature from the Greenberg and Tomson model, the Johnson and Tomson model, the van Hunnik, Pots and Hendriksen model and the Sun and Nesic model. Note that the Johnson and Tomson and Greenberg and Tomson models use the same driving force expression, and that the solubility equation for the van Hunnik et al. model was not provided in the paper itself, so is omitted.

5.3 Discussion of A/V ratio

The A/V ratios defined by Greenberg and Tomson[60, 61] and Johnson and Tomson[59, 76] in their expressions relate to the area of crystals relative to the solution which they are suspended in. How this translates to the case of a corroding steel surface is unclear. Sun and Nesic[54] used the initial projected area of the steel surface to determine the precipitation rate in their studies. However, for longer term studies where a porous

$FeCO_3$ film develops, the A/V ratio in a closed system will inevitably change with time, and how this translates to an open system such as a steel pipeline is not clear. This concept was discussed by Nesic et al.[116] during the development of a numerical model to describe the kinetics and evolution of film porosity of $FeCO_3$. They considered the A/V ratio from the perspective of that encountered within a porous film. From a review of the precipitation models and using a simple asymptotic analysis, they deduced that in the absence of a film (i.e. in the bulk solution), porosity (ε) is 1 and A/V=0. This implies there is no precipitation in the bulk, no matter how high the saturation or temperature. In contrast, for a 100% dense film, ε=0 and A/V=0. Between these values, the A/V values can become particularly large. Nesic et al.[116] also stated that some information exists within literature on how A/V changes with porosity, but these simple geometric models typically fail at one of the extremes. Based on a thorough analysis and comparison with CO_2 corrosion experiments, the A/V ratio was expressed as a function of porosity in the following form:

$$\frac{A}{V} \propto \frac{\varepsilon^2(1-\varepsilon)}{\Delta x} \tag{36}$$

where Δx is the width of the control volume.

nucleation and that the precipitation process is controlled by the crystal growth rate. A one-dimensional control volume approach is used and the proposed equation for the film growth kinetics is based on a mass balance for solid $FeCO_3$:

$$\frac{\partial c_{FeCO_{3(s)}}}{\partial t} = PR_{FeCO_{3(s)}} - CR\frac{\partial c_{FeCO_{3(s)}}}{\partial x} \tag{37}$$

where $\frac{\partial c_{FeCO_{3(s)}}}{\partial t}$ is the rate of change of $FeCO_3$ concentration, $PR_{FeCO_{3(s)}}$ is the precipitation rate and $CR\frac{\partial c_{FeCO_{3(s)}}}{\partial x}$ is the undermining rate of the film due to corrosion.

Equation (37) was then rearranged to form an expression in terms of porosity to provide information on the film morphology:

$$\frac{\partial \varepsilon}{\partial t} = -\frac{M_{FeCO_{3(s)}}}{\rho_{FeCO_{3(s)}}} PR_{FeCO_{3(s)}} - CR\frac{\partial \varepsilon}{\partial x} \tag{38}$$

where $M_{FeCO_{3(s)}}$ is the molecular mass and $\rho_{FeCO_{3(s)}}$ is the density of $FeCO_3$.

5.4 Comparison and evaluation of precipitation models and their applicability to corroding steel surfaces: the concept of corrosion layer accumulation rate (CLAR)

As previously mentioned, four main models exist in literature for predicting $FeCO_3$ precipitation and all models take the form of Equation (35). Figures 13(a) to (d) show the precipitation rates predicted by all four models over the same range of saturation ratios and temperatures. For each precipitation rate model, the corresponding K_{sp} model has been used, along with an A/V ratio of 1 m^{-1} and an ionic strength of zero. This is true for all models, with the exception of the van Hunnik et al.[83] model. Given that the K_{sp} values were not referred to explicitly in the publication, the most recent Sun and Nesic K_{sp} model was implemented.

All models demonstrate increasing precipitation rate in conjunction with temperature and saturation ratio (as expected), and there is generally a strong agreement between the Greenberg and Tomson, Johnson and Tomson and van Hunnik et al. models. However, the model proposed by Sun and Nesic differs by over three orders of magnitude in some instances.

Table 5: A summary and comparison of the four available $FeCO_3$ precipitation models available in literature

	Greenberg and Tomson	Johnson and Tomson	Van Hunnik, Pots and Hendriksen	Sun and Nesic
Summary	Crystals were pre-grown in an anoxic environment and washed to remove counter-ions. Consequently, well characterised seed crystals were used as a substrate. Precipitation kinetics were determined by using the traditional (indirect) technique which involves measuring Fe^{2+} concentration change. Precipitation was initiated by raising pH by lowering the CO_2 partial pressure in the system.	Crystals were pre-grown in an anoxic environment and washed to remove counter-ions. Consequently, well characterised seed crystals were used as a substrate. Precipitation kinetics were determined by using the traditional (indirect) technique which involves measuring Fe^{2+} concentration change. Equilibrium was established over 48 hours, then temperature was ramped, with samples being removed from the reaction vessel every 30 mins.	Experiments were performed in a flow loop under anoxic conditions. Precipitation kinetics were determined by using the traditional (indirect) technique which involves measuring Fe^{2+} concentration change. The rate was determined from the initial deviation from the linear increase of the Fe^{2+} concentration after the saturation point was exceeded.	Experiments were performed in a glass cell. Steel samples were placed in a deoxygenated saline solution. Ferrous chloride was added to create a specific level of $FeCO_3$ saturation. Samples were removed at regular intervals. Precipitation rate was determined by measuring the mass difference with and without the $FeCO_3$ layer.
Substrate	$FeCO_3$ seed crystals	$FeCO_3$ seed crystals	Steel pipe surface	Steel coupons
Solution	Deoxygenated water	Deoxygenated water	Deoxygenated 1 wt.% NaCl solution	Deoxygenated 1 wt.% NaCl solution
Precipitation rate (P_{FeCO_3}) (mol/m³/s)	$e^{A_0-\frac{E}{RT}}\frac{A}{V}K_{sp}\left[\sqrt{S}-1\right]^2$	$e^{A_0-\frac{E}{RT}}\frac{A}{V}K_{sp}\left[\sqrt{S}-1\right]^2$	$e^{A_0-\frac{E}{RT}}\frac{A}{V}K_{sp}(S-1)\left(1-\frac{1}{S}\right)$	$e^{A_0-\frac{E}{RT}}\frac{A}{V}K_{sp}(S-1)$
Solubility product, K_{sp} (mol²/L²)	$log(K_{sp}) = -59.2385 - 0.041377(T_K) - \frac{2.1963}{T_K} + 24.5724log(T_K)$	$log(K_{sp}) = -0.4343\left(\frac{-30140}{8.314(T_K)} + 36.22\right)$	No K_{sp} value identified	$log(K_{sp}) = -59.3498 - 0.041377(T_K) - \frac{2.1963}{T_K} + 24.5724log(T_K) + 2.518(I^{0.5}) - 0.657(I)$
Constant, A_0	44.4	56.3	52.4	28.2
Activation Energy, E (kJ/mol)	95.8	127.3	119.8	64.9
Area, A	Area of crystals surfaces	Area of crystal surfaces	It is not clear from the paper whether the area used was determined from crystal size or from the area of the corroding electrode	Area refers to that of the corroding sample
Volume, V	Volume of solution	Volume of solution	Volume of solution	Volume of solution

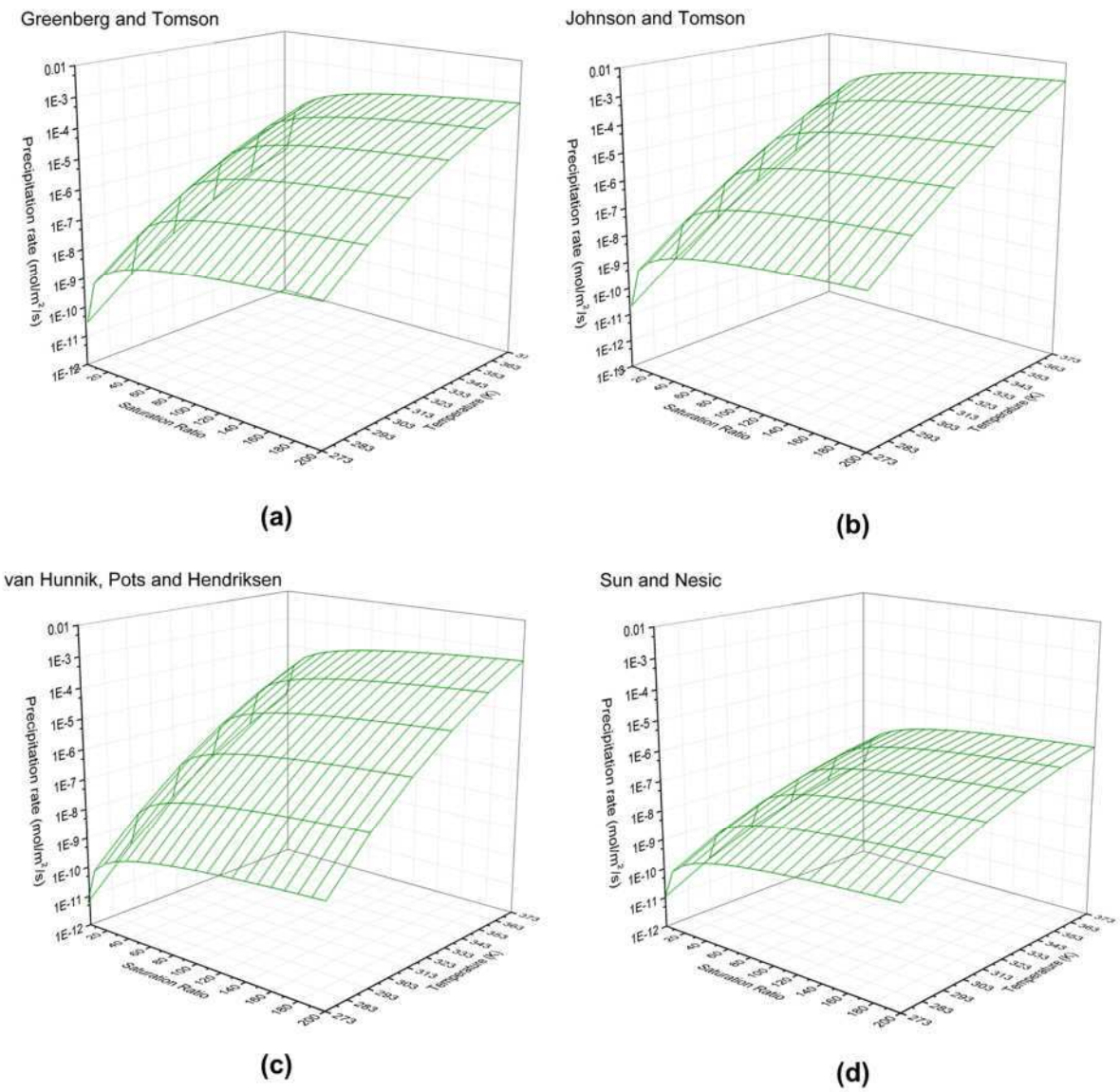

Figure 13: Predicted precipitation rates for $FeCO_3$ for saturation ratios from 0 to 200 and temperature from 0 to 100°C for (a) the Greenberg and Tomson model, (b) the Johnson and Tomson model, (c) the van Hunnik, Pots and Hendriksen model and (d) the Sun and Nesic model. Note that the corresponding K_{sp} models have been used for each precipitation model, with the exception of the van Hunnik et al. model where the K_{sp} model of Sun and Nesic is applied.

The reason behind such a significant discrepancy cannot be solely attributed to the different K_{sp} predictions which feed into the precipitation models. This is reflected in Figures 14(a) and (b) which shows the predicted precipitation rates for all four models when the K_{sp} values of Sun and Nesic are implemented over the temperature range of 0 to 100°C for saturation ratios of 10 and 200.

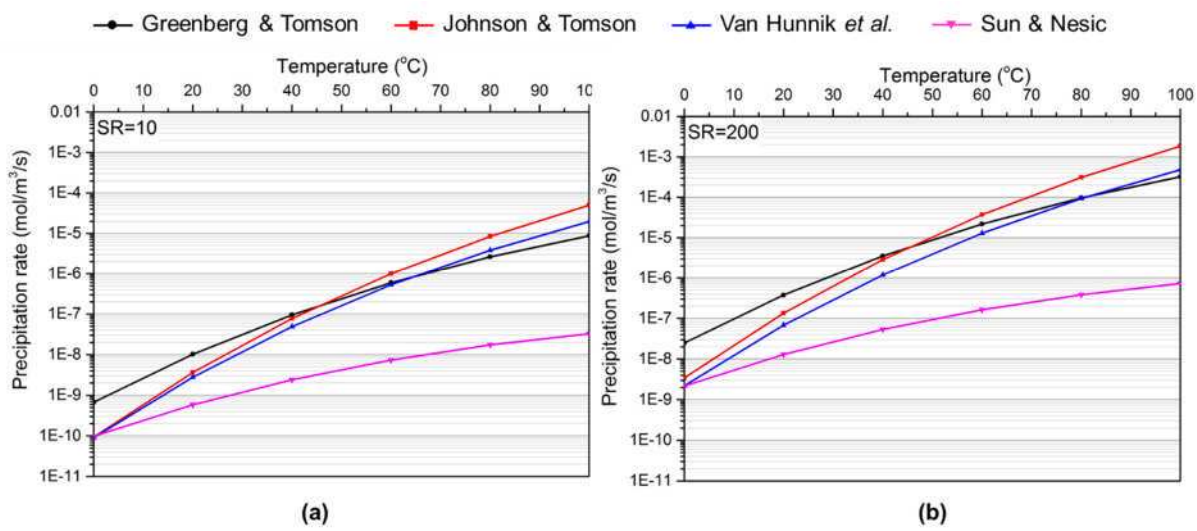

Figure 14: Predicted precipitation rates for $FeCO_3$ for four models when *the same K_{sp} model* of Sun and Nesic is used in all four equations. Precipitation rates are calculated over a range of temperature form 0 to 100°C at saturation ratios of (a) 10 and (b) 200.

As stated previously, the Greenberg and Tomson model, as well as the Johnson and Tomson model are both determined by evaluating the growth of $FeCO_3$ onto well characterised seed crystals. These precipitation models essentially characterise the growth of $FeCO_3$ in a bulk solution from seed crystals and do not necessarily relate the growth kinetics onto a steel surface. Consequently, the precipitation rates produced by these models are in the units of $mol \cdot m^{-3}s^{-1}$ if the A/V ratio is considered. It is important to stress here that neither Greenberg and Tomson, nor Johnson and Tomson explicitly state in their publications that their kinetic expressions can or should be applied to a corroding steel surface in a CO_2 environment.

In the case of van Hunnik et al.[83] this expression can be used to determine a rate of corrosion product accumulation onto a corroding steel surface. Again, as the equation stands in Table 5, this precipitation rate is expressed in $mol \cdot m^{-3}s^{-1}$. However, Gulbrandsen[129] indicated that the van Hunnik model can be rearranged to produce a precipitation rate per unit area ($mol \cdot m^{-2}s^{-1}$) (or a CLAR):

$$\frac{V}{A} P_{FeCO_3} = e^{A_0 - \frac{E}{RT}} K_{sp} (S-1)\left(1 - \frac{1}{S}\right) = CLAR \qquad (39)$$

Nonetheless, this expression still assumes that all precipitated $FeCO_3$ in the system ends upon the steel surface, a notion which is known to be untrue. This is also likely to be one of the main reasons why the van Hunnik model follows the behaviour of Greenberg and Tomson and Johnson and Tomson expressions more closely than that of Sun and Nesic.

These observations therefore highlight that a distinction needs to be made between the precipitation rate (i.e. total formation of $FeCO_3$) and the deposition rate (i.e. relating to the quantity of $FeCO_3$ on a steel surface), as will be discussed. This concept was recently addressed by Sun and Nesic where the notion of the CLAR was introduced.[54] To determine the level of over-estimation within the van Hunnik model, the amount of $FeCO_3$ depositing onto a steel surface was investigated by Sun and Nesic[54] using the corrosion layer weight gain method. Experiments were performed in static solutions within a glass cell at a pH of 6.6 using a deoxygenated 1 wt.% NaCl solution at temperatures between 60 and 90°C. In various tests, supersaturation was varied from 10 to 300 through the addition of deoxygenated ferrous chloride solution. Steel samples were inserted into the test solution as the substrate for deposition measurements. Time averaged deposition rates were then performed by recording the difference in mass between the $FeCO_3$ covered sample and the mass once the corrosion product had been removed using Clarke's solution. The concentration of Fe^{2+} within the bulk solution was also monitored to evaluate the precipitation rate and to compare this with the CLAR.

In the first set of experiments (pH 6.6 and 80°C), the sample surface area within the 2 L glass cell was set at 5.4, 60 and 252 cm^2 (translating to A/V values of 12.6, 3 and 0.27 m^{-1}, respectively). For each experiment, an initial Fe^{2+} concentration of 50 ppm was used. For all tests, the precipitation rate determined by Fe^{2+} concentration measurements overestimated the quantity of $FeCO_3$ deposited onto the steel surface, particularly for small steel surface areas of 5.4 and 60 cm^2. However, as the surface area to volume ratio increased, the level of deposition became very similar to that of the predicted precipitation rate using Fe^{2+} measurements. Therefore the assumption holds for large surface area to volume ratios, but breaks down as the sample surface becomes smaller. Sun and Nesic showed that the implementation of the weight gain technique, although more cumbersome, offers a more realistic interpretation of the deposition rate.

When comparing the CLARs from a series of experiments with those predicted by van Hunnik et al.[83], large discrepancies were found. The data obtained from the weight-

change method produced rates of formation which were two orders of magnitude lower than those calculated using the van Hunnik et al.[83] model. Sun and Nesic therefore concluded that the assumptions involved with the Fe^{2+} method do not hold and should not be used to determine $FeCO_3$ CLARs.

The discrepancy between the van Hunnik et al. model and the Sun and Nesic model can be explained by precipitation elsewhere in the system. In relation to the two other remaining models (Greenberg and Tomson and Johnson and Tomson), these tests were derived based on experiments performed at low level of saturation (<2) and developed using the seeded crystal growth technique which is unlikely to involve nucleation of $FeCO_3$ crystals elsewhere in the system.[57] The fact that these two models were only validated at low saturation ratios, whilst the Sun and Nesic model was determined over much higher saturation ratios could also contribute to the observed discrepancy. In addition, the Sun and Nesic model is built on experimental work involving both the nucleation and growth onto a *steel substrate* whilst the Greenberg and Tomson and Johnson and Tomson models involve *purely growth on seed crystals*, which are both quite different processes. Again, this discussion is not to say that the two models are inaccurate in terms of predicting precipitation, merely to highlight that they focus on understanding two very different processes which produce drastically different rates of $FeCO_3$ formation.

In terms of modelling the precipitation process onto a steel surface, it is perhaps not surprising that the model proposed by Sun and Nesic[54] appears to be the most reliable. As additional validation, the precipitation rates determined by Yang et al.[187] using an electrochemical quartz crystal microbalance (EQCM) in static solutions onto an iron surface are very similar to the mass gain measurements performed by Sun and Nesic[54].

Based on the mass gain analysis performed by Sun and Nesic[54], a distinction was made between the homogeneous precipitation rate (P_{FeCO_3}) and the corrosion layer accumulation rate (CLAR). They argued that the use of previous models by Johnson and Tomson[59, 76, 102] and van Hunnik et al.[83] is inappropriate for CO_2 corrosion/precipitation involving carbon steel surfaces. In the case of the models by Johnson and Tomson[59, 76, 102], this is as a result of the A/V ratio which does not apply. As for van Hunnik et al.[83], the indirect Fe^{2+} concentration method leads to large errors when

determining CLAR. In light of this, Sun and Nesic[77] proposed a new empirical expression for the CLAR, founded on their direct mass-change results:

$$CLAR = e^{A_0 - \frac{E}{RT}} K_{sp}(S - 1) \tag{40}$$

where CLAR is the corrosion layer accumulation rate (i.e. the rate of precipitation onto the steel surface) in $mol \cdot m^{-2} s^{-1}$. This equation takes the same form and uses the same constants as that developed by Sun and Nesic in Table 5. However, the A/V ratio is omitted in this equation to make it applicable to a corroding steel surface. If all Fe^{2+} ions ultimately end up on the steel surface, then the relationship between the precipitation rate (P_{FeCO_3}) and the CLAR is:

$$P_{FeCO_3} = \frac{A}{V} CLAR \tag{41}$$

6. Challenges, priority research areas and techniques to further the understanding of $FeCO_3$ nucleation and growth

6.1 Current model limitations and suggested future research

The development of the Sun and Nesic[54] model has significantly improved the prediction of $FeCO_3$ precipitation kinetics onto carbon steel over a wide range of saturation ratios and temperatures. However, there are a number of factors which none of the four $FeCO_3$ models available in literature account for, which are likely to have a substantial effect on the precipitation of $FeCO_3$. Of the numerous factors which can influence precipitation kinetics, perhaps the two aspects which are least understood are that of the brine chemistry (i.e. the role of monovalent and divalent cations and anions) and the link between surface chemistry, CLAR and the role of mass-transfer.

It is suggested that future research needs to be directed towards understanding the conditions at the electrode-electrolyte interface and relating this to precipitation kinetics. In addition, the influence of more complex brine chemistries needs to be considered. However, what also needs to be reviewed are the approaches adopted when determining precipitation/deposition kinetics in laboratory-based studies. A number of limitations exist with current lab based techniques when quantifying precipitation in supersaturated solutions. That being said, a number of experimental techniques have been applied over

the past few years, which have the potential to improve our understanding of $FeCO_3$ precipitation, and these are reviewed below.

It is also suggested that to achieve an improved understanding of $FeCO_3$ precipitation kinetics, research should be directed towards methodologies which involve:

1. maintaining a stable solution chemistry in dynamic conditions
2. the application and/or development of quantitative *in situ* techniques to track the relationship between steel corrosion rate and precipitation behaviour
3. the implementation of combined experimental and modelling approaches to relate surface concentrations to precipitation

However, achieving each of these approaches presents challenges. The following subheadings consider each of the suggested methodologies and reviews either preliminary or complementary work in other research areas which can contribute towards achieving each of the aforementioned points in the context of $FeCO_3$ precipitation.

6.1.1 Maintaining a stable solution chemistry in dynamic conditions

One of the main experimental challenges in determining $FeCO_3$ accumulation rates, particularly over extended periods at low levels of supersaturation, is maintaining the saturation ratio over the duration of the test. This has been achieved to a certain extent by Sun and Nesic[54] in static conditions where the supersaturation was maintained approximately constant by adjusting the Fe^{2+} concentration. This was performed by continuously dosing the system with a deoxygenated ferrous chloride solution into the glass cell. Although this produced consistent data, the values were for static conditions at very high levels of supersaturation (>100).

There still remains a requirement to understand the kinetics of $FeCO_3$ precipitation at *low levels of bulk saturation in flowing conditions*. As stated previously, determining the influence of mass-transfer on the precipitation rate is an important step in establishing a reliable corrosion management strategy. The range of supersaturation of particular interest in terms of oil and gas transport is typically below 5 and achieving such a low constant supersaturation in dynamic conditions is particularly challenging experimentally for a closed system.

A number of published papers in both the corrosion and mineral scaling community perform free-drift experiments, or studies in batch systems, where there is no continuous feeding of constituents into the system with examples provided in the first part of the paper by Sun et al.[54] and the work of Alsaiari et al.[99]. When precipitation or dissolution occurs in a closed system, many factors such as the pH, ionic strength and the thermodynamic driving forces for precipitation change together. In order to fully understand and quantify precipitation kinetics, it is important to keep these parameters constant.

Interestingly, systems have been utilised in the mineral scaling community which provide a constant composition of a supersaturated solution with respect to scales such as calcium carbonate ($CaCO_3$) and calcium sulphate ($CaSO_4$)[104, 188-191]. These studies can be divided into three approaches; the use of constant composition continuous stirred tank reactors (CSTRs), and the application of once-through flow cells and a recently developed long-term continuous replenishment dynamic system. These are reviewed in the following sections.

6.1.1.1 Constant Composition Continuous Stirred Tank Reactors (CSTRs)

This methodology involves the use of a CSTR where two titrants are dosed into a reaction vessel to maintain the pH, ionic strength and concentrations of the species. The concept for this was initially introduced in 1978 by Tomson and Nancollas[192] and has been adapted in later studies by researchers from the same research institute[104, 105]. In these tests the output of a pH controller is compared to a pre-set value, with the difference in electrical potential controlling a motor of a syringe pump to deliver titrants from two syringes into the reactor cell. Examples of this work are provided by Rice University who considered the bulk precipitation of various carbonates[104]. In addition, a more simplistic implementation of this technique is performed in the second part of a publication by Sun et al.[54] where $FeCO_3$ precipitation onto a steel surface is considered. Depending upon the system, the control of this process and trying to maintain a stable chemistry can be particularly challenging, especially at high temperature when the kinetics of film formation are particularly rapid.

6.1.1.2 Once-through flow cells

Perhaps the most applicable and translatable study which could be applied to $FeCO_3$ deposition is the once-through flow cell as discussed in the paper by Bukuaghangin et al.[191] which was utilised to study the kinetics of barium sulphate ($BaSO_4$) scaling in the presence and absence of inhibitor. The design of the system was inspired from the cell developed by Euvrard et al.[193], which was actually applied in a closed system, resulting in a decrease in saturation ratio over time. This restricted kinetic studies to limited periods of time. In the work performed by Bukuaghangin et al.[191], the set-up was adjusted to include a once-through flow system. Essentially, two separate brines travel independently via peristaltic pumps through a thermostatic bath before entering a mixing chamber where the solutions are combined before surface deposition occurs within the cell. The cell enables saturation ratio to be maintained for long durations in a flowing system which would be beneficial for the study of $FeCO_3$ precipitation. One slight limitation of the cell is that only low flow rates can be generated, so studying the effect of high flowrates on precipitation is not possible. However, being able to ensure a constant fluid composition travelling past the steel sample addresses one of the significant short-comings associated with quantifying $FeCO_3$ precipitation kinetics. It could be possible to modify the system to cater for higher flow rates, however, large volumes of solution would be required to reach appreciable flow rates for significant periods of time, depending on the channel and sample sizes.

6.1.1.3 Continuous replenishment/flow-through dynamic system

The majority of CO_2 corrosion experiments tend to be conducted at either high levels of supersaturation to reach steady-state conditions rapidly, or the supersaturation is allowed to evolve naturally throughout the course of an experiment. Regrettably, most operating conditions in upstream pipelines do not translate to these 'easy to run' conditions.

In an effort to better simulate the long-term internal pipeline chemistry found in the field, Ieamsupapong et al.[156] developed a continuous replenishment system which was used to control the water chemistry by maintaining low saturation values (~1) with respect to $FeCO_3$ for an entire test duration. Figure 15(a) shows the dynamic flow-through system which consists of multiple feed solution containers and the working cell. A working

impeller (Figure 15(b)), housing test specimens resides within the working cell which is able to generate uniform flow and mass-transfer within the cell. The concentrations of species in the feed solution are adjusted based on the desired conditions within the working cell, and are able to maintain a stable pH and Fe^{2+} concentration in a dynamic environment.

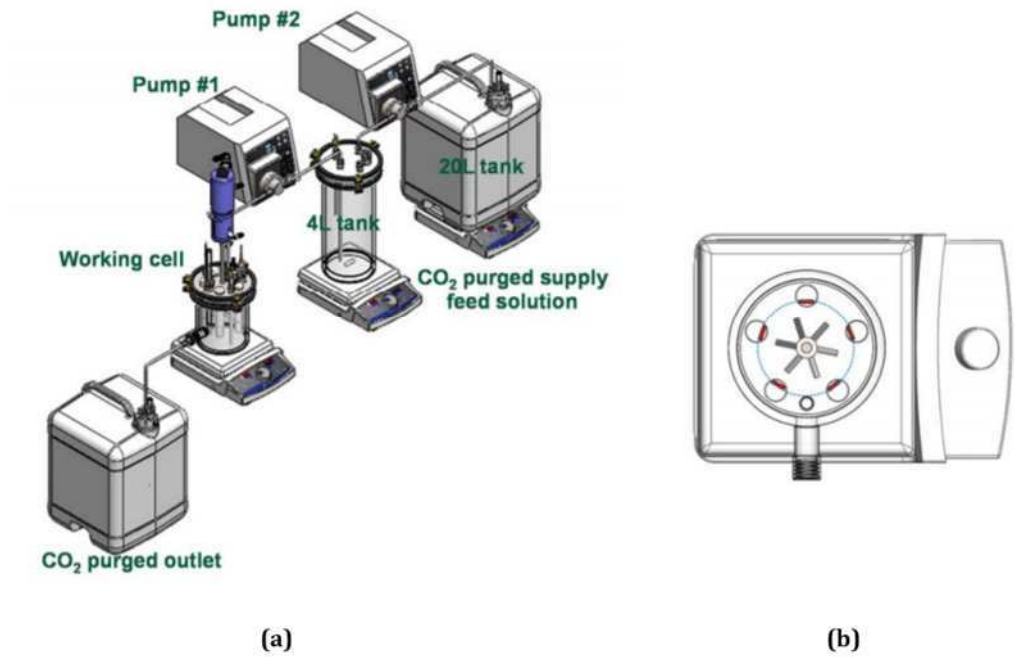

Figure 15: (a) Continuous replenishment setup to control solution pH and Fe^{2+} concentration and (b) top view of impeller/sample holder design to provide well-characterised hydrodynamics over sample – images adapted from Ieamsupapong et al.[156] and reproduced with permission from NACE International, Houston, TX. All rights reserved.

Figures 16(a) – (c) indicate the transient response of the Fe^{2+} concentration, pH and saturation ratio as a function of time for 9 days within the working cell. The target Fe^{2+} concentrations in these experiments were 40, 10 and 3 ppm at pH values of 5.4, 5.7 and 6, respectively. The results from the cell indicate that the system is capable of maintaining a very stable chemistry in a dynamic system at low saturation (which varied by a factor of two around a saturation level of one).

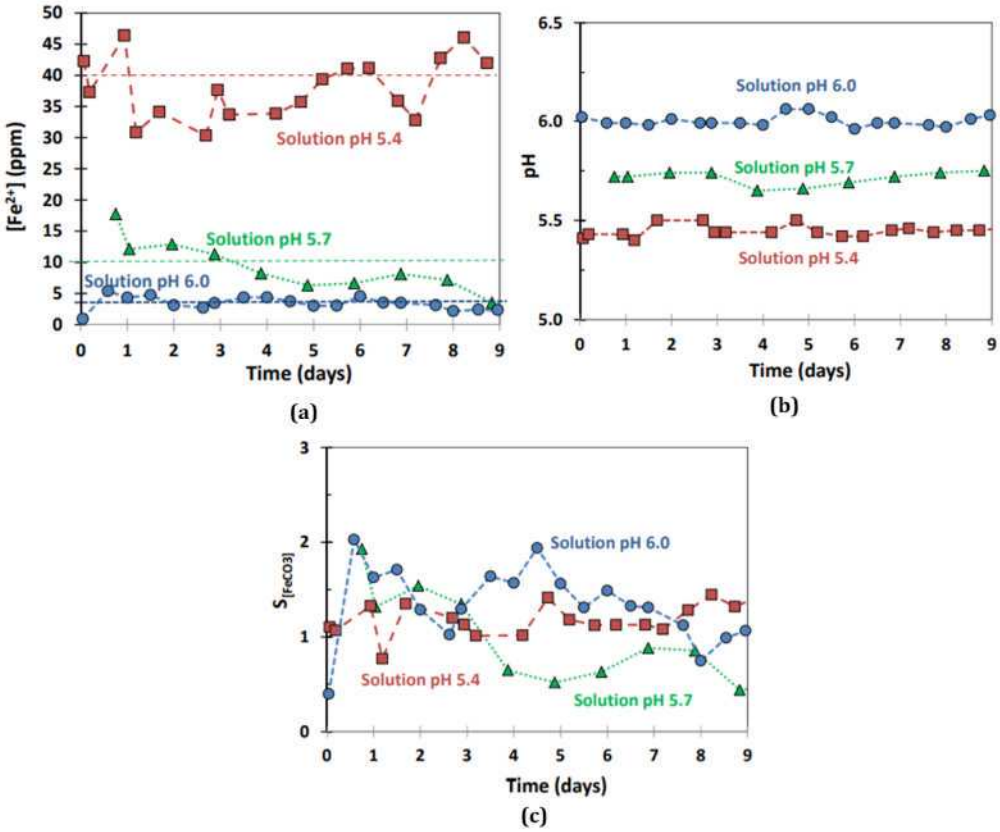

Figure 16: Comparison of (a) Fe^{2+}, (b) pH and (c) supersaturation change in the bulk solution over time using the constant replenishment/flow-through cell of from Ieamsupapong et al.[156]. Experiments ran for 9 days at a temperature of 80°C, pCO_2 of 0.54 bar and 0.6 m/s – images adapted from Ieamsupapong et al.[156] and reproduced with permission from NACE International, Houston, TX. All rights reserved.

6.1.2 Application and/or development of quantitative *in situ* techniques

Four key *in situ* techniques identified in the literature which hold promise for providing a deeper insight into $FeCO_3$ kinetics are:

- *In situ* visualisation of crystal nucleation and growth
- The electrochemical quartz crystal microbalance
- *In situ* synchrotron X-ray diffraction
- *In situ* X-ray microtomography

The first two techniques can be used predominantly to understand the earlier stages of precipitation (nucleation and growth), while the latter two techniques can be employed

to study both the early and later stages of precipitation. Each setup is reviewed in-turn in the following sections:

6.1.2.1 *In situ* visualisation of crystal nucleation and growth

During the early stages of $FeCO_3$ precipitation, it has been shown that the suppression of corrosion rate is largely achieved through a surface blocking effect on the steel substrate[144]. Once the initial layer of crystals is formed, the increase in thickness of the porous $FeCO_3$ network is then capable of acting as a diffusion barrier to electrochemically active species.

One possible method of understanding the coverage and growth of $FeCO_3$ during the earlier stages of growth is to monitor the surface with *in situ* visualisation techniques that can provide information on nucleation and growth kinetics. In addition to creating a once-through flow cell to enable continuous flow of a supersaturated fluid over a steel surface, Sanni et al.[189, 190] and Bukuaghangin et al.[191] extended their setup (discussed earlier) to provide real-time visualisation of mineral scale build-up. The surface deposition kinetics were followed by a high resolution camera linked to a computer. The camera enabled real-time observations and instantaneous image capture of scale deposition on the steel surfaces inserted into the *in situ* flow cell. Each captured image was then processed using a MATLAB programme, utilising the difference in contrast of the bare steel surface and the crystals that had formed. Once processing the image, the programme then produced a binary output image in black and white which can be used to determine the surface coverage, crystal size and number of crystals present on the steel substrate. There exists the potential to extend this study to $FeCO_3$ precipitation, however challenges may exist in the image processing stage as the contrast may be different for $FeCO_3$ deposition onto a corroding carbon steel surface as compared to $CaCO_3$/$BaSO_4$ deposition onto a non-corroding stainless steel surface.

6.1.2.1 The electrochemical quartz crystal microbalance (EQCM)

Another technique for monitoring the very early stages of $FeCO_3$ nucleation and growth is the electrochemical quartz crystal microbalance (EQCM). The EQCM is a device capable of measuring (in real time) very small changes in mass based on the frequency shift of a piezoelectric quartz crystal. The device not only possesses nanogram sensitivity, but it also enables simultaneous electrochemical measurements, making it useful in the study

of $FeCO_3$ precipitation kinetics in CO_2 containing environments. The correlation between mass and frequency of the EQCM is described by the Sauerbrey equation[194]:

$$\Delta f = -\frac{2f_0^2}{\sqrt{\mu_q \rho_q}} \cdot \Delta m \qquad (42)$$

Where Δf is the frequency change (Hz), Δm is the change in mass per unit area (g/cm^2), f_0 is the resonant frequency of the fundamental mode of the crystal (Hz), μ_q is the shear modulus of quartz (g/cm/s^2) and ρ_q is the density of quartz (g/cm^3).

In an initial paper, Yang et al.[187] evaluated the capability of the EQCM to measure the mass change due to dissolution *in situ* during CO_2 corrosion. This was followed by studying film formation and removal (via chemical dissolution) of $FeCO_3$. The EQCM was able to accurately determine the dissolution behaviour of an iron coated quartz crystal in a 1 wt.% NaCl solution at 25 and 80°C when corroding naturally and when under potentiostatic control.

In subsequent tests, the precipitation kinetics of $FeCO_3$ were determined at 80°C and pH 6.6 in a 1 wt.% NaCl solution saturated with CO_2 on both polarized gold and iron coated quartz crystals for the ultimate purpose of performing $FeCO_3$ dissolution experiments. In tests where deposition onto iron was measured, the EQCM was able to identify the early stages of film growth, producing precipitation rates comparable with the model of Sun and Nesic[54]. The technique was particularly useful as it not only provided real time measurements of precipitation, but arguably provides a more accurate measurement of mass gain, which is sometimes challenging when using a microbalance in conjunction with the mass gain technique. Yang et al.[187] was also able to control the kinetics of $FeCO_3$ precipitation onto gold electrodes by applying cathodic potentials to the quartz crystal. However, the coverage of $FeCO_3$ was observed to be better on the iron electrodes, making them more suitable for the dissolution experiments performed.

6.1.2.2 *In situ* synchrotron radiation X-ray diffraction (SR-XRD)

X-ray techniques are particularly important in terms of electrode/electrolyte interaction studies. X-ray diffraction (XRD) is able to provide information on phase composition, orientation, surface texture, strain and transformations. One of the most powerful advantages of this technique is that it can be used for *in situ* studies which enable surfaces to be examined when exposed to an electrolyte in realistic environmental conditions. However, such studies require attention to detail in terms of the electrochemical cells developed, as well as access to the instrumentation required for synchrotron studies, which can be particularly expensive.

Recent work by Burkle et al.[195, 196], Ingham et al.[93, 139, 140], Ko et al.[136-138] and Sk et al.[18] has demonstrated the ability of synchrotron radiation x-ray diffraction (SR-XRD) to provide qualitative and quantitative information in relation to $FeCO_3$ precipitation kinetics. Burkle et al.[195, 196] presented the design of an *in situ* SR-XRD flow cell instrumented with electrochemistry for corrosion measurements. The flow cell was utilised to follow both the nucleation and growth behaviour of corrosion products and the evolution of the phases present during the CO_2 corrosion of X65 carbon steel surfaces in real-time. This particular study focused on a CO_2-saturated 3.5 wt.% NaCl brine at 80°C and a flow rate of 0.1 m/s at pH values of 6.3, 6.8 and 7. $FeCO_3$ was shown to be the only crystalline phase to form in all conditions. The comparison between XRD main peak area intensities and $FeCO_3$ surface coverage, mass and volume demonstrated that there was a qualitative relationship between these parameters at each pH, providing information on the kinetics of film formation. The results also indicated that the observed trend had potential to be developed into a quantitative relationship. A schematic and image of the setup used is provided in Figure 17, while some of the typical results from the experiment at a specific pH are provided in Figure 18 for a pH of 7 at 80°C. Unfortunately, the limitation of this particular method was that the flow system was recirculating, resulting in the chemistry of the solution changing with time. However, this could be rectified through conversion into a once-through system.

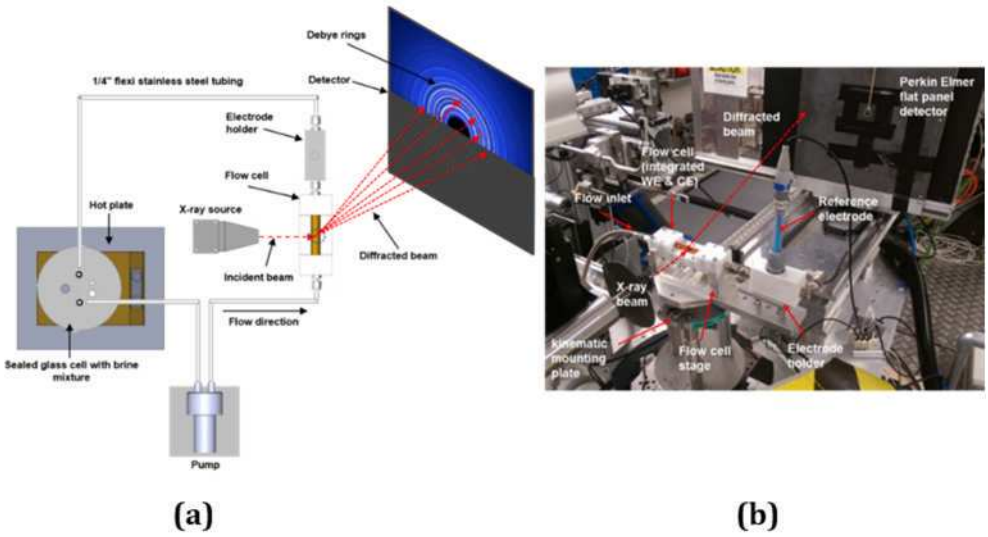

Figure 17: The flow cell set-up during Synchrotron experiments performed by Burkle et al.[195] (a) Photograph and (b) schematic of the flow cell set-up used on the Diamond Light Source beamline (I15) – image adapted from Burkle et al.[195]

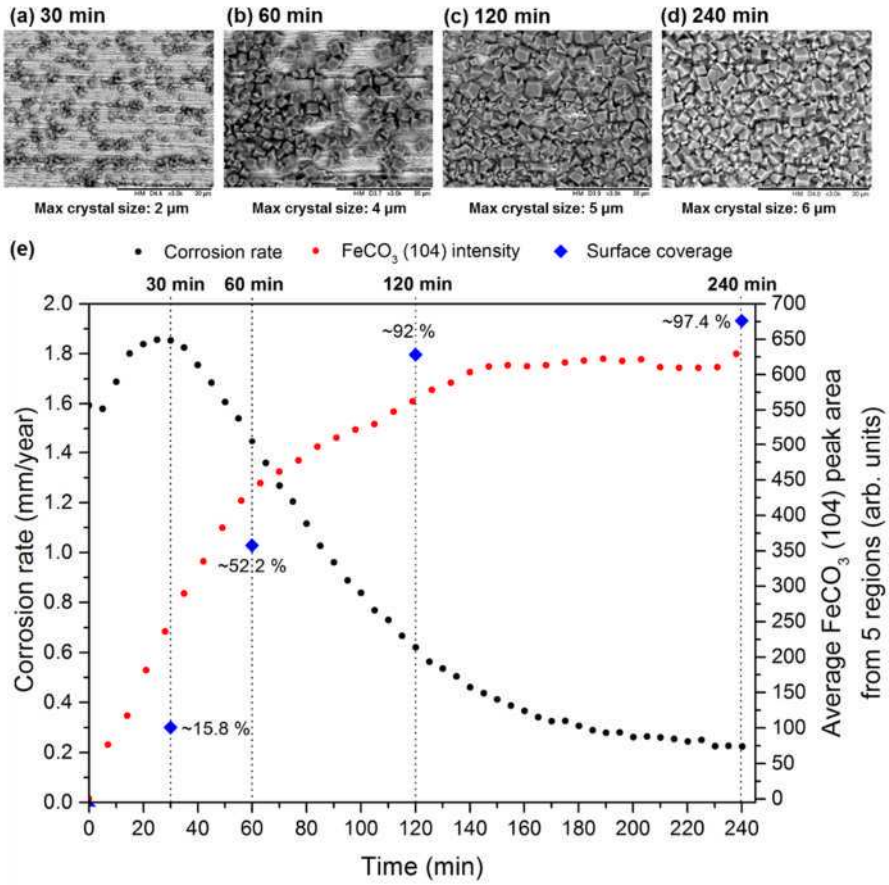

Figure 18: Development of the $FeCO_3$ crystals; (a)-(d) SEM images as a function of time (scale bar corresponds to 30 µm and data collected from laboratory repeats); (e) *In situ* corrosion rate and major $FeCO_3$ (104) average peak area versus time collected at beamline I15, conducted in a CO_2-saturated 3.5 wt.% NaCl solution at 80°C, 0.54 bar pCO_2 and 0.1 m/s at pH 7[196] – image adapted from Burkle et al.[196]

6.1.2.3 *In situ* X-ray microtomography

The latter stages of $FeCO_3$ growth are associated with the development of a thicker, porous layer which changes in structure during its development. This film growth and change in porosity and permeability with time also influences the corrosion rate in addition to the surface blocking effect provided by the initial accumulation of the film on the steel surface[116].

Developing a full understanding of the porosity and permeability of a $FeCO_3$ layer and how this evolves over time is one of the key requirements to improve prediction models of $FeCO_3$ growth. Such a mechanistic model for film formation was developed by Nesic et al.[116], however, the proposed variations in film porosity from the model as a function of thickness and the various operating conditions were not extensively validated experimentally.

If it is possible to track the changes in porosity, tortuosity and permeability of $FeCO_3$ films and relate changes in such properties to the transient corrosion behaviour of the underlying substrate, such an approach could assist greatly the development of models to accurately predict the growth mechanism and protection afforded by $FeCO_3$ layers. One such technique which holds the ability to achieve such an understanding is x-ray microtomography.

X-ray microtomography is a method for imaging structures in three dimensions with resolution on the micron length scale[197]. As well as being a non-destructive technique, it can also study specimens immersed in an electrolyte[197], making it an ideal method for the *in situ* monitoring of $FeCO_3$ formation on a substrate. The latest generation of synchrotron facilities have made it possible to achieve micrometre to sub-micron resolution, which has generated increased interest from the material characterisation community[198].

In the last decade, advances in laboratory based instruments have enabled resolution at sub-micron level, providing a viable alternative to synchrotron sources. The systems operate on the same principles, however, they suffer from the disadvantages of long scan times and many orders of magnitude lower flux capacity, making them currently unsuitable for examining the changes and development in corrosion product formation *in situ* when the kinetics are particularly fast, as one of the fundamental requirements of X-ray tomography is that the microstructure does not change significantly during the scan period[197]. However, the application of synchrotron X-ray microtomography does not suffer from such shortcomings, possessing 1000 times greater flux, fast scan times and superior resolution[198].

Regardless of the X-ray source, microtomography is now making significant contributions in the field of 3D analysis, helping material engineers to understand structures in far greater detail than those captured by standard surface microscopy techniques[199]. A detailed review of the many morphological parameters that can be extracted using X-ray tomography of porous materials is presented by Maire et al.[200]. In this work, a selection of cellular ceramics were analysed which possessed different morphologies and pore sizes. Figure 19 shows images of the materials investigated as well as their pore thickness distribution. From such images it is also possible to extract parameters such as tortuosity of the network (i.e. the ratio of the length of the path between two points in the porous network over their distance in a straight line) in addition to the porosity.

A similar study was conducted by Brabant et al.[201] who compared a number of porous materials, including limestone, pine wood and aluminium foam. Their methodology for analysis involved dividing the network of pores into subdomains. Such an approach enabled the porosity, equivalent diameter and orientation of the pores to be quantified. This method of separation also facilitated the construction of a simplified skeleton of the pore network or solid phase, which could be particularly beneficial as an input for the modelling of species transport to determine properties such as permeability. Application of this methodology to understand the permeability of $FeCO_3$ corrosion product films and their porosity variation with thickness would provide useful data to correlate with mechanistic models to improve the understanding of how such films develop.

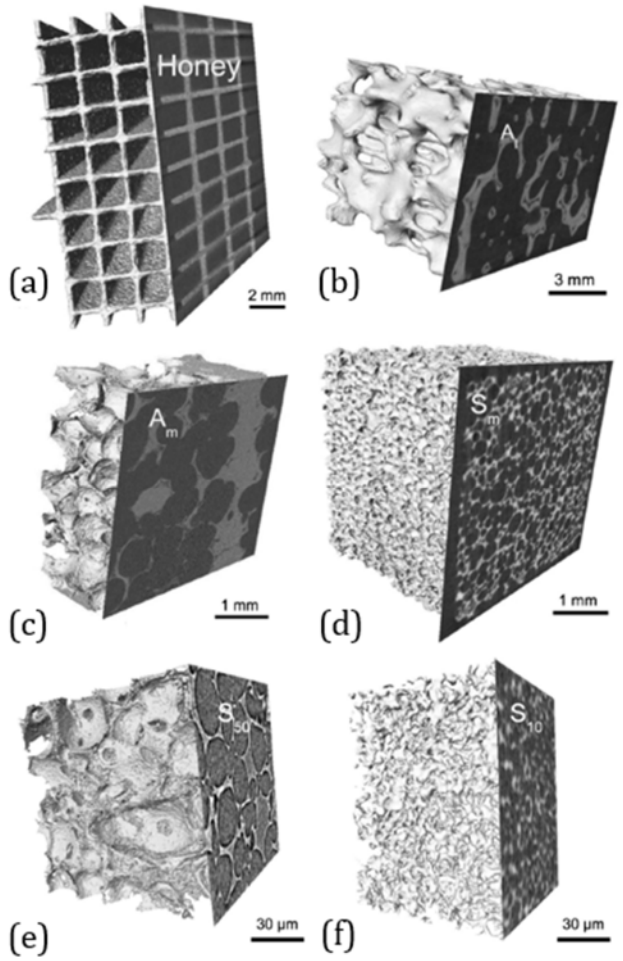

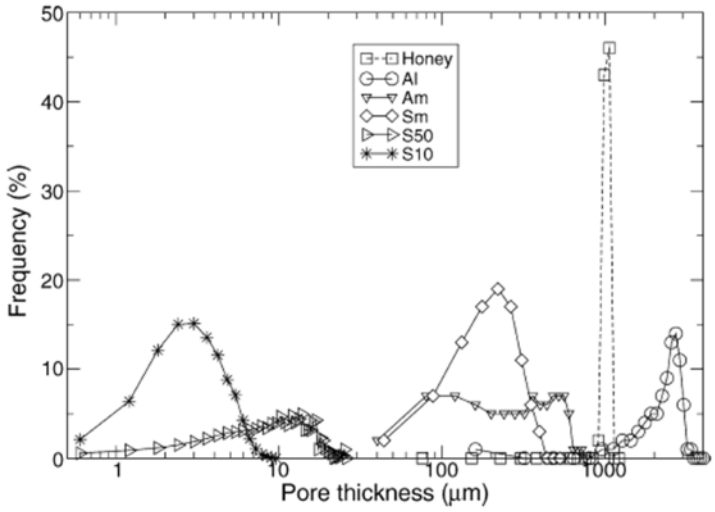

(g)

Figure 19: 3D view and grey level tomographic slice for six samples (a) honeycomb, (b)/(c) two aluminium foams, (d)/(e)/(f) three preceramic polymers. Figure 19(f) shows the pore size distribution of each network obtained after processing the tomographic images – images adapted from Maire et al.[200]

6.1.3 Implementation of combined experimental and modelling approaches to relate surface concentrations to precipitation

As alluded to earlier in this review, Fe^{2+} is generated at the steel surface during corrosion, while H^+ ions are consumed on the steel surface or the film surface (if the film is Fe_3C) prior to protective film formation. The evolution of concentration gradients from the bulk solution to the steel surface results in higher supersaturation in the film and/or at the metal surface, which can increase the level of precipitation at the surface.[15] This effect is likely to be more substantial at low bulk saturation values as compared to highly supersaturated solutions.

A concerted effort needs to be directed towards not only understanding bulk solution chemistry, but determining surface corrosion rates/reactions and how this influences the surface pH and concentration of Fe^{2+}. This will be the key to understanding the precipitation process and accurately predicting the rate of $FeCO_3$ growth.

To date, the state-of-the-art in terms of predicting the concentration profile from a corroding carbon steel surface into a bulk solution under hydrodynamic conditions (in open literature) is that of the mechanistic model developed by Nordsveen et al.[122] and Nesic et al.[123] for CO_2 corrosion. The model takes into consideration electrochemical reactions at the steel surface, diffusion of species between the metal surface and the bulk (including diffusion through porous surface films), migration due to establishment of potential gradients, and homogenous chemical reactions. The model can predict the corrosion rate as well as the concentration profiles for all species present in the brine from the steel surface into the bulk solution. The model by Nordsveen et al.[122] and Nesic et al.[123] is arguably the most comprehensive mechanistic model to date.

As part of a series of numerical experiments using the developed model, Nesic et al.[123] compared the saturation ratio at the steel surface to that of the bulk solution for the flow of a brine solution at 1 m/s through a 0.01m diameter pipe at 1 bar pCO_2 and 20°C, with an Fe^{2+} content of 1 ppm. Figure 20 shows the predicted saturation profile. The figure illustrates the error which can potentially be made when considering if precipitation of $FeCO_3$ is thermodynamically favourable. For example, in this particular environment, one could argue that precipitation is not thermodynamically favourable below a bulk pH of

6.6. However, the surface of the steel exceeds saturation with respect to $FeCO_3$ for a bulk pH of 6.

The corrosion of the steel surface results in a higher pH at the interface. This reduces the concentration of Fe^{2+} required to exceed the solubility of $FeCO_3$ which when combined with the high Fe^{2+} concentration at the surface results in an increased level of supersaturation at the surface. At present, none of the models proposed within literature for $FeCO_3$ formation are correlated with surface precipitation rates. They are all based on correlations with bulk saturation ratios.

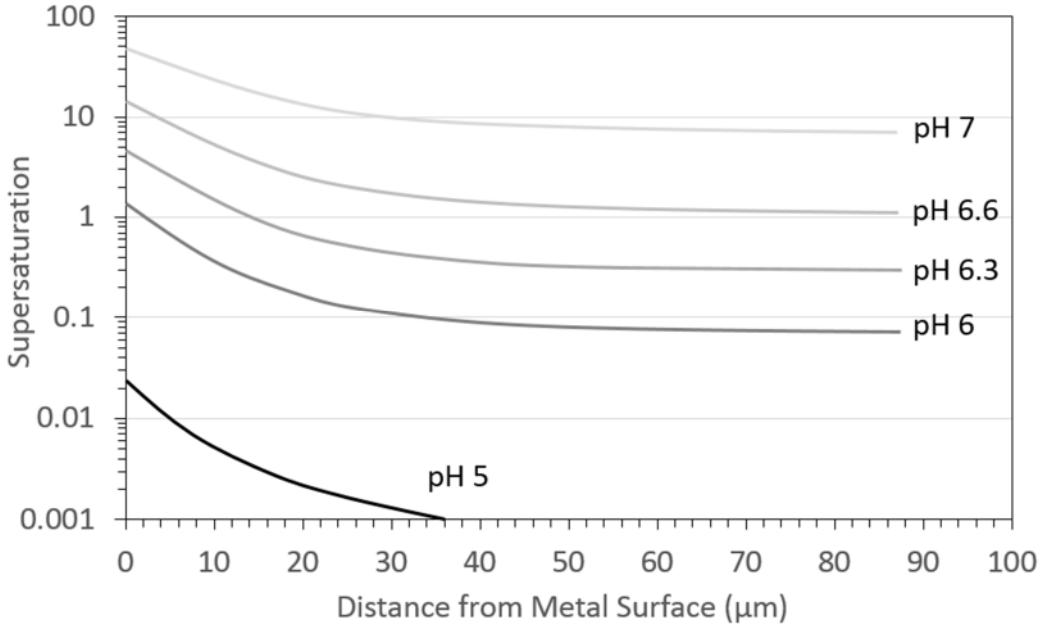

Figure 20: Difference between the bulk and surface conditions at different pH for T = 20°C, pCO_2 = 1 bar, cFe^{2+} = 1 ppm, v = 1 m/s, and d = 0.01 m based on the model by Nordsveen et al.[122] and Nesic et al.[123] – image adapted from Nesic et al.[123]

One identified study within literature focused on understanding precipitation processes onto electrode surfaces by correlating precipitation rates with predicted surface pH measurements and species concentrations. However, this study by Tlili et al.[202] was conducted in an oxygenated environment and considered the role of pH at the electrode/solution interface on $CaCO_3$ precipitation. Nonetheless, the principle of the technique could be translated to a deaerated environment for $FeCO_3$ precipitation where different cathodic reactions dominate. The study involved modelling the oxygen reduction reaction at the electrode as a function of applied potential along with the

homogeneous chemical dissociation reactions in a CO_2 system and the diffusion processes of each species, whilst also accounting for electro-neutrality to determine the pH at the electrode/solution interface. This work built on the initial model of Deslouis et al.[203] for seawater and enabled Tlili et al.[202] to extract concentration profiles for OH^-, HCO_3^-, CO_3^{2-} and Ca^{2+} as a function of distance from the surface for a polarised gold electrode. The model ultimately enabled the supersaturation at the gold electrode to be determined as a function of applied potential for a given set of bulk solution conditions. The local pH and supersaturation values were compared with the electro-gravimetric measurements from a gold coated quartz crystal microbalance. The results confirmed that precipitation was possible on the gold surface even when the bulk solution is under-saturated with respect to calcite, proving that surface composition is critical in the precipitation process. There is the potential to adapt this technique to $FeCO_3$ deposition to provide a more fundamental understanding on the role of surface chemistry on the deposition process. However, studying $FeCO_3$ precipitation is made slightly more complicated by the fact that the system needs to be oxygen free. Nonetheless, there is potential in this methodology for it to be adapted for $FeCO_3$ formation studies.

7. Conclusions

Internal pipeline corrosion as a result of dissolved CO_2 in process fluids is one of the main obstacles towards successful oil and gas production. When the product of the activities of Fe^{2+} and CO_3^{2-} ions exceeds the solubility product, it becomes thermodynamically possible for $FeCO_3$ to form from the solution and dramatically reduce the corrosion rate by precipitation of a porous crystalline layer directly onto the steel surface. This paper has consolidated the information in the literature relating to $FeCO_3$ formation in the oil and gas industry and generated the following conclusions:

- Factors which influence the kinetics of $FeCO_3$ formation include: (i) the solubility of $FeCO_3$, (ii) environmental conditions, (iii) operating conditions and (iv) the material and interfacial properties of the steel.
- The solubility product is influenced by temperature, an increase in which reduces solubility. This behaviour is very important since the driving force for precipitation of $FeCO_3$ is the saturation ratio (S) of $FeCO_3$. However, it is clear that challenges exist experimentally when deciphering even the solubility product of $FeCO_3$ as a function of temperature. Of the various empirical expressions for

solubility product in the literature, the model of Sun and Nesic[53], which accounts for temperature (as well as the influence of ionic strength on ion activity), appears to be the most reliable. Accurate prediction of K_{sp} (and ultimately S) is the first step in producing reliable estimates of precipitation kinetics.

- The protectiveness of $FeCO_3$ is influenced by several environmental factors such as temperature, pH, CO_2 partial pressure and ferrous ion concentration, which can affect precipitation behaviour either directly, or indirectly. The morphology and protectiveness strongly depend on the rate at which $FeCO_3$ accumulates on the steel surface and hence the value of S for $FeCO_3$. Typically, a high S is required to obtain appreciable levels of $FeCO_3$ precipitation onto the steel surface, although this is again dependant on pH and temperature.
- Increasing pH has a profound effect on the morphology and level of protection offered by $FeCO_3$ films, improving corrosion resistance significantly. For temperatures <40°C lower precipitation rates are established and a loosely adherent, porous film can result, although some studies have observed the formation of protective films at room temperature with a high pH and very high level of supersaturation.
- One influential environmental property which has received less attention is the role of brine chemistry on precipitation. The presence of additional dissolved salts other than NaCl not only affects ionic strength, but high concentrations of certain species (e.g. Ca^{2+}) can promote the formation of different, competing scales in preference to $FeCO_3$, which alter the level of protection afforded to the steel surface.
- In addition to the rate of $FeCO_3$ accumulation on the steel surface, the corrosion rate of the underlying steel is also an important consideration as this effectively 'undermines' the film. If the precipitation rate significantly exceeds that of the corrosion rate, then a dense, adherent, protective layer is anticipated which can be very thin (<10 μm). Conversely, if the corrosion rate exceeds the rate of $FeCO_3$ formation, a porous and poorly protective film is likely to develop, which can be particularly thick (~100 μm or greater).
- The formation and adhesion of the $FeCO_3$ layer has also been related to the presence of iron carbide (Fe_3C) which can act as a diffusion barrier, increasing the local pH and Fe^{2+} concentration. However, the effect of this layer has not been fully

explored, yet has the potential to be critical in dictating whether a protective layer develops.

- Determining the bulk solution chemistry alongside the surface corrosion rates/reactions and identifying how this influences the surface pH and local S appears to be the key to understanding the precipitation process and accurately predicting the rate of $FeCO_3$ growth. Four models of the precipitation rate of $FeCO_3$ exist in the open literature and the model of Sun and Nesic[54] is arguably the most reliable for predicting the rate at which corrosion products accumulate on a corroding steel surface (for reasons which are discussed in detail in this review). However an important limitation of all current models is that they ignore the link between surface chemistry, precipitation rate and mass transfer, expressing the precipitation rate as a function of bulk S.
- One important study, (albeit in the context of $CaCO_3$ precipitation[202]), has shown that precipitation is possible even when the bulk solution is under-saturated, demonstrating the importance of understanding the steel-electrolyte interface conditions in precipitation studies. These influences in $FeCO_3$ precipitation are poorly understood and further research is needed towards creating methodologies that can maintain a stable solution chemistry in dynamic conditions, in order to track the relationship between corrosion rate and $FeCO_3$ precipitation. Four *in situ* experimental techniques that are worthy of further development are: visualisation of crystal nucleation, synchrotron radiation X-ray diffraction, microtomography and electrochemical quartz crystal microbalance. These methods may provide the foundations for a new, combined experimental and modelling approach to relate surface concentrations to precipitation, thus providing greater understanding of the key mechanisms influencing $FeCO_3$ precipitation.

8. References

1. A. Dugstad. "The importance of $FeCO_3$ supersaturation on the CO_2 corrosion of mild steels", CORROSION 92, (Houston TX: NACE, 1992).
2. J. Han, S. Nešić, Y. Yang, and B.N. Brown, "Spontaneous passivation observations during scale formation on mild steel in CO_2 brines", Electrochimica Acta, 56, 15 (2011): p. 5396-5404.

3. J. Han, D. Young, H. Colijn, A. Tripathi, and S. Nešić, "Chemistry and Structure of the Passive Film on Mild Steel in CO_2 Corrosion Environments", Industrial & Engineering Chemistry Research, 48, 13 (2009): p. 6296-6302.

4. J. Han, Y. Yang, S. Nešić, and B.N. Brown. "Roles of Passivation and Galvanic Effects in Localized CO_2 Corrosion of Mild Steel", CORROSION 2008, (New Orleans, LA:NACE, 2008).

5. J. Han, Y. Yang, B. Brown, and S. Nešić. "Electrochemical investigation of localized CO_2 corrosion on mild steel", CORROSION 2007, (Nashville, TN:NACE, 2007).

6. G. Schmitt and M. Horstemeier. "Fundamental aspects of CO_2 metal loss corrosion - Part II: Influence of different parameters on CO_2 corrosion mechanisms", CORROSION 2006, (San Diego, CA: NACE, 2006).

7. S. Nešić, "Key issues related to modelling of internal corrosion of oil and gas pipelines–A review", Corrosion science, 49, 12 (2007): p. 4308-4338.

8. M. Kermani and A. Morshed, "Carbon dioxide corrosion in oil and gas production - A compendium", Corrosion, 59, 8 (2003): p. 659-683.

9. G. Schmitt. "Fundamental aspects of CO_2 metal loss corrosion. Part II: Influence of different parameters on CO_2 corrosion mechanism", CORROSION 2015, (Dallas, TX: NACE, 2015).

10. A. Dugstad. "Fundamental aspects of CO_2 metal loss corrosion, Part I: Mechanism", CORROSION 2015, (Dallas, TX: NACE, 2015).

11. A. Kahyarian, M. Achour, and S. Nesic, "Chapter 7 - CO_2 corrosion of mild steel", Trends Oil Gas Corrosion Research and Technology, (2017): p. 149-190.

12. A. Kahyarian, M. Singer, and S. Nesic, "Modeling of uniform CO_2 corrosion of mild steel in gas transportation systems: A review", Journal of Natural Gas Science and Engineering, 29, Supplement C (2016): p. 530-549.

13. J.A. Dougherty. "A review of the effect of organic acids on CO_2 corrosion", CORROSION 2004, (New Orleans, LA: NACE, 2004).

14. R. Barker, Y. Hua, and A. Neville, "Internal corrosion of carbon steel pipelines for dense-phase CO_2 transport in carbon capture and storage (CCS)–a review", International Materials Reviews, 62, 1 (2017): p. 1-31.

15. A. Dugstad. "Fundamental aspects of CO_2 metal loss corrosion - Part 1: Mechanism", CORROSION 2006, (San Diego, CA: NACE International Conference, 2006).

16. *EPSRC Grant EP/R00496X/1: Preventing Surface Degradation in Demanding Environments*. 2017 [cited 2018 17/05/2018]; Available from: http://gow.epsrc.ac.uk/NGBOViewGrant.aspx?GrantRef=EP/R00496X/1.

17. *Corrosion Chemistry: Faraday Discussion*. 2015 [cited 2018 17/05/2018]; Available from: http://www.rsc.org/events/detail/12120/corrosion-chemistry-faraday-discussion.

18. M.H. Sk, A.M. Abdullah, M. Ko, B. Ingham, N. Laycock, R. Arul, and D.E. Williams, "Local supersaturation and the growth of protective scales during CO_2 corrosion of steel: effect of pH and solution flow", Corrosion Science, (2017).

19. B. Linter and G. Burstein, "Reactions of pipeline steels in carbon dioxide solutions", Corrosion science, 41, 1 (1999): p. 117-139.

20. C. De Waard and D. Milliams, "Carbonic acid corrosion of steel", Corrosion, 31, 5 (1975): p. 177-181.

21. R.F. Weiss, "Carbon dioxide in water and seawater: the solubility of a non-ideal gas", Marine chemistry, 2, 3 (1974): p. 203-215.

22. Z. Duan, R. Sun, C. Zhu, and I.-M. Chou, "An improved model for the calculation of CO_2 solubility in aqueous solutions containing Na^+, K^+, Ca^{2+}, Mg^{2+}, Cl^-, and SO_4^{2-}", Marine Chemistry, 98, 2-4 (2006): p. 131-139.

23. Z. Duan and R. Sun, "An improved model calculating CO2 solubility in pure water and aqueous NaCl solutions from 273 to 533 K and from 0 to 2000 bar", Chemical geology, 193, 3-4 (2003): p. 257-271.

24. J.N. Butler, *Carbon dioxide equilibria and their applications*. 1991: CRC Press.

25. S. Nesic, "Effects of multiphase flow on internal CO_2 corrosion of mild steel pipelines", Energy & Fuels, 26, 7 (2012): p. 4098-4111.

26. J.M. Bockris, J. McBreen, and L. Nanis, "The hydrogen evolution kinetics and hydrogen entry into a-iron", Journal of the Electrochemical Society, 112, 10 (1965): p. 1025-1031.

27. N. Pentland, J.M. Bockris, and E. Sheldon, "Hydrogen evolution reaction on copper, gold, molybdenum, palladium, rhodium, and iron mechanism and measurement technique under high purity conditions", Journal of The Electrochemical Society, 104, 3 (1957): p. 182-194.

28. J.M. Bockris and E. Potter, "The mechanism of the cathodic hydrogen evolution reaction", Journal of The Electrochemical Society, 99, 4 (1952): p. 169-186.

29. M. Devanathan and Z. Stachurski, "The mechanism of hydrogen evolution on iron in acid solutions by determination of permeation rates", Journal of the electrochemical society, 111, 5 (1964): p. 619-623.

30. T. Tran, B. Brown, and S. Nesic. "Corrosion of mild steel in an aqueous CO_2 environment - basic electrochemical mechanisms revisited", CORROSION 2015, (Dallas, TX:NACE, 2015).

31. M. Singer, L. Chong, A. Mohsen, and A. Jenkins. "Top of line corrosion - Part 1: Review of the mechanism and laboratory experience", CORROSION 2014, (San Antonio, TX:NACE, 2014).

32. E. Remita, B. Tribollet, E. Sutter, V. Vivier, F. Ropital, and J. Kittel, "Hydrogen evolution in aqueous solutions containing dissolved CO_2: quantitative contribution of the buffering effect", Corrosion Science, 50, 5 (2008): p. 1433-1440.

33. J. Han, J. Zhang, and J.W. Carey, "Effect of bicarbonate on corrosion of carbon steel in CO_2 saturated brines", International Journal of Greenhouse Gas Control, 5, 6 (2011): p. 1680-1683.

34. A. Kahyarian, B. Brown, and S. Nesic, "Electrochemistry of CO_2 corrosion of mild steel: Effect of CO_2 on cathodic currents", CORROSION, 74, 8 (2018): p. 851-859.

35. F.V. De Sousa, P.R. Viana, B. Tribollet, O.E. Barcia, and O.R. Mattos, "Hydrogen evolution reaction evaluation in aqueous solutions containing CO_2 at different pressures", Journal of The Electrochemical Society, 164, 6 (2017): p. C294-C299.

36. A. Kahyarian, A. Schumaker, B. Brown, and S. Nesic, "Acidic corrosion of mild steel in the presence of acetic acid: Mechanism and prediction", Electrochimica Acta, 258, (2017): p. 639-652.

37. A. Kahyarian, B. Brown, and S. Nešić, "Mechanism of cathodic reactions in acetic acid corrosion of iron and mild steel", Corrosion, 72, 12 (2016): p. 1539-1546.

38. J.M. Bockris and D. Drazic, "The kinetics of deposition and dissolution of iron: effect of alloying impurities", Electrochimica acta, 7, 3 (1962): p. 293-313.

39. J.M. Bockris, D. Drazic, and A. Despic, "The electrode kinetics of the deposition and dissolution of iron", Electrochimica Acta, 4, 2-4 (1961): p. 325-361.

40. A. Atkinson and A. Marshall, "Anodic dissolution of iron in acidic chloride solutions", Corrosion Science, 18, 5 (1978): p. 427-439.

41. A. El Miligy, D. Geana, and W. Lorenz, "A theoretical treatment of the kinetics of iron dissolution and passivation", Electrochimica Acta, 20, 4 (1975): p. 273-281.

42. M. Keddam, O.R. Mottos, and H. Takenouti, "Reaction model for iron dissolution studied by electrode impedance I. Experimental results and reaction model", Journal of the Electrochemical Society, 128, 2 (1981): p. 257-266.

43. M. Keddam, O.R. Mattos, and H. Takenouti, "Reaction model for iron dissolution studied by electrode impedance II. Determination of the reaction model", Journal of The Electrochemical Society, 128, 2 (1981): p. 266-274.

44. L. Felloni, "The effect of pH on the electrochemical behaviour of iron in hydrochloric acid", Corrosion Science, 8, 3 (1968): p. 133-148.

45. D.M. Dražić, *Iron and its Electrochemistry in an Active State*, in *Modern Aspects of Electrochemistry*. 1989, Springer. p. 69-192.

46. K. Heusler, "Der Einfluß der Wasserstoffionenkonzentration auf das elektrochemische Verhalten des aktiven Eisens in sauren Lösungen Der Mechanismus der Reaktion $Fe \rightleftharpoons Fe^{2+} + 2e$", Berichte der Bunsengesellschaft für physikalische Chemie, 62, 5 (1958): p. 582-587.

47. T. das Chagas Almeida, M. Bandeira, R. Moreira, and O. Mattos, "Discussion on "Electrochemistry of CO_2 corrosion of mild steel: Effect of CO_2 on iron dissolution reaction" by A. Kahyarian, B. Brown, S. Nesic,[Corros. Sci. 129 (2017) 146–151]", Corrosion Science, 133, (2018): p. 417-422.

48. S. Nesic, N. Thevenot, J.-L. Crolet, and D. Drazic. "Electrochemical properties of iron dissolution in the presence of CO_2-Basics revisited", CORROSION 96, (Houston, TX:NACE, 1996).

49. T. das Chagas Almeida, M.C.E. Bandeira, R.M. Moreira, and O.R. Mattos, "New insights on the role of CO_2 in the mechanism of carbon steel corrosion", Corrosion Science, 120, (2017): p. 239-250.

50. A. Kahyarian, B. Brown, and S. Nesic, "Electrochemistry of CO_2 corrosion of mild steel: Effect of CO_2 on iron dissolution reaction", Corrosion Science, 129, (2017): p. 146-151.

51. I.S. Cole, P. Corrigan, S. Sim, and N. Birbilis, "Corrosion of pipelines used for CO_2 transport in CCS: Is it a real problem?", International Journal of Greenhouse Gas Control, 5, 4 (2011): p. 749-756.

52. D. Davies and G. Burstein, "The effects of bicarbonate on the corrosion and passivation of iron", Corrosion, 36, 8 (1980): p. 416-422.

53. W. Sun, S. Nešić, and R.C. Woollam, "The effect of temperature and ionic strength on iron carbonate ($FeCO_3$) solubility limit", Corrosion Science, 51, 6 (2009): p. 1273-1276.

54. W. Sun and S. Nešic, "Kinetics of corrosion layer formation: Part 1-Iron carbonate layers in carbon dioxide corrosion", Corrosion, 64, 4 (2008): p. 334-346.

55. J. Garside, "Advances in the characterization of crystal growth", AIChE Symposium Series, 80, 240 (1984): p. 23-38.

56. S. Guo, L. Xu, L. Zhang, W. Chang, and M. Lu, "Corrosion of alloy steels containing 2% chromium in CO_2 environments", Corrosion Science, 63, (2012): p. 246-258.

57. A.C. Lasaga, *Kinetic theory in the earth sciences*. 2014: Princeton University Press.

58. Y. Yang, *Removal Mechanisms of Protective Iron Carbonate Layer in Flowing Solutions*, 2012, PhD Thesis, Ohio University.

59. M.L. Johnson, *Ferrous carbonate precipitation kinetics - A temperature ramped approach*, 1991, PhD Thesis, Rice University.

60. J. Greenberg and M. Tomson, "Precipitation and dissolution kinetics and equilibria of aqueous ferrous carbonate vs temperature", Applied Geochemistry, 7, 2 (1992): p. 185-190.

61. J. Greenberg, *High temperature kinetics of precipitation and dissolution of ferrous-carbonate*, 1987, Masters Thesis, Rice University

62. D.K. Nordstrom, L.N. Plummer, D. Langmuir, E. Busenberg, H.M. May, B.F. Jones, and D.L. Parkhurst, "Revised chemical equilibrium data for major water-mineral reactions and their limitations", ACS symposium series, 416, (1990): p. 398-413.

63. G.M. Marion, D.C. Catling, and J.S. Kargel, "Modeling aqueous ferrous iron chemistry at low temperatures with application to Mars", Geochimica et cosmochimica Acta, 67, 22 (2003): p. 4251-4266.

64. C.A. Silva, X. Liu, and F. Millero, "Solubility of siderite ($FeCO_3$) in NaCl solutions", Journal of solution chemistry, 31, 2 (2002): p. 97-108.

65. D.L. Jensen, J.K. Boddum, J.C. Tjell, and T.H. Christensen, "The solubility of rhodochrosite ($MnCO_3$) and siderite ($FeCO_3$) in anaerobic aquatic environments", Applied geochemistry, 17, 4 (2002): p. 503-511.

66. C. Ptacek and E. Reardon. "Solubility of siderite ($FeCO_3$) in concentrated NaCl and Na_2SO_4 solutions at 25°C", Water-Rock Interaction, Proc. Int. Symp., 7th, 1992).

67. P.C. Singer and W. Stumm, "The solubility of ferrous iron in carbonate-bearing waters", Journal (American Water Works Association), 62, 3 (1970): p. 198-202.

68. J. Bruno, P. Wersin, and W. Stumm, "On the influence of carbonate in mineral dissolution: II. The solubility of $FeCO_3$(s) at 25°C and 1 atm total pressure", Geochimica et cosmochimica Acta, 56, 3 (1992): p. 1149-1155.

69. R.D. Braun, "Solubility of iron (II) carbonate at temperatures between 30 and 80°C", Talanta, 38, 2 (1991): p. 205-211.

70. W. Preis and H. Gamsjäger, "Critical evaluation of solubility data: enthalpy of formation of siderite", Physical Chemistry Chemical Physics, 4, 16 (2002): p. 4014-4019.

71. H.C. Helgeson, "Thermodynamics of hydrothermal systems at elevated temperatures and pressures", American journal of science, 267, 7 (1969): p. 729-804.

72. W.M. Latimer, "Oxidation states of the elements and their potentials in aqueous solutions", (1938).

73. H.J. Smith, "On equilibrium in the system: Ferrous carbonate, carbon dioxide and water", Journal of the American Chemical Society, 40, 6 (1918): p. 879-883.

74. C. Ptacek and D.W. Blowes, *Influence of siderite on the pore-water chemistry of inactive mine-tailings impoundments*. 1994, ACS Publications.

75. P. Bénézeth, J. Dandurand, and J. Harrichoury, "Solubility product of siderite ($FeCO_3$) as a function of temperature (25–250°C)", Chemical Geology, 265, 1 (2009): p. 3-12.

76. M. Johnson and M. Tomson. "Ferrous carbonate precipitation kinetics and its impact CO_2 corrosion", CORROSION 91, (Houston, TX: NACE: NACE, 1991).

77. W. Sun, *Kinetics of iron carbonate and iron sulfide scale formation in CO_2/H_2S corrosion*, 2006, PhD Thesis, Ohio University.

78. M. Ueda and H. Takabe. "Effect of environmental factor and microstructure on morphology of corrosion products in CO_2 environments", CORROSION 99, (Houston, TX: NACE, 1999).

79. A. Dugstad, L. Lunde, and K. Videm. "Parametric study of CO_2 corrosion of carbon steel", CORROSION 94, (Houston, TX: NACE, 1994).

80. A. Dugstad, L. Lunde, and K. Videm. "Influence of alloying elements upon the CO_2 corrosion rate of low alloyed carbon steels", CORROSION 91, (Houston, TX: NACE, 1991).

81. K. Videm. "The influence of pH and concentration of bicarbonate and ferrous ions on the CO_2 corrosion of carbon steels", CORROSION 93, (Houston, TX: NACE, 1993).

82. F. Pessu, R. Barker, and A. Neville, "The influence of pH on localized corrosion behavior of X65 carbon steel in CO_2-saturated brines", Corrosion, 71, 12 (2015): p. 1452-1466.

83. E. Van Hunnik, E. Hendriksen, and B.F. Pots. "The formation of protective $FeCO_3$ corrosion product layers in CO_2 corrosion", CORROSION 96, (Denver, CO: NACE International Conference, 1996).

84. M.H. Nazari, S. Allahkaram, and M. Kermani, "The effects of temperature and pH on the characteristics of corrosion product in CO_2 corrosion of grade X70 steel", Materials & Design, 31, 7 (2010): p. 3559-3563.

85. H. Fang, B. Brown, and S. Nešić, "Sodium chloride concentration effects on general CO2 corrosion mechanisms", Corrosion, 69, 3 (2013): p. 297-302.

86. Q. Liu, L. Mao, and S. Zhou, "Effects of chloride content on CO_2 corrosion of carbon steel in simulated oil and gas well environments", Corrosion Science, 84, (2014): p. 165-171.

87. F. Farelas, M. Galicia, B. Brown, S. Nešić, and H. Castaneda, "Evolution of dissolution processes at the interface of carbon steel corroding in a CO_2 environment studied by EIS", Corrosion Science, 52, 2 (2010): p. 509-517.

88. J. Han, B.N. Brown, and S. Nešić, "Investigation of the galvanic mechanism for localized carbon dioxide corrosion propagation using the artificial pit technique", Corrosion, 66, 9 (2010): p. 1-12.

89. Y. Yang, B. Brown, S. Nesic, M.E. Gennaro, and B. Molinas. "Mechanical strength and removal of a protective iron carbonate layer formed on mild steel in CO_2 corrosion", CORROSION 2010, (San Antonio, TX: NACE, 2010).

90. T. Tanupabrungsun, B. Brown, and S. Nesic. "Effect of pH on CO_2 corrosion of mild steel at elevated temperatures", CORROSION 2013, (Orlando, FL: NACE, 2013).

91. T. Tanupabrungsun, *Thermodynamics and Kinetics of Carbon Dioxide Corrosion of Mild Steel at Elevated Temperatures*, 2012, Ohio University.

92. D.W. Shannon. "The role of chemical components in geothermal brines on corrosion", CORROSION 78, (Houston, TX: NACE, 1978).

93. B. Ingham, M. Ko, N. Laycock, J. Burnell, P. Kappen, J. Kimpton, and D. Williams, "In situ synchrotron X-ray diffraction study of scale formation during CO_2 corrosion of carbon steel in sodium and magnesium chloride solutions", Corrosion Science, 56, (2012): p. 96-104.

94. C. Ding, K.-w. Gao, and C.-f. Chen, "Effect of Ca^{2+} on CO_2 corrosion properties of X65 pipeline steel", International Journal of Minerals, Metallurgy and Materials, 16, 6 (2009): p. 661-666.

95. K. Gao, F. Yu, X. Pang, G. Zhang, L. Qiao, W. Chu, and M. Lu, "Mechanical properties of CO_2 corrosion product scales and their relationship to corrosion rates", Corrosion Science, 50, 10 (2008): p. 2796-2803.

96. G. Zhao, J. Li, S. Hao, X. Lu, and H. Li, "Effect of Ca^{2+} and Mg^{2+} on CO_2 corrosion behavior of tube steel", Journal of iron and steel research international, 12, 1 (2005): p. 38-42.

97. L.M. Tavares, E.M. da Costa, J.J. de Oliveira Andrade, R. Hubler, and B. Huet, "Effect of calcium carbonate on low carbon steel corrosion behavior in saline CO_2 high pressure environments", Applied Surface Science, 359, (2015): p. 143-152.

98. S. Navabzadeh Esmaeely, Y.-S. Choi, D. Young, and S. Nešić, "Effect of calcium on the formation and protectiveness of iron carbonate layer in CO_2 corrosion", Corrosion, 69, 9 (2013): p. 912-920.

99. H.A. Alsaiari, S. Yean, M.B. Tomson, and A.T. Kan. "Iron calcium carbonate: Precipitation interaction", Society of Petroleum Engineers, (Aberdeen, UK, 2008).

100. S. Yean, H.A. Alsaiari, A.T. Kan, and M.B. Tomson. "Ferrous carbonate nucleation and inhibition", Society of Petroleum Engineers, (Aberdeen, UK, 2008).

101. H.A. Nasr-El-Din, J.D. Lynn, M.K. Hashem, and G. Bitar. "Field application of a novel emulsified scale inhibitor system to mitigate calcium carbonate scale in a low temperature, low pressure sandstone reservoir in Saudi Arabia", Society of Petroleum Engineers, (San Antonio, TX, 2002).

102. M.B. Tomson and M.L. Johnson. "How ferrous carbonate kinetics impacts oilfield corrosion", Society of Petroleum Engineers, (Anaheim, CA, 1991).

103. H.A. Alsaiari, A. Kan, and M. Tomson, "Effect of calcium and iron (II) ions on the precipitation of calcium carbonate and ferrous carbonate", SPE Journal, 15, 2 (2010).

104. H.A. Alsaiari, M.B. Tomson, and A.T. Kan. "Constant composition study of crystal growth of mixed calcium-ferrous carbonate salt", CORROSION 2010, (San Antonio, TX:NACE, 2010).

105. H.A. Alsaiari, N. Zhang, S. Work, A.T. Kan, and M.B. Tomson. "A new correlation to predict the stoichiometry of mixed scale: Iron-calcium carbonate", Society of Petroleum Engineers, (Aberdeen, UK, 2012).

106. J.L. Crolet, N. Thevenot, and A. Dugstad. "Role of free acetic acid on the CO_2 corrosion of steels", CORROSION 99, (San Antonio, TX:NACE, 1999).

107. E. Gulbrandsen and K. Bilkova. "Solution chemistry effects on corrosion of carbon steels in presence of CO_2 and acetic acid", CORROSION 2006, (San Diego, CA:NACE, 2006).

108. B. Hedges and L. McVeigh. "The role of acetate in CO_2 corrosion: The double whammy", CORROSION 99, (San Antonio, TX:NACE: NACE International, 1999).

109. N.N. Greenwood and A. Earnshaw, *Chemistry of the Elements*. 2012: Elsevier.

110. H.S. Harned and R.W. Ehlers, "The dissociation constant of acetic acid from 0 to 60° Centigrade", Journal of the American Chemical Society, 55, 2 (1933): p. 652-656.

111. O. Nafday and S. Nesic. "Iron carbonate scale formation and CO_2 corrosion in the presence of acetic acid", CORROSION 2005, (Houston, TX:NACE, 2005).

112. K. Videm and A. Dugstad, "Corrosion of carbon steel in an aqueous carbon dioxide environment. I: Solution effects", Materials Performance, 28, 3 (1989): p. 63-67.

113. J. Heuer and J. Stubbins, "Microstructure analysis of coupons exposed to carbon dioxide corrosion in multiphase flow", Corrosion, 54, 7 (1998): p. 566-575.

114. S. Rajappa, R. Zhang, and M. Gopal. "Modeling the diffusion effects through the iron carbonate layer in the carbon dioxide corrosion of carbon steel", CORROSION 98, (San Diego, CA: NACE: NACE, 1998).

115. T. Berntsen, M. Seiersten, and T. Hemmingsen, "Effect of $FeCO_3$ supersaturation and carbide exposure on the CO_2 corrosion rate of carbon steel", Corrosion, 69, 6 (2013): p. 601-613.

116. S. Nesic, J. Lee, and V. Ruzic. "A mechanistic model of iron carbonate film growth and the effect on CO_2 corrosion of mild steel", (Denver, CO:NACE, 2002).

117. A. Ikeda, M. Ueda, and S. Mukai, "CO_2 behavior of carbon and chromium steels", Advances in CO_2 Corrosion, 1, (1984): p. 39-51.

118. S. Arumugam, N. Tajallipour, and P.J. Teevens. "Modeling the influence of iron carbonate scale morphology in sweet corrosion prediction", CORROSION 2014, (San Antonio, TX: NACE: NACE International, 2014).

119. K. Videm and A. Dugstad. "Film covered corrosion, film breakdown and pitting attack of carbon steels in aqueous CO_2 environments", CORROSION 88, (Houston, TX: NACE, 1988).

120. A.B. Gavanluei, B. Mishra, and D.L. Olson. "Corrosion rate measurement of a downhole tubular steel at different CO_2 partial pressures and temperatures and calculation of the activation energy of the corrosion process", CORROSION 2013, (Orlando, FL: NACE, 2013).

121. M.F. Suhor, M.F. Mohamed, A.M. Nor, M. Singer, and S. Nesic. "Corrosion of mild steel in high CO_2 environment: Effect of the $FeCO_3$ layer", CORROSION 2012, (Salt Lake City, UT: NACE, 2012).

122. M. Nordsveen, S. Nešic, R. Nyborg, and A. Stangeland, "A mechanistic model for carbon dioxide corrosion of mild steel in the presence of protective iron carbonate films-Part 1: Theory and verification", Corrosion, 59, 5 (2003): p. 443-456.

123. S. Nešic, M. Nordsveen, R. Nyborg, and A. Stangeland, "A mechanistic model for carbon dioxide corrosion of mild steel in the presence of protective iron carbonate films—Part 2: A numerical experiment", Corrosion, 59, 6 (2003): p. 489-497.

124. J. Han, B.N. Brown, D. Young, and S. Nešić, "Mesh-capped probe design for direct pH measurements at an actively corroding metal surface", Journal of applied electrochemistry, 40, 3 (2010): p. 683-690.

125. Y. Hua, R. Barker, and A. Neville, "Relating iron carbonate morphology to corrosion characteristics for water-saturated supercritical CO_2 systems", The Journal Of Supercritical Fluids, 98, (2015).

126. N.R. Rosli, Y.-S. Choi, and D. Young. "Impact of oxygen ingress in CO_2 corrosion of mild steel", CORROSION 2014, (San Antonio, TX: NACE, 2014).

127. W. Li, B. Brown, D. Young, and S. Nešić, "Investigation of Pseudo-Passivation of Mild Steel in CO_2 Corrosion", Corrosion, 70, 3 (2013): p. 294-302.

128. J.E. Wong and N. Park. "Further investigation on the effect of corrosion inhibitor actives on the formation of iron carbonate on carbon steel", CORROSION 2009, (Atlanta, GA:NACE, 2009).

129. E. Gulbrandsen. "Acetic acid and carbon dioxide corrosion of carbon steel covered with iron carbonate", CORROSION 2007, (Nashville, TN: NACE International Conference: NACE International, 2007).

130. J. Kvarekval, S. Olsen, and S. Skjerve. "The effect of O_2 on CO_2 corrosion in pH stabilized gas/condensate pipelines", CORROSION 2005, (Houston, TX: NACE, 2005).

131. A. Dugstad, H. Hemmer, and M. Seiersten, "Effect of steel microstructure on corrosion rate and protective iron carbonate film formation", Corrosion, 57, 4 (2001): p. 369-378.

132. G.A. Schmitt and M. Mueller. "Critical wall shear stresses in CO_2 corrosion of carbon steel", CORROSION 99, (San Antonio, TX:NACE, 1999).

133. B.F.M. Pots, E.L.J.A. Hendriksen, and J.F. Hollenberg. "What are the real influences of flow on corrosion?", CORROSION 2006, (San Diego, CA: NACE, 2006).

134. C. de Waard, U. Lotz, and D.E. Milliams, "Predictive Model for CO_2 Corrosion Engineering in Wet Natural Gas Pipelines", Corrosion, 47, 12 (1991): p. 976-985.

135. T. Hara, H. Asahi, Y. Suehiro, and H. Kaneta, "Effect of flow velocity on carbon dioxide corrosion behavior in oil and gas environments", Corrosion, 56, 8 (2000): p. 860-866.

136. M. Ko, B. Ingham, N. Laycock, and D. Williams, "In situ synchrotron X-ray diffraction study of the effect of microstructure and boundary layer conditions on CO2 corrosion of pipeline steels", Corrosion Science, 90, (2015): p. 192-201.

137. M. Ko, B. Ingham, N. Laycock, and D. Williams, "In situ synchrotron X-ray diffraction study of the effect of chromium additions to the steel and solution on CO2 corrosion of pipeline steels", Corrosion Science, 80, (2014): p. 237-246.

138. M. Ko, N.J. Laycock, B. Ingham, and D. Williams, "In situ synchrotron x-Ray diffraction studies of CO_2 corrosion of carbon steel with scale inhibitors ATMPA and PEI at 80°C", Corrosion, 68, 12 (2012): p. 1085-1093.

139. B. Ingham, M. Ko, N. Laycock, N.M. Kirby, and D.E. Williams, "First stages of siderite crystallisation during CO2 corrosion of steel evaluated using in situ synchrotron small-and wide-angle X-ray scattering", Faraday discussions, 180, (2015): p. 171-190.

140. B. Ingham, M. Ko, G. Kear, P. Kappen, N. Laycock, J. Kimpton, and D. Williams, "In situ synchrotron X-ray diffraction study of surface scale formation during CO_2 corrosion of carbon steel at temperatures up to 90°C", Corrosion Science, 52, 9 (2010): p. 3052-3061.

141. Y. Hua, R. Barker, and A. Neville, "Comparison of corrosion behaviour for X-65 carbon steel in supercritical CO_2-saturated water and water-saturated/unsaturated supercritical CO_2", The Journal Of Supercritical Fluids, 97, (2015): p. 224-237.

142. L. Wei, X. Pang, C. Liu, and K. Gao, "Formation mechanism and protective property of corrosion product scale on X70 steel under supercritical CO_2 environment", Corrosion Science, 100, (2015): p. 404-420.

143. F. Pessu, R. Barker, and A. Neville, "Understanding pitting corrosion behavior of X65 carbon steel in CO_2-saturated environments: The temperature effect", Corrosion, 72, 1 (2015): p. 78-94.

144. R. De Motte, R. Barker, D. Burkle, S. Vargas, and A. Neville, "The early stages of $FeCO_3$ scale formation kinetics in CO_2 corrosion", Materials Chemistry and Physics, 216, (2018): p. 102-111.

145. M. Ueda and A. Ikeda. "Effect of microstructure and Cr content in steel on CO_2 corrosion", CORROSION 96, (Denver, CO: NACE, 1996).

146. C. Palacios and J. Shadley, "Characteristics of corrosion scales on steels in a CO_2-saturated NaCl brine", Corrosion, 47, 2 (1991): p. 122-127.

147. P.I. Nice and M. Ueda. "The effect of microstructure and chromium alloying content to the corrosion resistance of low-alloy steel well tubing in seawater injection service", CORROSION 98, (San Diego, CA: NACE, 1998).

148. D.A. López, S.N. Simison, and S.R. de Sánchez, "The Influence of Steel Microstructure on CO_2 Corrosion. EIS Studies on the Inhibition Efficiency of Benzimidazole", Electrochimica Acta, 48, 7 (2003): p. 845-854.

149. H. Takabe and M. Ueda. "The formation behavior of corrosion protective films of low Cr bearing steels in CO_2 environments", CORROSION 2001, (Houston, TX: NACE, 2001).

150. S. Al-Hassan, B. Mishra, D.L. Olson, and M.M. Salama, "Effect of microstructure on corrosion of steels in aqueous solutions containing carbon dioxide", Corrosion, 54, 6 (1998): p. 480-491.

151. J. Crolet, N. Thevenot, and S. Nešić, "Role of conductive corrosion products in the protectiveness of corrosion layers", Corrosion, 54, 3 (1998): p. 194-203.

152. J.L. Mora-Mendoza and S. Turgoose, "Fe_3C influence on the corrosion rate of mild steel in aqueous CO_2 systems under turbulent flow conditions", Corrosion Science, 44, 6 (2002): p. 1223-1246.

153. L. Paolinelli, T. Pérez, and S. Simison, "The effect of pre-corrosion and steel microstructure on inhibitor performance in CO_2 corrosion", Corrosion Science, 50, 9 (2008): p. 2456-2464.

154. A. Dugstad, H. Hemmer, and M. Seiersten. "Effect of steel microstructure upon corrosion rate and protective iron carbonate film formation", CORROSION 2000, (Orlando, FL: NACE, 2000).

155. F. Farelas, B. Brown, and S. Nešić. "Iron carbide and its influence on the formation of protective iron carbonate in CO_2 corrosion of mild steel", CORROSION 2013, (Orlando, FL: NACE, 2013).

156. S. Ieamsupapong, B. Brown, M. Singer, and S. Nesic. "Effect of solution pH on corrosion product layer formation in a controlled water chemistry system", CORROSION 2017, (New Orleans, LA: NACE International Conference, 2017).

157. P. Burke. "Synopsis: recent progress in the understanding of CO_2 corrosion, Advances in CO_2 Corrosion", CORROSION 84, (Houston, TX: NACE, 1984).

158. G. Schmitt. "Fundamental aspects of CO_2 corrosion", CORROSION 83, (Houston, TX: NACE, 1983).

159. A. Dugstad. "Mechanism of protective film formation during CO_2 corrosion of carbon steel", CORROSION 98, (San Diego, CA: NACE, 1998).

160. C. Bosch and R.K. Poepperling. "Influence of chromium contents of 0.5 to 1.0% on the corrosion behavior of low alloy steel for large diameter pipes in CO_2 containing aqueous media", CORROSION 2003, (San Diego, CA: NACE, 2003).

161. P.I. Nice, H. Takabe, and M. Ueda. "The development and implementation of a new alloyed steel for oil and gas production wells", CORROSION 2000, (Orlando, FL: NACE, 2000).

162. B. Kermani, M. Dougan, J.C. Gonzalez, C. Linne, and R. Cochrane. "Development of Low Carbon Cr-Mo Steels with Exceptional Corrosion Resistance for Oilfield Applications", CORROSION 2001, (Houston, TX: NACE, 2001).

163. K. Nose, H. Asahi, P.I. Nice, and J.W. Martin. "Corrosion properties of 3% Cr steels in oil and gas environments", CORROSION 2001, (Houston, TX, 2001).

164. T. Muraki, T. Hara, and H. Asahi. "Effects of chromium content up to 5% and dissolved oxygen on CO_2 corrosion", CORROSION 2002, (Denver, CO: NACE, 2002).

165. B. Kermani, J.C. Gonzales, G.L. Turconi, L. Scoppio, G. Dicken, and D. Edmonds. "Development of superior corrosion resistance 3% Cr steels for downhole applications", CORROSION 2003, (San Diego, CA: NACE, 2003).

166. B. Kermani, J.C. Gonzales, G.L. Turconi, T.E. Perez, and C. Morales. "In-field corrosion performance of 3% Cr steels in sweet and sour downhole production and water injection", CORROSION 2004, (New Orleans, LA: NACE, 2004).

167. B. Kermani, J.C. Gonzales, G.L. Turconi, T.E. Perez, and C. Morales. "Materials optimisation in hydrocarbon production", CORROSION 2005, (Houston, TX: NACE, 2005).

168. M.H. Sk, A. Abdullah, J. Qi, M. Ko, B. Ingham, N. Laycock, M. Ryan, and D. Williams, "The effects of Cr/Mo micro-alloying on the corrosion behavior of carbon steel in CO_2-saturated (sweet) brine under hydrodynamic control", Journal of The Electrochemical Society, 165, 5 (2018): p. C278-C288.

169. M.H. Sk, A.M. Abdullah, M. Ko, N. Laycock, B. Ingham, M.P. Ryan, and D.E. Williams, "Effect of Cr/Mo on the protectiveness of corrosion scales on carbon steel in sweet medium under high flow regime", ECS Transactions, 80, 10 (2017): p. 509-517.

170. K. Denpo and H. Ogawa, "Effects of nickel and chromium on corrosion rate of linepipe steel", Corrosion Science, 35, 1-4 (1993): p. 285-288.

171. Q. Wu, Z. Zhang, X. Dong, and J. Yang, "Corrosion behavior of low-alloy steel containing 1% chromium in CO_2 environments", Corrosion Science, 75, (2013): p. 400-408.

172. J. Sun, W. Liu, W. Chang, Z. Zhang, Z. Li, T. Yu, and M. Lu, "Characteristics and formation mechanism of corrosion scales on low-chromium X65 steels in CO_2 environment", Acta Metall Sin, 45, 1 (2009): p. 84.

173. C. Chen, M. Lu, D. Sun, Z. Zhang, and W. Chang, "Effect of chromium on the pitting resistance of oil tube steel in a carbon dioxide corrosion system", Corrosion, 61, 6 (2005): p. 594-601.

174. R. Nyborg and A. Dugstad. "Mesa corrosion attack in carbon steel and 0.5% chromium steel", CORROSION 98, (San Diego, CA:NACE, 1998).

175. J. Bryant and G. Chitwood, "Corrosion behavior of 1-22% chromium steels and monel K-500 in CO_2-brine environments", Advances in CO_2 Corrosion, 1, (1984): p. 163-172.

176. D.V. Edmonds and R.C. Cochrane, "The effect of alloying on the resistance of carbon steel for oilfield applications to CO_2 corrosion", Materials Research, 8, 4 (2005): p. 377-385.

177. L.D. Paolinelli, T. Pérez, and S.N. Simison, "The incidence of chromium-rich corrosion products on the efficiency of an imidazoline-based inhibitor used for CO_2 corrosion prevention", Materials Chemistry and Physics, 126, 3 (2011): p. 938-947.

178. L. Xu, B. Wang, J. Zhu, W. Li, and Z. Zheng, "Effect of Cr content on the corrosion performance of low-Cr alloy steel in a CO_2 environment", Applied Surface Science, 379, (2016): p. 39-46.

179. L. Xu, S. Guo, W. Chang, T. Chen, L. Hu, and M. Lu, "Corrosion of Cr bearing low alloy pipeline steel in CO_2 environment at static and flowing conditions", Applied Surface Science, 270, (2013): p. 395-404.

180. G. Sedahmed and L. Shemilt, "Forced convection mass transfer at rough surfaces in annuli", Letters in Heat and Mass Transfer, 3, 6 (1976): p. 499-511.

181. M. Alkhateeb, R. Barker, A. Neville, and H.M. Thompson, "The effect of surface roughness on diffusion and chemical reaction controlled limiting currents on a Rotating Cylinder Electrode in deaerated solutions with and without CO_2", CORROSION, in press, (2018).

182. G. Fogg and J. Morse. "Development of a new solvent-free flow efficiency coating for natural gas pipelines", Rio Pipeline 2005 Conference and Exposition, (Rio de Janeiro, Brazil, 2005).

183. D.A. Dawson and O. Trass, "Mass transfer at rough surfaces", International Journal of Heat and Mass Transfer, 15, 7 (1972): p. 1317-1336.

184. D. Gabe and F. Walsh, "The rotating cylinder electrode: a review of development", Journal of Applied Electrochemistry, 13, 1 (1983): p. 3-21.

185. J.J. De Yoreo and P.G. Vekilov, "Principles of crystal nucleation and growth", Reviews in mineralogy and geochemistry, 54, 1 (2003): p. 57-93.

186. W. Sun and S. Nešić. "Basics revisited: kinetics of iron carbonate scale precipitation in CO_2 corrosion", CORROSION 2006, (San Diego, CA: NACE, 2006).

187. Y. Yang, B. Brown, and S. Nesic. "Application of EQCM to the study of CO_2 corrosion", 17th International Corrosion Congress, (NACE, 2008).

188. P.G. Koutsoukos and E. Kapetanaki. "Mixed calcium carbonate and calcium sulfate scale", CORROSION 2016, (Vancouver, Canada:NACE, 2016).

189. O. Sanni, T. Charpentier, N. Kapur, and A. Neville. "$CaCO_3$ scale surface nucleation and growth kinetics in a once-through in situ flow rig as a function of saturation ratio (SR)", CORROSION 2016, (Vancouver, Canada:NACE, 2016).

190. O. Sanni, T. Charpentier, N. Kapur, and A. Neville. "Study of surface deposition and bulk scaling kinetics in oilfield conditions using an in-situ flow rig", CORROSION 2015, (Dallas, TX:NACE, 2015).

191. O. Bukuaghangin, O. Sanni, N. Kapur, M. Huggan, A. Neville, and T. Charpentier, "Kinetics study of barium sulphate surface scaling and inhibition with a once-through flow system", Journal of Petroleum Science and Engineering, 147, (2016): p. 699-706.

192. M.B. Tomson and G.H. Nancollas, "Mineralization kinetics: A constant composition approach", Science, 200, 4345 (1978): p. 1059.

193. M. Euvrard, F. Membrey, C. Filiatre, C. Pignolet, and A. Foissy, "Kinetic study of the electrocrystallization of calcium carbonate on metallic substrates", Journal of Crystal Growth, 291, 2 (2006): p. 428-435.

194. G. Sauerbrey, "Use of a quartz vibrator from weighing thin films on a microbalance", Z. Phys., 155, (1959): p. 206.

195. D. Burkle, R. De Motte, W. Taleb, A. Kleppe, T. Comyn, S. Vargas, A. Neville, and R. Barker, "Development of an electrochemically integrated SR-GIXRD flow cell to study $FeCO_3$ formation kinetics", Review of Scientific Instruments, 87, 10 (2016): p. 105125.

196. D. Burkle, R. De Motte, W. Taleb, A. Kleppe, T. Comyn, S. Vargas, A. Neville, and R. Barker, "In situ SR-XRD study of $FeCO_3$ precipitation kinetics onto carbon steel in CO_2-containing environments: The influence of brine pH", Electrochimica Acta, 255, (2017): p. 127-144.

197. A.J. Davenport, C. Padovani, B.J. Connolly, N.P. Stevens, T.A. Beale, A. Groso, and M. Stampanoni, "Synchrotron X-ray microtomography study of the role of Y in corrosion of magnesium alloy WE43", Electrochemical and solid-state letters, 10, 2 (2007): p. C5-C8.

198. B. Connolly, D. Horner, S. Fox, A. Davenport, C. Padovani, S. Zhou, A. Turnbull, M. Preuss, N. Stevens, and T. Marrow, "X-ray microtomography studies of localised corrosion and transitions to stress corrosion cracking", Materials science and technology, 22, 9 (2006): p. 1076-1085.

199. E. Maire and P.J. Withers, "Quantitative X-ray tomography", International materials reviews, 59, 1 (2014): p. 1-43.

200. E. Maire, P. Colombo, J. Adrien, L. Babout, and L. Biasetto, "Characterization of the morphology of cellular ceramics by 3D image processing of X-ray tomography", Journal of the European Ceramic Society, 27, 4 (2007): p. 1973-1981.

201. L. Brabant, J. Vlassenbroeck, Y. De Witte, V. Cnudde, M.N. Boone, J. Dewanckele, and L. Van Hoorebeke, "Three-dimensional analysis of high-resolution X-ray computed tomography data with Morpho+", Microscopy and Microanalysis, 17, 2 (2011): p. 252-263.

202. M. Tlili, M. Benamor, C. Gabrielli, H. Perrot, and B. Tribollet, "Influence of the interfacial pH on electrochemical $CaCO_3$ precipitation", Journal of The Electrochemical Society, 150, 11 (2003): p. 765-771.

203. C. Deslouis, I. Frateur, G. Maurin, and B. Tribollet, "Interfacial pH measurement during the reduction of dissolved oxygen in a submerged impinging jet cell", Journal of Applied Electrochemistry, 27, 4 (1997): p. 482-492.